

Doctoral Thesis

**Selective Darkening Filter
and Welding Arc Observation
for the Manual Welding Process**



Bernd Hillers
University Bremen

doctoral thesis

Selective Darkening Filter and Welding Arc Observation for the Manual Welding Process

Bernd Hillers

15th March 2012

1. Gutachter: Prof. Dr.-Ing. Axel Gräser
2. Gutachter: Prof. Dr.-Ing. Kai Michels

Zusammenfassung

Der Schutz des Schweißers während des Schweißens stellt die Grundmotivation dieser Arbeit dar. Die heutzutage verfügbaren, automatisch abdunkelnden Schweißfilter (Automatic Darkening Filter (ADF)) verbessern die Sicht des Schweißers, indem diese vor dem Zünden des Lichtbogens und während des Schweißens die Lichtdurchlässigkeit dynamisch anpassen. Ermöglicht wird dies durch Flüssigkristalldisplays (LCDs), bestehend aus einem einzigen Pixel zur Abdunkelung der Sicht. Die ADFs sind verbesserungsfähig, indem die Sicht des Nutzers nur dort abgedunkelt wird, wo der helle Lichtbogen im Blickfeld erscheint. Ein grafisches LCD (GLCD) mit einer Auflösung von $n \times m$ Pixeln ermöglicht die selektive Abdunkelung im Sichtbereich des Schweißers. Der Aufbau eines solchen selektiven, automatisch abdunkelnden Filters (Selective Auto Darkening Filter (SADF)) wird als Gesamtsystem entwickelt und seine Anwendbarkeit getestet. Unter anderem besteht der Aufbau zur korrekten Detektion der Lichtbogenposition aus der Integration einer Kamera in den Schweißprozess. Anstelle eines LCDs mit einem Pixel wird ein speziell für den Einsatz beim Schweißen angepasster Prototyp eines GLCD in den Sichtbereich des Schweißers integriert. Ein Kalibrierungsverfahren sichert die korrekte Projektion der Lichtbogenposition aus der Sicht der Kamera in die Sicht des Schweißers.

Wie eingeführt ist zur Detektion der Lichtbogenposition die Entwicklung eines angepassten Videosystems zur Beobachtung während des Schweißens notwendig. Die Videobeobachtung von Szenen mit hoher Kontrastdynamik tritt bei sehr großen Unterschieden zwischen dem hellsten und dunkelsten Bildpunkt auf. Spezielle Kamerachips sind in der Lage, solche anspruchsvollen hohen Kontrastdynamiken abzubilden. Solch eine hochdynamische Kamera wird zur Integration im Schweißschutzhelm eingesetzt. Die gewählte Anwendung, das Schweißen, mit ihren rauen Umgebungsbedingungen, macht die Entwicklung weiterer Hardware notwendig. So sind ein Problem die zumeist flackernden Lichtverhältnisse während der unterschiedlichen Phasen der Schweißprozesse. Die optische Synchronisation der Bildaufnahme auf den Schweißprozess stabilisiert die Videoaufnahme und ermöglicht weiterhin eine gezielte gepulste Beleuchtung durch kompakte Leuchtdioden höchster Leuchtdichte. Der Bildaufnahmeprozess wird weiterhin verbessert, indem zwei mit unterschiedlichen Kameraparametern aufgenommene Bilder als Datengrundlage genutzt werden. Hierbei werden ein unterbelichtetes und ein überbelichtetes Bild zu einem neuen Bild mit höherem Kontrastumfang, als es durch eine Einzelaufnahme möglich ist, zusammengeführt.

Die Grundannahme gängiger histogrammbasierter Kontrastverbesserungsalgorithmen, dass Histogrammklassen von Farbwerten mit geringer Häufigkeitsdichte auch geringe und damit unwichtige Informationen enthalten, ist bei der Videobeobachtung von Schweißprozessen nicht zutreffend. Der Lichtbogen und das helle Schweißbad als Interessenfokus und hellste Bereiche besitzen zumeist nur einen geringen Flächenanteil am Gesamtbild und bilden dabei Klassen geringer Häufigkeitsdichten. Um für die Kontrastverbesserung eine Lösung zu erhalten, werden unterschiedliche Standardalgorithmen getestet bzw. von diesen ausgehend ein neues Verfahren entwickelt. Dieses Verfahren segmentiert das Bild in Bereiche ähnlichen Inhalts, bereitet diese unabhängig auf und führt sie zu einem neuen Gesamtbild wieder zusammen. Diese Arbeit entwickelt somit alle Aspekte eines SADF Systems mit der Problematik der Abdunkelung der Sicht, Kalibrierung, Bildakquise und Bildaufbereitung.

Abstract

The protection of the welder during arc-time is the source of motivation for this thesis. Automatic Darkening Filter (ADF) enhance the welder's protection by giving him a good view of the welding scene before and during welding by driving automatically darken a one pixel LCD when the welding starts. These ADFs may be enhanced by darkening the welders view partially where it is necessary to protect him from glaring light. A Graphical LCD (GLCD) with a resolution of $n \times m$ pixels gives the ability to selectively control the darkening in the welders view. The setup of such a Selective Auto Darkening Filter is developed and its applicability tested. The setup is done by integrating a camera into the welding operation for extracting the welding arc position properly. Instead of the ADF a prototype of a GLCD taylored for welding is mounted in the welder's view. A calibration process assures the correct projection of the extracted arc position from the camera view onto the welders view.

The extraction of the welding arc position requires an enhanced video acquisition during welding. The observation of scenes with high dynamic contrast is an outstanding problem which occurs if very high differences between the darkest and the brightest spot in a scene occur. Special camera chips which map a high range of lighting conditions at once to an image can improve the image acquisition. Such a high dynamic range camera is used for the helmet integration. The application to welding with its harsh conditions needs the development of supporting hardware. The synchronization of the camera with the flickering light conditions of pulsed welding processes in Gas Metal Arc Welding stabilizes the acquisition process and allows the scene to be flashed precisely if required by compact high power LEDs. The image acquisition is enhanced by merging two different exposed images for the resulting source image. These source images cover a wider histogram range than it is possible by using only a single shot image with optimal camera parameters. For a welding scene the basic assumption that the bin of an histogram with the lowest number of pixels does not contain important information does not apply, because the arc, the brightest and most important spot in the image, is covers mostly a small area. After testing different standard contrast enhancement algorithm a novel more content based algorithm is developed. It segments the image into areas with similar content related to the used colour space and enhances these independently. So this thesis covers all aspects of a SADDF system with darkening the view, calibration, image acquisition and image enhancement.

” Cuando una puerta se cierra, otra se abre ”
” When one door closes, another one opens ”
” Wenn sich eine Tür schließt, öffnet sich eine andere ”

(Miguel de Cervantes Saavedra *1547 - †1616)

Contents

Glossary	15
1. Introduction	19
1.1. Organization of the thesis	20
1.2. Overview of the Welding Process	21
1.2.1. Gas Metal Arc Welding	21
1.2.2. Shielded Metal Arc Welding	25
1.2.3. Laser Welding	26
1.3. Welding Observation	26
1.3.1. Quality Assessment	27
1.3.2. Process Control	29
1.4. Personal Protection Equipment	30
1.4.1. Passive Filters	30
1.4.2. Automatic Darkening Filter	31
1.4.3. Selective Auto Darkening Filter	31
1.4.4. Mixed Reality	32
2. State of the Art	35
2.1. Welding Protection	35
2.1.1. Sensitivities of the Human Eye	35
2.1.2. Regulations for Welding Protection	39
2.1.3. Automatic Darkening Filter	40
2.2. Welding Process Observation	42
2.2.1. Process Parameter	42
2.2.2. Visual Observation	42
2.3. Image Processing	49
2.3.1. Spatially Uniform Enhancement	50
2.3.2. Spatially Varying Enhancement	50
2.3.3. Noise Filtering	51
2.4. High Dynamic Range Increase	51
2.4.1. Recovering Radiance Map	53
3. IntARWeld system	57
3.1. Image Acquisition	58
3.1.1. High Dynamic Range Camera System	58
3.1.2. Optical Camera Trigger	60
3.1.3. Active LED Lighting	65

3.1.4. Toggle Merging for High Dynamic Range Increase	69
3.2. Image Enhancement	73
3.2.1. Using Histogram Equalization	74
3.2.2. Using Grey Level Grouping	75
3.2.3. Using Contrast Limited Histogram Equalization	81
3.2.4. Variable Block Shape Adaptive Histogram Equalization	86
3.2.5. Stripe denoising	94
3.3. Selective Automatic Darkening Filter	95
3.3.1. Graphical Liquid Crystal Display	97
3.3.2. Calibration of a GLCD to the Camera	98
4. Results	103
4.1. Pulsed MAG process	104
4.1.1. Raw Data	104
4.1.2. Comparing Different Image Enhancement Algorithms	108
4.1.3. Comparing Results of VBSAHE Processing with LED Lighting	115
4.1.4. Merging two Different Exposed Images	116
4.2. Pulsed MIG process	123
4.3. Pulsed TIG Process	124
4.4. The Selective Automatic Darkening Filter	126
4.5. Conclusions	128
A. Appendix	131
A.1. Mathematical Conventions	131
A.2. Linear Algebra	131
A.3. 2D Projection of the 3D World	133
A.3.1. Finite projective camera	133
A.4. Schematics	136
A.5. Results of different image processing algorithms	137
Bibliography	143
List of Figures	149
List of Tables	153

Glossary

Abbreviations

ADF (Automatic Darkening Filters) An Automatic Darkening Filter is welding filter which darkens the view automatically if a welding arc is in the welders view. So the welder can see the scene through the filter while not welding and is protected by the automatic shading against the bright glaring from the welding arc.

AR (Augmented Reality) Augmented reality is a part of a virtuality continuum called Mixed Reality, which was introduced by Paul Milgram [1]. It describes the interstages of this continuum ranging from the real environment, to augmented reality over augmented virtuality to a pure virtual environment.

CCD (Charged Coupled Device) Type of a camera chip which integrates the incoming photons by transforming the collected charge caused by the photo current to a voltage. Too high charges may flood neighboured regions where they distort the voltage measurement of the neighboured cell. This effect is called blooming where white areas bloom from a spot of high brightness intensity to neighboured regions.

CLAHE (Contrast Limited Adaptive Histogram Equalization) The CLAHE algorithm divides the images into $n \times n$ squares, which are enhanced independently but limited related to contrast. The resulting image is produced by merging the enhanced tiles to the complete image.

DOF (degree of freedom) One degree of freedom is the ability either to move along a line or to rotate around a line.

EMC (Electromagnetic compatibility) A branch of electrical sciences which studies the unintentional generation, propagation and reception of electromagnetic energy with reference to the unwanted effects (Electromagnetic interference, or EMI) that such energy may induce. The goal of EMC is the correct operation, in the same electromagnetic environment, of different equipment which use electromagnetic phenomena, and the avoidance of any interference effects.

FPN (Fixed Pattern Noise) An uncalibrated C-MOS camera chip does not supply equal pixel values for single-coloured areas. So before using the camera the camera is

calibrated by holding a single coloured surface in front of the lense and storing for every single pixel its deviation to the mean value of all pixel. Now during grabbing images this deviation is subtracted from every single image, with the result that single- coloured surfaces occur with nearly constant values for all its pixels. The matrix with the subtractions for every single camera pixel is called the fixed pattern noise. It is a noise which is related to the pixel position and not to time as it is constant over time.

GLCD (Graphical Liquid Crystal Display) A Graphical LCD specifies a LCD, where single uniform pixel points may be independently controlled.

GLG (Grey-Level-Grouping) A contrast enhancement algorithm which unites (groups) the smallest histogram bin of a grouping step with its smallest neighbour. The grouping step is repeated until only two groups remain. For the pixel mapping, the pixel values are re-distributed in an un-grouping step between the minimum and maximum value of a group. The un-grouping is done for all groups for measuring the contrast quality for every grouping step. At the end the grouping step level with the highest calculated contrast is selected.

GMAW (Gas Metal Arc Welding) Gas Metal Arc Welding means the subordinate concept of welding with an electric arc. A wire is constantly fed through a welding torch plus a shielding gas covering the melting pot. The wire serves as the electrode for the arc and as filler material for the welding seam.

HDRI (High Dynamic Range Increase) The technique of HDRI increases the photographic information mapped from the environment to a frame by merging a number of differently exposed images. Secondly the abbreviation HDRI is used for High Dynamic Range Images which use float values to represent the colour information in order to avoid a fixed step size.

HMD (Head Mounted Display) A head mounted display enables the user to gather information by a wearable head-worn device. HMD are available in video-see-through and optical-see-through design. The video-see-through shows the user only the video fed to the device while the optical-see-through supplies a diaphanous display so that the environment can be seen plus the video information.

IntARWeld (Intelligent Augmented Reality Welding Helmet) The Marie Curie Transfer of Knowledge Project (TOK) IntARWeld (MTKI-CT-2005-029652) is founded by the European Union. Its partners are recruited from the Friedrich-Wilhelm-Bessel Institut Forschungsgesellschaft mbH (FWBI) and the welding helmet producer Sperian Welding Protection AG in Wattwil (Switzerland).

LCD (Liquid Crystal Display) A liquid crystal display (LCD) is a thin, flat display device made up of any number of color or monochrome pixels arrayed in front of a light source or reflector. Each pixel of an LCD consists of a layer of liquid crystal molecules aligned between two transparent electrodes, and two polarizing filters, the axes of polarity of which are perpendicular to each other. With no liquid

crystal between the polarizing filters, light passing through one filter would be blocked by the other. If a voltage is applied between the electrodes, the liquid crystals are aligned parallel to the electrode with a torsion so that the preferred orientation of the polarized light from the one side is shifted to the orientation of the opposite polarizer.

MAG (Metal Active Gas Welding) Process where an active gas is used to improve the arc stability. It may supply carbon -dissolved from carbon dioxide- for to burn up foreign matters in the melting pool. A very common active gas is a mixture of 82% argon with 18% carbon dioxide.

MIG (Metal Inert Gas Welding) The Metal Inert Gas Welding means the concept of used shielding gas. The used gas shall protect the melting pot from oxidizing, what would change the temperature and the material in the metal pool e.g. Aluminium, with its hard aluminiumoxide phase, is welded with argon as inert gas.

MISE (Mean integrated squared error) An optimum criterion used in density estimation is given by summing up all deviations of an estimated value based on a sample from the real value (groundtruth).

PDF (Probability Density Function) The Probability density function of a multidimensional random variable is a function that describes the relative likelihood in the observation space. It can be estimated by a so called density estimator. The estimator uses a finite number of samples of the process.

PPE (Personal Protection Equipment) Equipment related to all aspects of personal protection for working like ear, eye, hand and foot protection.

SADF (Selective Automatic Darkening Filter) Optical filter which darkens selectively automatically when the welding arc starts by identifying glaring light sources and darkens selected pixels of a Graphical Liquid Crystal Display (GLCD) where the light source occur in the view of the welder.

SMAW (Shield Metal Arc Welding) One of the oldest manual welding processes developed in 1908. A massive rod coated with a material which produce during welding shielding gases and light slag on the seam, is clamped to a rod holder. The welder holds this rod which is used like in GMAW processes as electrode and filler material.

SVD (Singular Value Decomposition) Algorithm to decompose a $n \times m$ matrix into its Eigenvalues and Eigenvector. It can be used to retrieve an optimal solution for an overdetermined system based on unprecise data.

TIG (Tungsten Inert Gas Welding) Process as well known as Gas Tungsten Arc Welding which uses a nonconsumable (tungsten-) electrode for the welding arc. If filler material is needed for the welding process, it is applied from outside. Mostly a

rod is fed by the welder to the weld pool. This process can produce filigree arcs to weld thin materials.

TN (Twisted Nematic) A type of LCD where the liquid crystal fluid rotates the plane of polarization about 90° .

TOK (Transfer of Knowledge Program) A Transfer of Knowledge program aims for the knowledge exchange between business and academic institutions. The knowledge transfer is based on interchange of people working from the business unit at the academic institute and vice versa.

VBSAHE (Variable Block Size Adaptive Histogram Equalization) The VBSAHE algorithm segments the image related to its content. The segments are enhanced independently but limited to its contrast. The resulting image is produced by merging the enhanced tiles to the complete image.

1

Introduction

The first experiments in the modern arc welding were made by the Russian engineer Nikolai Gawrilowitsch Slawjanow in 1891 when he used a metal electrode instead of a carbon one. Hence the electrode was used to invoke an electric arc and to be transferred as filler metal. From these first experiment until the present time about 156 different welding processes have been developed for over 2000 different types of metal materials and the number is still growing. The welding process now has wide application in the value creation chain like automotive, shipyards, building construction, chemical industry et cetera. The process of welding, cutting and screwing produced in the year 2008 about 6% of value of germany's gross domestic product.

The welding process is one that still relies heavily on the skill of the welder, because the process is sensitive to slight changes of its numerous parameters, so automation of the welding process is generally limited to specific recurring tasks. Robustness of any process can be improved by sensing and monitoring it. In welding the sensing is mostly done at a distance from the place where the welding process takes place. The harsh conditions of an electrical arc with a pool of melted metal, flying metal drip and splatters of the process cause glaring light, harmful ultraviolet rays, unhealthy smoke, dirty conditions, high temperature and high electromagnetic distortions which make direct measurement very challenging. Hence the available sensors concentrate on measuring parameters such as voltage, current or wire feed speed, light and acoustic emissions to calculate or estimate physical quantities. For automated seam tracking and quality measurement the seam is measured online in front and behind the welding torch as the weld is made.

The human visual system with the eyes protected by a welding helmet with an optical darkening filter is still considered to be superior to common electronic sensor systems because of its higher dynamic contrast range. The only disadvantage of this approach is that the

area around the weld becomes less visible because the welding helmet darkens the whole visible scene not just the weld itself. Current available auto darkening filters (ADF) use a one pixel LCD to darken the view at the exact moment of arc occurrence. New developments of graphical LCDs (GLCD), may offer a 2D matrix with independently shadable pixels. One can imagine that if such a GLCD is placed between the eye and the welding arc, it only has to darken the view where the arc occurs and can leave the surrounding view unaffected. The application of a GLCD for selectively auto darken the view of the welder, is one of the aims of this thesis. The welder shall be supplied with a running prototype of a selective auto darkening welding helmet.

To extract the right position of the glaring lights as it occurs with the arc, a sensor system has to be used. Trials have been done to photograph or film the seam using standard CCD cameras, but the results gave little usable visible information because of the low contrast dynamics of CCD or standard C-MOS camera chips. Blooming effects of a single bright spot cause saturation over a large area resulting in barely visible surrounding or a poor flickering image. For some years video sensor chips are available with the ability to map a high dynamic range of contrast ratio to a digital image. They potentially provide the ability to setup a system for the observation of the electrical arc in the welding process and weld pool. To provide an effective technical setup it is not sufficient to have the right sensor. It is also necessary to understand and minimize the effect of other process phenomena that reduce the quality of the image. This states the second aim of the thesis, which is the examination of the problem of extracting a proper video view of the welding process. The resulting video quality depends on the welding process, the camera system and the final image processing that enhances the information contained in the captured images.

1.1. Organization of the thesis

During reading of the different chapters, the reader will gain knowledge about the boundary conditions as given by the welding applications and state-of-the-art for eye protection during welding. In order to understand the environment given by a welding arc, the most important issues of gas metal arc welding (GMAW) are introduced in the sections that follow. The motivation for a welding protection system with a SADF technique using a GLCD is presented as well as applications for a welding observation system.

Chapter 2 will start with the human eye and its perception for light and contrast, which will be the next issue on the track to the complete boundaries for a SADF system. Especially the medical considerations in accordance to the emitted radiance of the welding, introduce the need for a safe eye shield.

After introducing the human eye and its need for welding protection, the norm for working safety which represent the condensed experience about protection, will be presented. The focus will be on the European Norms, to have beside the academic access as well the practical knowledge with the focus onto the human user. Coming from the human perception of the process, the machine vision part will be examined. Especially the image acquisition and

image pre-processing for direct welding observation is a central subject related to the state-of-the-art. Here the process and the camera must be jointly reviewed. The chapter 2 ends with the introduction to the high dynamic range increase (HDRI) by merging multiple shots of the identical scene but different camera parameters in order to give the idea of raising the cameras contrast dynamics.

Chapter 3 focusses on the direct development of the SADP. The different issues presented in the preceding chapter will be further developed. So the image acquisition and improvement followed by a deep view onto the mathematical description for the mapping between the worlds from 3D to 2D will be elaborated. The selective shading needs to cope with glaring light sources of varying brightness and reflections due to different process parameters (e.g. welding current, type of wire electrode), different material (e.g. construction steel, aluminium), different surfaces (e.g. polished, untreated, painted, rusty) and the geometrical setup of the environment for reflections (e.g. plain surfaces, closed space). After developing the application from the theoretical point of view, the real world results will be measured and evaluated in chapter 4.

1.2. Overview of the Welding Process

The huge amount of about 156 different welding processes and 2000 different sorts of material for welding, urge to constraint the SADP system to the most important welding applications. The MIG and MAG processes are presented uniquely although they use a similar technique. The reason are the different conditions they produce for image acquisition.

1.2.1. Gas Metal Arc Welding

The Gas Metal Arc Welding (GMAW) is a class of welding which uses an electrical welding arc and a covering gas. The arc is produced by a metal electrode which serves also as filler material. The function of the gas is to cover the melting pool for either protect it completely from oxidation or supply the process with active gas components to control the metallurgy process. The shielding gas and its flow rate also have a pronounced effect on aspects of the welding process like [2]:

- Arc characteristic: (e.g. length, shape, stability)
- Mode of metal transfer: (e.g. globular transfer, spray transfer, droplet transfer frequency, size of drops)
- Penetration and weld bead profile
- Undercutting tendency
- Cleaning Action: (e.g. burning impurities)

1. Introduction

- Mechanical properties after welding

Normally a wire is fed through a welding torch and acts as the melting electrode, with the melted material filling the welding seam as shown in figure 1.1. The gas flow encloses the wire electrode and the area of the melting pool. Below a distinction of the GMAW will be made concerning the implementation of the welding arc with its connected metal transfer modes and the used gas for the process.

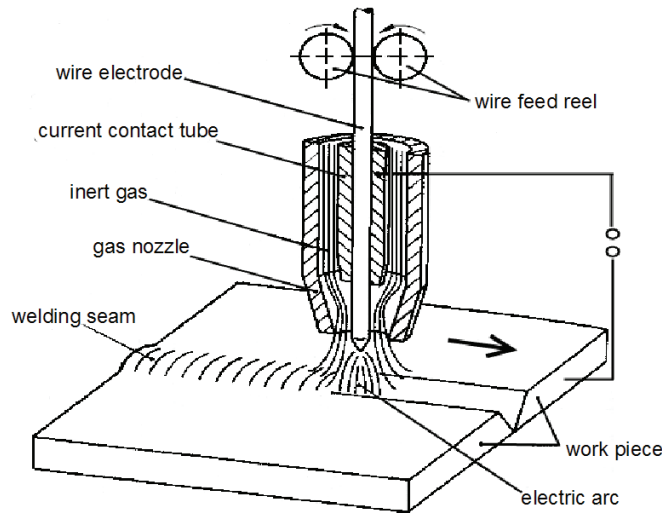


Figure 1.1.: *Technical Concept of GMAW. (source:[3])*

The welding arc and its connected metal transfer exists in four different major forms: globular, short circuit, spray and pulsed spray.

Short Circuiting Transfer The short circuit arc can use the lowest range of welding currents. When starting the process, the wire electrode is constantly fed through the torch and touches the workpiece causing a short circuit as it can be seen in figure 1.2 [A]. Due to the short circuit, the current rises [B,C] rapidly and heats the wire until it is melted [D]. The liquid metal pinches off the electrode [E] and the short circuit is interrupted causing an arc. Electromagnetical forces transport the liquid metal to the weld pool[F]. The welding arc burns until the wire contacts the workpiece again, causing the short circuit [G,H,I] and the process repeats. This happens with a frequency of 20 to 200 Hz and depends on a variety of parameters like current, gas and electrode material.

Globular Metal Transfer Globular metal transfer produces metal drops at the end of the electrode with a size bigger than the diameter of the wire. It takes place at low currents, if the force of the welding is not sufficient to pinch off metal drops from the electrode, so that either gravity or a short circuit detaches them. Globular transfer has a high deposition rate and thus high welding speeds may be reached. The disadvantage is that the huge drops

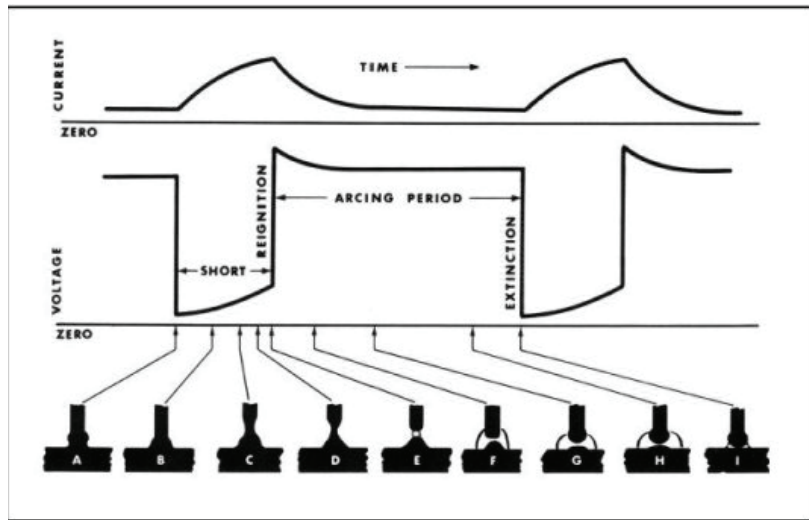


Figure 1.2.: *Phases of the short circuit welding arc (source:[2])*

causes a high sputter rate, an uneven surface and is limited to flat and horizontal positions [4].

Spray Transfer In the spray transfer mode the welding arc has such a high energy, that the metal drop pinches off the electrode by magnetic effects before the electrode contacts the workpiece. For this mode of operation a stable electric arc with a higher average current is needed. The stability of an arc can be boosted by using a gas mixture of mostly argon plus carbon dioxide as an active component. Argon is an inert gas more than 1.4 times denser than air and provides an inert blanket against oxidation of the melting pool. The carbon dioxide in the mixture provides a better ionisation of the arc path and thus improves the arc stability. The presence of carbon dioxide constraints the use of this exemplary gas mixture to carbon and low alloy steel. The spray transfer mode results in a highly focussed stream of tiny drops (spray) onto the work piece, which are merely influenced by gravity forces.

Pulsed Spray Transfer The pulsed spray transfer mode is made possible by current controlled welding sources, which can produce a high current signal of nearly any shape. The basic signal for pulsed spray transfer consists of a positive **Alternating Current (AC)** superimposed on a low constant (DC) current (see figure 1.3). The DC signal (see figure 1.3 (A)) keeps the arc burning on a level without forming metal drops on the wire tip. The positive AC-signal does the job of metal transfer. At the moment the welding current is forced to rise by the welding source, a metal drop begins to pinch off the electrode (B) and accelerates towards the work piece with its positive polarity. In order not to accelerate too much, the welding source lowers the current, but still keeps it high to enforce a straight trajectory (backpack current) (C). In ideal case the arc current returns to the DC-level, when the drop touches the work pieces(D). Depending on the welding parameters this process runs with a recurrence rate of 20 – 200Hz for the described sequence. Beside this basic form of a pulsed welding arc, a huge variety of different arc-signals exists for different applications.

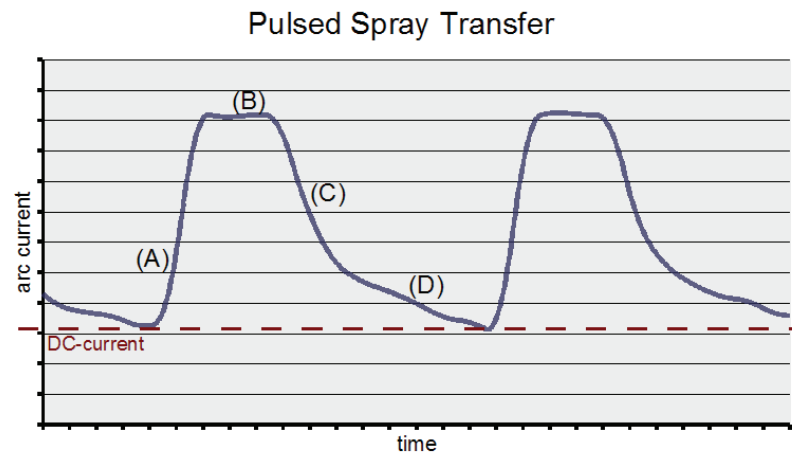


Figure 1.3.: *Qualitative example of measured spray transfer*

Metal Inert Gas Welding

After describing the different types of metal transfer modes a concise explanations of the different welding processes are given.

The Metal Inter Gas (MIG) process uses mostly argon, helium or a mixture of both. The purpose of the inert gases is to cover the welding process against reactions with oxidizing atmospheric gases. One of the most utilized materials for MIG welding is aluminium. It is sensitive to oxidation and aluminium-oxide is a hard and resistant shell which melt at high temperature. Its melting point is at about 2050°C while pure aluminium melts at 660°C. This is one reason why aluminium welding is more complicated, as the for high temperature resistant aluminium-oxide skin must be breached, while the pure aluminium body is already melting some thousand grades Celsius below.

Metal Active Gas Welding

Adding an active gas like oxygen or carbon oxide gives the Metal Active Gas (MAG) welding the effect of improving the arc stability due to better ionization in the arc track. For carbon steel and low alloy steels carbon dioxide deepens the penetration of the material but increases the sputter loss. Adding oxygen grows the weld pool, the penetration and arc stability but a higher oxidation of the welding material occurs, with a loss of silicon and manganese, which can change the metallurgy of alloyed steel.

Tungsten Inert Gas Welding

The Tungsten Inter Gas (TIG) is a process in which the filler material is not used as the arc producing electrode. Commonly a DC arc is produced between the work piece and a non-

consumable tungsten electrode. This electrode is covered by an inert shielding gas like argon or helium to protect it and to cover the weld pool from oxidation (see figure 1.4). A filler material is often used but is not compulsory as it can be omitted at thin butt joints. The feeding of the filler material to an arc, which burns constantly from the tungsten electrode, does not splatter which allows a smooth seam to be laid. On the other hand the quality of the process is as only as good as the skill of the welder in handling the welding torch. If the electrode touches the work piece, then beside some wolfram inclusions in the seam, the conic form of the electrode is destroyed by metal that attaches to it, resulting in the shape and quality of the welding arc becoming poor. An additional issue is that the tungsten electrode needs some special protection against oxygen. Especially if the arc is turned off the electrode has to be cooled and protected by the shielding gas down to 300°C. High quality professional TIG welding machines turn off the arc smoothly to avoid shrinkage cavities, enable crater filling and electrode cooling at once.

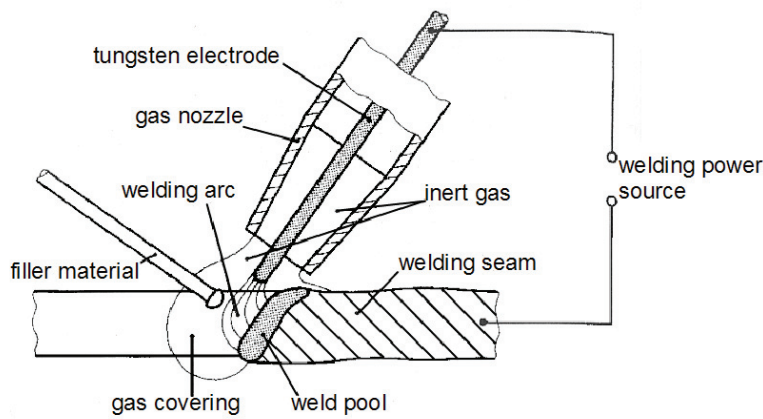


Figure 1.4.: *Technical principle of a TIG process (source:[3])*

The TIG-process can cause significant electromagnetic compatibility (EMC) problems, when the arc is started. For example one non-contacting technique to start the arc uses a high frequency (HF) starter which causes high current surges and by that high electromagnetic radiations. This may cause computing boards like microcontrollers (μC), interface chips or Personal Computers (PC) to crash or to be damaged. An alternative approach uses a technique called lift-arc. Here the welder first touches the workpiece with the tungsten electrode, while the welding source measures the voltage between electrode and workpiece and does not raise the current from a low level until the electrode is lifted off the workpiece and the arc starts at an insignificant distance between electrode and workpiece.

1.2.2. Shielded Metal Arc Welding

This process is also known as stick welding. In comparison to processes where some shielding gas is used to protect the weld pool from oxidation, the stick welding uses a glass like film called slag, produced during the process for weld metal protection. No wire is constantly

1. Introduction

fed through a welding torch. A coated thick rod electrode is clamped into a holder and the feeding is done by the user with the rod holder in his hand. This process was one of the first being commercially used. It is the most sensitive and most robust process one in a kind. It is the most sensitive, because the welder does not really see the process as clear like a GMAW process and must feed manually the electrode. The manual feeding means another degree of freedom to be handled by the welder, so that a good welding seam expects higher welding skills. On the other hand it is the most robust process, because in comparison to the GMAW process, which is quite sensitive to air draught, the Shielded Metal Arc Welding (SMAW) process is less sensitive because the coating of the rod electrode produces during welding a shielding gas and the remaining light slag covers the seam and forces a slow cool down of the process. These properties are helpful on open air construction sites, where adverse weather condition make welding more complicated.

1.2.3. Laser Welding

Beside drilling and cutting, a laser can be used for welding. It is a process with brings highly focussed energy to the workpiece whereby the heat affected zone is small. Laser welding is usually used without any filler material and the laser produce a weld pool to a depth depending on the focus point of the laser beam. Pure laser beam welding can be divided into the heat transfer and keyhole melting. The first uses a laser with "low" energy, which impinges on the metal surface and heats it until it melts. The keyhole technique uses a laser with higher power which forms a small channel of vaporised metal and thus a smaller weld pool. Due to the high but very focussed energy, this method is suitable for high speed welding.

1.3. Welding Observation

Welding observation is normally done by a person looking through a darkening filter. The human eye is able to perceive a huge variety of contrast dynamics. So if the welder uses a darkening filter he is able to see the bright welding arc and also the surrounding of this scene. Using a passive or automatic filter in front of a commercial CCD video camera has disappointing results. The welding arc is mapped to appear as a white area, due to the blooming effect of the CCD technology. This effect is produced by very bright spots in a scene whose brightness exceeds the maximum abilities of the pixel cell (see figure 1.5). Welding videos of the welding process with all its details as seen by the human observer through a darkening filter is not available and opens a new field of application in quality assessment, process control, human interaction and personal protection equipment. But the term "observation" can be interpreted to a wider area, if it is seen independent from visual impressions. The following paragraphs do give an overview about the varieties of observation applicable to welding results related to different purposes.

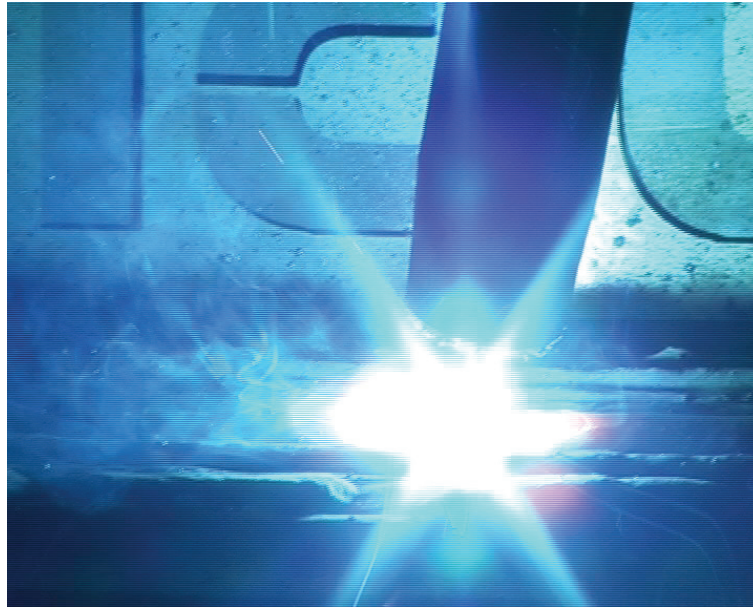


Figure 1.5.: *CCD camera image of MAG process with bloomed view on arc*

1.3.1. Quality Assessment

To ensure a reliable quality assessment of a desired welding process a variety of different measurement approaches are used. Starting from classical paper sheets where the used welding machine parameter and used material are documented, the bandwidth includes non-destructive method in online and post analysis. During welding the process parameters like current and voltage may be recorded or tracking sensors which work by tactile probes or laser triangulation in front or behind the welding torch keep the track. In the post process phase measurements can be done by using

- x-ray photo

The most commonly and widely used technique available for quality assessment is x-ray photography of the welding seam. On one side of the seam the photographic film is placed while on the other side a γ -ray source "exposures" the film. The 3D details information of the seam is thereby mapped to 2D image which integrates the information in depth of the material.

- ultrasonic

An ultrasonic transmitter in contact to the workpiece transmits a directed wave into it, which is distorted and reflected by the imperfections in the material. The echo of the ultrasonic signal give information about the inner structure of the material.

- pyrometer

A pyrometer gives information about the temperature of the work piece without contacting it. Spatial resolving pyrometer or IR-cameras supply information about the work piece and weld pool.

1. Introduction

- dye penetration

This method makes surface defects like cracks visible. A high capillary ink is applied by spraying or painting it onto the produced seam. The ink dissolves into the finest cracks. After cleaning a developer is used to drive the ink out of the cracks so that it becomes visible on the surface, making the cracks clearly identifiable. The ink is often fluorescent so that it can be easily seen using ultraviolet light

- magnetic powder

With ferromagnetical materials the magnetic powder method can be used. In this method the material is covered with fine metal powder and a pattern is induced in the metal powder that follows the magnetic flux in the metal. Defects or inclusion in the metal deflect the magnetic flux lines so that the metal powder pattern maps the information from inside the material onto its surface.

- eddy current

The eddy current method is applicable for automated testing. A primary coil induces by electro magnetic induction a local field to the metal piece. This field can be sensed by a secondary coil. If a defect in the material deflects the eddy current lines then it overlays with the primary magnetic field resulting in an attenuated field sensed by the secondary coil.

- acoustic emission

Two different methods exist for acoustic testing. The first method acoustic emission is an intrusive method which measures the emissions during tension or pressure testing. Cracks in the material produce a crackle sound if the material is impinged on pressure or tension. Using several microphones may give information about the position of the defect. This method gives a simple applicable approach for testing huge structures by stressing them without harming.

The second method is related to process supervision during automated welding. The automated process is taught by a self learning system and deviation after learning imply possible error during the production [5] (see i³tech ¹).

This short list of non-destructive measurements related to welding is not comprehensive [6], but it shows that all testing modes avoid directly contacting the location where and when the real process takes place that is where the metal melts while the arc burns.

Welding observation may enhance these approaches to an in situ observation of the running process.

¹<http://www.i3tech-gmbh.com/> seen on 27.3.2009

1.3.2. Process Control

The application to use a proper welding process visualization is inherent to apply this new data domain of welding observation for process control in automated and semi-automated processes. Achieving a high quality video opens the field of application to several new opportunities.

Remote View

Processes like tractor automata, semi-automated production using positioners, roller beds or portal system for stringer joining, often need a manual supervisor to make adjustments during welding. The torch distance or the position relative to the prepared welding seam may change which results in inappropriate joints. A remote view on the process including the arc and environment may facilitate a remote control of the production by one person with more than one process being supervised at once.

Seam Tracking

Seam tracking during automated welding is used to either rise the precision of a welding task by avoiding misalignment or to weld fuzzy taught production. Tactile sensors exist with a metal finger gliding at an edge of the workpiece and the torch is guided along one axis. The guidance of the process cannot be done directly at the position of the welding arc and needs to be guided either by an edge parallel to the seam.

Another approach is to use laser light section where a camera is heading on a projected laser line. On a plain surface the laser line is straight visible. Aberrations by unevenness do deform the straight line depending on the height of the asperity. A laser triangulation sensor supplies 2D information of the surface. The sensor cannot be used directly at the position of the welding arc, as either the camera is blended by the light or the laser line is not visible. The average minimum distance from relative to the welding arc depends highly on the available contrast dynamic of the used camera.

A stereo camera system which can grab good images of the process may extracts a 2.5D view of the process and may supply precise information about the welding process at the weld pool for seam tracking.

Arc Length and Torch Distance Measurement

The length of the welding arc defines significantly the produced heat power and its dissemination. Low profile metal sheets are more sensitive to deviations from optimal power distribution, The arc length measurement is a task which is roughly done by the welding

1. Introduction

power source by measuring the voltage at the arc path. The drawback to be coped with, is the unknown chain of contact resistors of the setup between the two connector (poles) of the welding source. They differ from setup to setup and as well during the process as the conductance of the arc and workpiece change with its temperature, working position and distance. Especially in MIG and MAG processes the resistors between the contact tip in the welding torch and the wire electrode are not stable and cause imprecision in arc-length extraction. For GMAW in the specialization of very short ($0.5 - 5\text{ mm}$) TIG arcs a precision of about $\pm 0.1\text{ mm}$ is needed to ensure a proper welding.

1.4. Personal Protection Equipment

The welding process causes high radiances over a variety of wavelength from infrared over visible light to ultraviolet rays with wavelengths from 350-800 nm. The spectral irradiance - an example is shown in figure 1.6- highly depends on the used process, material and gas as the light is produce like in an electric discharge lamp. The visible light of a welding arc is much too bright for the eye and causes flash burns. The infrared radiance causes burns due to overheating the skin and eye with the danger of coagulation causing tissue injury. The last and most dangerous radiance is the UV spectrum which causes skin cancer, painful sun burns on the skin and horny skin (cornea) of the eye [7].

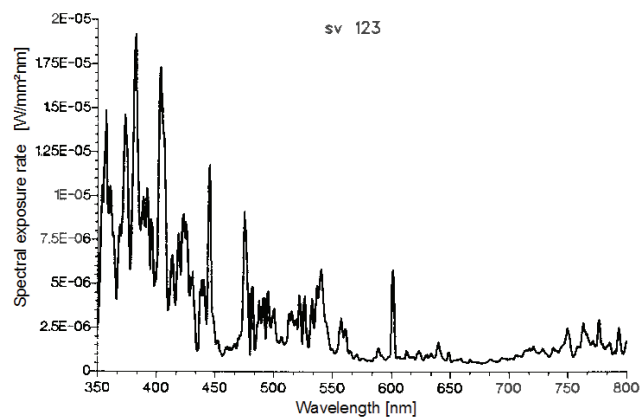


Figure 1.6.: *Example of spectral irradiance for MAG welding of mild steel with a mixture of argon and carbon dioxide (18%) at 100 A*

1.4.1. Passive Filters

During the welding process the welder has to be protected from these hazards by covering the body with opaque and heat resistant material like cotton or leather equipment. Everything but the eyes must be opaquely covered. The eyes need a special protection as they are needed for observation during welding. Observation situations occur for manual, semi-automated or fully automated welding. If only a short glance is taken for inspection of a running welding

process a simple black glass with a very low transmission will be sufficient from the protection and ergonomic point of view. Some very high professional manual welder prefer passive filter as they claim to have a better view through a one layer passive than through a three to five layer automatic darkening filter.

1.4.2. Automatic Darkening Filter

For the manual welding process where a welder needs to be precise in welding torch handling over a whole working day of eight hours or more, an Automatic Darkening Filter (ADF), is a more ergonomic and thus quality assurance choice. This type of filter darkens automatically a see-through window, if a welding process starts in the surrounding. With an ADF the welder does not have the problem of a permanent merely diaphanous view, like he has with a passive filter. Now a correct aiming to the starting point of the welding seam is easy to find. With an ADF the welder has a good view onto the scene by the inactive shading of the filter. During welding process a safe observance is assured due to the ADF activated shading at an adequate shading level [8]. By shading the complete view by one constant shading level, the limited dynamic range of the eye cannot picture low lighted details of the surrounding, as the arc must be shaded at an high level.

1.4.3. Selective Auto Darkening Filter

The European Union - Marie Curie Transfer of Knowledge Program (TOK) grants under the number MTKI-CT-2005-029652 the project IntARWeld. The IntARWeld project yields, from the point of research, to the improvement of current ADF technique as it is widely used in high-end welding protection. The research activities at Optrel AG ² in Switzerland and the Friedrich-Wilhelm-Bessel-Institut Forschungsgesellschaft mbH (FWBI³) in Bremen (Germany) follow the idea of a Selective Auto Darkening Filter (SADF). This filter shall dynamically darkens the users view only there, where a glaring light source occurs and keep the low lighted regions clear. Such a SADF will protect the welder during welding from flash-burn by shading the areas which overexposes the eye and remains a good view onto the environment by less shading the surrounding. In order to achieve the functionality of a dynamic selective shading one idea is to place a partial shadable filter between the user and the light sources as it can be done with a GLCD. A light source detecting device needs to extract the bright areas in the welders view as they occur in the welders line of sight. A digital camera can sense the view of the welder and thus the bright areas occurring during welding. These cores of the technique give an approach for a SADF setup integrated in a welding helmet. They have to be embedded into the SADF application where they induce the adjacent problems, which will be investigated in the following chapters.

One big issue is the proper extraction of a camera image. The welding process causes an harsh environment with high electromagnetic radiations. The scene has very high contrast

²formerly know as Sperian Welding Protection

³<http://www.fwbi-bremen.de/>

1. Introduction

ratio which is the ratio of the darkest to the brightest area and a fast changing light condition due to the unstable light source produced by the electric arc of the most welding process. These boundaries urge the active control of the camera parameters during welding and an adapted image processing to receive a good view onto the process. Another issue is to build an algorithm for controlling the GLCD for each eye while the camera with its monoscopic view does not have the same stereoscopic view of the user. Additionally the relative pose between the user and camera is not constant between different uses. That is why the issue of precise system calibration needs to be considered. Especially the projective geometry will help to regard the context of mapping the world from 3D to a 2D camera chip and from there to a 2D GLCD which is in the line of sight of the second "camera" called human eye.

1.4.4. Mixed Reality

The SADF concept enables a better access to the welding by supplying a better view. The Mixed Reality paradigm can be seen as the next logical step after improving the user view. The mixed reality paradigm enriches the user view by adding new information. The Mixed Reality continuum (see figure 1.7) as introduced by Paul Milgram [1] gives the opportunity to add any amount of artificial content to the users view. It starts with the pure reality and adds on his way to the virtual reality more and more additional data to the users view.



Figure 1.7.: *Mixed Reality continuum*

The blending of information is mostly done by using a head-mounted display (HMD) widely known as video goggles. These displays do either blend the additional data to the users view while he sees the environment pure naturally. This approach is called optical see-through HMD. The second more simple mode of adding information is to grab the view by camera, add some content and display this video stream to the user, which is called video-see-through mode. If the portion of real view is bigger than the added virtual information, then this is called Augmented Reality (AR). For this video see-through AR can be used to form a new paradigm for Personal Protection Equipment (PPE). A stereo camera system integrated in a welding helmet records the scene and feeds the images to a stereo HMD. The connection is made with a computer system in between the camera and HMD which gives the opportunity to enrich the images with additional data. Here the image acquisition and enhancement plays a central role for the view impression of the user. For the field of welding application the project TEREDES uses this approach. It integrates two cameras in a welding helmet with an intercamera distance similar to the human eye distance (see figure 1.8). These two view channels are processed by two independent computers and shown on a stereo HMD [9], [10], [11], [12]. One problem of this system was the limitation to spray transfer processes due to a limited adaptation of the video system onto other welding processes.

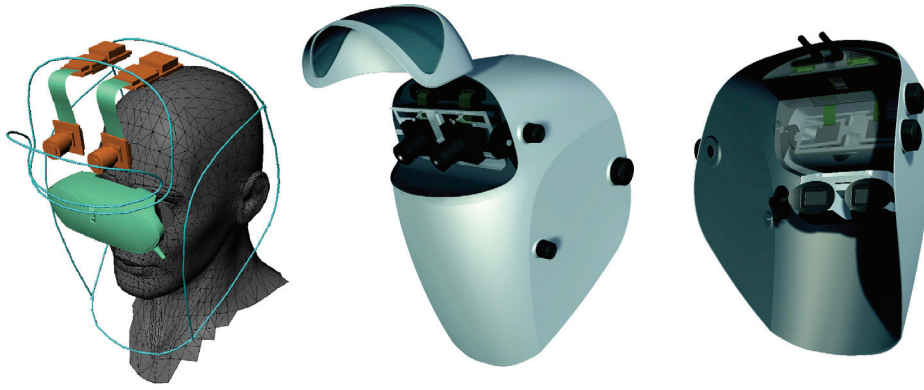


Figure 1.8.: *Conceptional Setup of the TEREBS welding helmet*

Instead of using this paradigm during welding it can be used for a pure virtual welding. The welding piece and the welding torch need to be tracked in order to know the relative pose of these two objects. The relative pose is fed to an welding seam model, which produces a pure virtual graphical rendered welding seam. The seam can be overlaid for the user onto the real physical object by blending it into the HMD [13].

2

State of the Art

In this chapter the problem of welding observation and protection is re-defined by introducing the single aspects of the problem and confining it from other works. It starts with the issue of the human visual system and its sensitivities and regulations. In the next step the aspects of the state of the art related to extract data about the welding process and the visual observation are described. A special section takes care about the image processing problem which consists of noise filtering, image enhancement and high dynamic range increase by merging several shots of the scene.

2.1. Welding Protection

As presented, the welding process produces emission as glaring visible light, infrared and ultraviolet rays. The visible light, which has the wavelength from 400 to 700nm is the one to be dynamically shaded. First the sensitivities of the human eye is taken into account from the physiology point of view. After introducing the functionality of the human eye receptors, a look onto the regulations for welding protection is taken. These regulations, which are the condensed experience for eye protection during welding, give a good impression about what a SADF has to cope with.

2.1.1. Sensitivities of the Human Eye

The human eye with its ability to adjust to different lighting conditions covers the dynamic range of $1 : 10^4$ from the darkest to the brightest point in the scene. Different mechanism

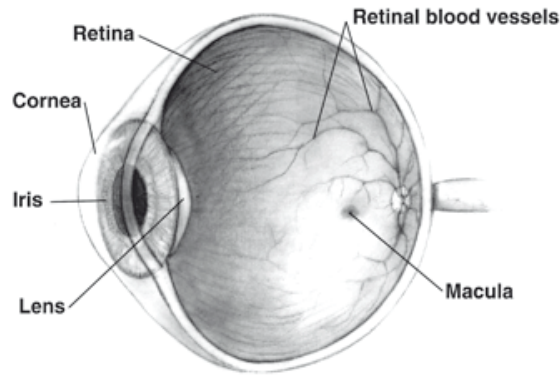


Figure 2.1.: *Human eye cross-sectional view, [Courtesy: NIH National Eye Institute]*

take care about the perception during bright and dim light and one these result in a different resolution from the central point of view to the outer areas of the inner eyes. These issues will be introduced following the needed basics for this thesis following basically [14] and [15].

Anatomy of the Eye Electromagnetical rays in the band of 400 nm up to 750 nm are sensed as light by the human eye. The imaging system of the eye consist from the optical point of view of a lens with autofocus functionality, an aperture provided by the iris and a light reception layer. The light receptive layer can be divided up in the different areas of the retina and the area of the macula (macula lutea) with its inner zone, the fovea centralis (see figure 2.1). The iris is controlled by the incidence of light and the focus distance. It reacts within seconds on changes in lighting conditions. The retina and the macula are covered with rod and cone cells. The rod cells are sensitive to greyscale vision in low dim light, the so called scotopic vision. They include a mechanism for higher sensitivity for low light on the receptive layer inside the eye, where the rod cell are supplied with an amplifier mechanism which decays with the amount of incident light. Their sensitivity maximum is at the wavelength of 500 nm (see figure 2.2). The cone cells cover the daylight vision (photopic vision) and occur in three different types; distinguishable by their maximum sensitivity to the colour blue (420 nm), green (534 nm) and red (564 nm). This results to an overall maximum sensitivity at nearby green at the wavelength of 550 nm .

The retina and the macula with its fovea centralis have different concentration of rod and cone cells. The entire light reception layer consist of about 120 million cones and 6 million rod cells. The retina is covered with a high density of cone cells and a low density of rod cells, hence the retina is specialized for scotopic vision. The fovea centralis inside the macula has no cone cells but a high concentration of rod cells, hence it is specialized for daylight colour view and not useful for dim light conditions.

The perception for two distinguishable objects was first examined 1834 by Ernst Heinrich Weber and augmented by Gustav Theodor Fechner in 1860. The resulting Weber-Fechner law (see equation 2.1) declares that in the case of a linear growing stimulus I_s the human

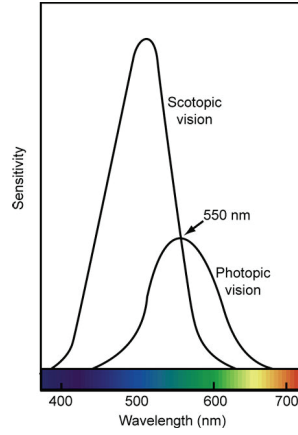


Figure 2.2.: *Scotopic and Photopic Vision* [source:[17]]

sensing organ like the eye perceives a resulting sensing signal (A) by the logarithm of the stimulus.

$$A = k \cdot \log \left(\frac{I_s}{I_0} \right) \quad (2.1)$$

with k depends on the individual eye. I_0 is a critical value for two distinguishable impressions and depends on the adaptation of the eye system. This law results, that the sensing system like the eye uses a logarithmic compression for the signal.

Equipped with these most important mechanisms the eye is able to adapt to light conditions with a ratio of $1 : 10^{11}$ between the darkest and brightest condition. If the illumination is kept constant, the most everyday life situation supply a ratio of 1:40 for the darkest to the brightest object reflectance [16].

Contrast perception The contrast perception of the human eye can be formulated for different boundary conditions. Two neighboured areas, form a border if they differ with the smallest distinguishable difference in brightness. This smallest distinguishable difference depends on the size of the two areas. The smaller the areas are, the bigger must be the difference. But this is not the only variable for the contrast. The problem here is, that it differs with the used colour and slope at the border in between, as well. Another access to this problem is to use different 2D patterns like a sinus with different frequencies f and to measure the perception level of the test person in comparison to a rising pattern amplitude of time (see equation 2.2).

$$P(u, v) = \sin(2\pi f v) \text{ with } u, v : \text{row, column of the image} \quad (2.2)$$

The resulting function is called the modulation transfer function (MDF) of the eye and depends on the age, pupil diameter and eye colour [18]. As an example the MDF is shown in figure 2.3 for a 25 year old blue eyed human with a pupil diameter of 3,8 mm.

Hazarderous effects The hazardous effects of optical radiation on the eye vary significantly with the irradiated wavelength. The discussion about the hazarderous effects can be divided

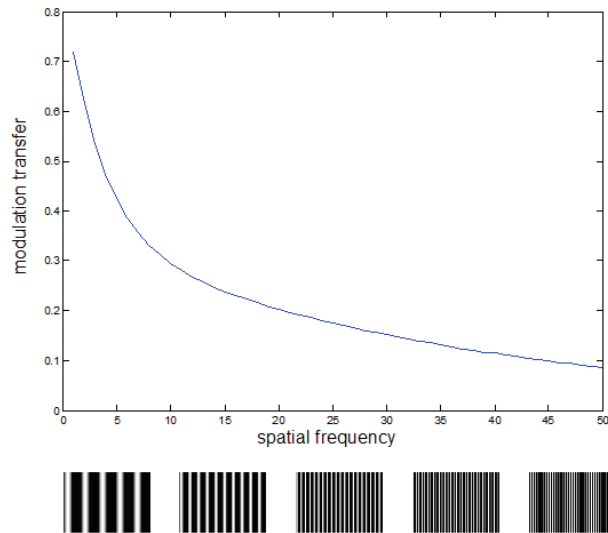


Figure 2.3.: *Modulation Transfer Function*

up into three main parts: The ultraviolet, the viewable light and infrared radiation [19]. The hazards from electromagnetic and magnetic fields related to cancer [20] are not considered, as they are not part of the welders protection using a SADP or ADF.

UV-rays with the distinction of UV-A (315 – 400 nm), UV-B(280 – 315 nm) and UV-C (100 – 280 nm) radiation are absorbed for about 96% by the cornea and the eye-lens. The longer the wavelength of the UV-ray is, the more they penetrate the eye (see figure 2.4). On the cornea mostly the UV-B and UV-C cause photochemical effects which result in a actinic keratosis- that painful effect known as snow blindness or welder’s flesh, which is like a sun burn on the cornea surface. After exposure the discomfort come with a latency between 6 and 12 hours. Symptoms are the reddening on the conjunctiva (conjunctivitis) within the area between the eye lids, a heavy tear flow, high sensitivity to light with a painful uncontrolled excessive blinking and the feeling of having ”sand” in the eye. The recovery takes one or two days.

The UV-A and UV-B rays are transmitted by the cornea and conjunctiva into the lens. A pigment in the lens which is itself a photodegradation product from an UV-B photochemical reaction, absorbs and therefore protects the retina from these rays. Inside the lens this brownish pigment can be accumulated and turn the lens almost black. This process is reversal, so that the opacity may last for some days and disappears if the exposure of the eye to UV-A and UV-B is sufficiently low.

The UV-B and UV-C ray can be easily blocked by a clear plastic or glass panel, so that the hazardeous effect can be minimized without loosing the access to the visual reception of a scene.

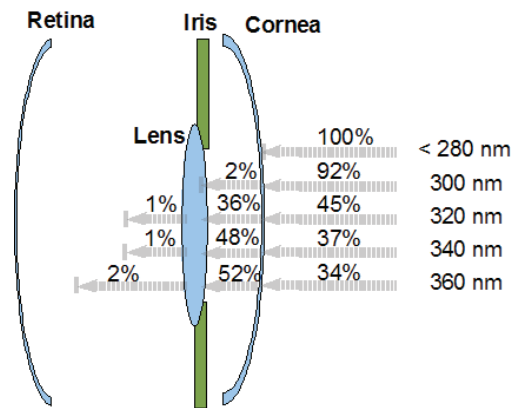


Figure 2.4.: *Schematic of absorption of UV-radiation in the ocular media of the human eye*

Visible and near IR-light in the spectrum of 400 – 1400 nm may harm the eye by retinal burns, which results in a loss of vision. These burns are effected by a too high energy input to the retina. If the retinal cell are to highly heated the protein denaturation affect the retinal tissue and form numb areas (blind spots).

Large temporary changes in visual sensitivity called flashblindness has been intensively investigated. Flashblindness is the effect, of an abruptly overloaded neurophysiological and results in a blindness which is recovered after some minutes.

The eye has its own safety equipment to protect against high radiation. The lid reflex has most smallest reaction time of 0.15 – 0.2 s . Another mechanism is to turn away the head from the line of sight to the glaring or flashing device within about 1 s .

The IR-light is defined in three biologically significant infrared bands with IR-A from 760 – 1400 nm , IR-B band with the wavelength of 1.4 – 3.0 μm and the IR-C band with its radiation from 3.0 – 1.0 μm . The biologic effect on the human visual system are infrared cataracts also known as glass blower or furnaceman's cataract. These cataract is -like the ones at the retina- a denaturation of proteins in the crystalline lens of the eye.

2.1.2. Regulations for Welding Protection

Official regulations for welding protection define the boundaries to deliver the user safe and reliable products for his personal protection. The project IntARWeld with its concept for a SADF, is not part of the European Norms which give the boundaries for welders protection. In order to know which boundaries exist, the according norms for passive shields and ADFs will be contemplated.

The European Committee for Standardization establishes norms for different aspects of eye protection depending on the circumstances of protection. A general specification for personal eye protection is given in the norm EN166. The specific description for eye protection

2. State of the Art

Norm	Title
EN165	Glossar for used terms
EN166	Specifications
EN167	Optical test methods
EN168	Non-Optical test methods
EN169	Filters for welding and related techniques: Transmittance requirements and recommended use
EN170	Ultraviolet filters. Transmittance requirements and recommended use
EN171	Infrared filters. Transmittance requirements and recommended use
EN172	Specification for sunglare filters used in personal eye-protectors for industrial use
EN175	Equipment for eye and face protection during welding and allied processes
EN379	Automatic welding filters

Table 2.1.: *Overview about European Norms [EN] for personal eye protection*

while welding, against an UV-, IR-source or sun-light are explicitly described in separate norms (EN169, EN170, EN171). With respect to welding an additional norm describes the "Equipment for eye and face protection during welding and allied processes (EN 175). In EN379 the boundaries for "Automatic welding filters" are described for ADFs. For defining the used terms for personal eye protection the norm EN165 consists only of a glossar with a description of the terms. Another two norms declare the testing methods for the optical and non-optical test methods (EN167, EN168). An overview about the European Norms for personal eye protection is given in table 2.1.

The level of shading depends on the brightness of the welding arc, which can be seen by the welder. The different welding processes with its material, used gas and the current affect the brightness of the arc. The environmental properties like the material surface (grinded or polished) and the geometrical shape affect the amount of light which is reflected or absorbed. The recommendations given by EN169 consider solely the process and the used current for the arc. In figure 2.5 the reference guidelines from EN169 are sketched in a diagram.

2.1.3. Automatic Darkening Filter

An ADF is like a LCD with one single huge pixel. A compound consisting of an IR-filter plus one or two LCDs gives the basic setup of the optical part. This optical block is connected to an arc detecting device, which darkens the optical block by connecting the LCDs to an electrical AC-signal. Depending on the functionalities of the control unit, the shading level of the ADF can be adjusted manually or automatically. The EN379 enjoins a maximum shading level difference between the open and close state of the ADF which must not exceed nine shading levels.

The technique used in LCDs is based on polarized light. Imagine two polarizers with perpendicular planes of polarizations. In between these two polarizers mostly produced as a thin plastic film, another two glass sheet with a filling of special liquid crystals is set up (see

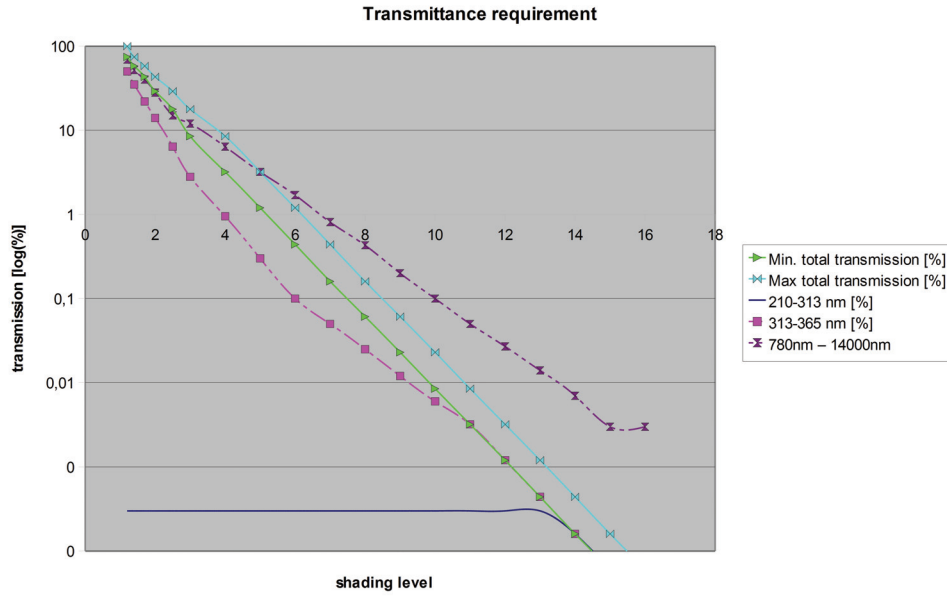


Figure 2.5.: *Transmission requirements for shading level*

figure 2.6). The surfaces of the glass sheets which are in contact with the liquid crystal are coated with a transparent electrode. If no voltage source is connected, the liquid crystals are arranged in parallel to the electrode planes and smoothly twisted about 90° from the one to the other electrode. This smooth twist guides the polarized light from the upper polarizer to the lower polarizer (analyzer) by changing the direction of polarization of 90° (see figure 2.6-A). If a voltage source is connected to these electrodes, an electro-magnetical field is formed and distorts the smooth twist by changing the alignment (e.g. twist and tilt) of the liquid crystals (see figure 2.6-B). For a deep understanding of liquid crystals and polarized light see [21] and [22].

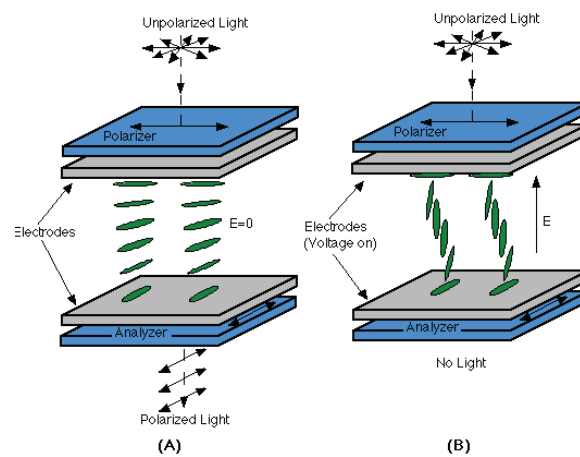


Figure 2.6.: *Principles of LCD using TN technique*

2.2. Welding Process Observation

The welding process observation includes the general documentation or abstraction of data from the welding process. This can be 1D-signals like the current, voltage, wire feed speed, brightness, point temperatures or acoustic. Visual imaging provides a 2D signal which is done by sensing light in a selected spectrum from visible to infrared. Active and passive direct sensing give the two branches of approaches for visual sensing. Active visual sensing uses external light sources like bulbs, lasers or flashing units. The passive direct sensing uses only a camera without any additional light. Using X-rays for documentation is widely used for after process documentation but can be used as well during the process. A good overview about this topic is given in [23].

2.2.1. Process Parameter

The process parameters may give information about the status of the process. In MIG / MAG short-arc welding the voltage to current evaluation may characterize if the arc is melting a metal drop from the electrode or if the liquid metal is detached after the shortcut and travels in direction of the workpiece. For pulsed MIG/MAG process the extraction is harder as the machine and not the process controls the signal. By that it happens that irregularly the energy during one pulse is not sufficient to detach a metal drop. The voltage change during detaching is not robustly visible in the impulse signal. The wire feed speed is directly mapped to the current. A so called synergy diagram defines the best current for the selected process related to wire feed speed.

The measured temperature of the weld pool may give information about the penetration depth of the welding process. Sensing the temperature with an IR point sensor and modelling the heat transfer in the work piece, makes a control of a gas tungsten arc welding and submerged arc welding feasible [24].

Sensing the spectral optical emissions of the process is used in [25] to control the energy in the process. By sensing the spectral lines of the light emissions caused by the gas and the metal vapour the difference of these two signals give information about the heat in the process. The control lowers the energy, if the metal vapour emissions gets dominant while the gas light emissions gets low.

2.2.2. Visual Observation

The visual observation can be subdivided related to the setup into active - with external light- and direct passive -without external light- observation. Applicable used sensors are sensor based on the Charged-Coupled-Device (CCD) or C-MOS technique.

Active Observation

Active video observation uses external illumination to extract scene information. It does not need to be automatically a light source which lights the entire scene as it is used for 3D extraction for seam tracking by laser triangulation.

Laser Triangulation Laser triangulation techniques are used to extract a 3D line profile information of the workpiece. These scanners survey the post or pre-process area of the welding by projecting a laser line pattern onto the surface and grabbing the deformation of the laser pattern from the original pattern with a camera. By knowing the (calibrated) position of the light source, the deformation of the line pattern is sensed to conclude the height information of the workpieces surface. The laser line patterns can be straight lines [26], [27] or circular projections [28]. If positioned in the pre-process area a guidance information for the welding torch may be extracted. If this sensor system is mounted to survey the post-process area, then information about the welding seam quality can be abstracted. Depending on the used camera the minimal distance to the welding arc differs on the used camera and laser type. The average minimal distance lies around 25 *mm* before or after the welding arc [29].

Laser lighting The laser may be widened and illuminate the entire scene, which results in a uniform lighted scene. Lighting the process area with monochromatic laser light gives the ability to bandpass it through a filter in front of the camera lens, so that exclusively the reflected laser light represents the camera image. The choice of the laser and by that the wavelength of its light depends on the emitted light of the welding process. The welded materials and dominantly the gas changes the emission of the process. A high quality image may be achieved and can be utilised for visual measurement to characterize the process [30] or to implement a welding seam tracking functionality [31].

Visible Light Flashing with visible light enhances the light conditions for the camera. In [32] a stroboscope is mounted as backlight to achieve a better foreground to background contrast of the electrode and metal drips. The system is used to show in a statistical approach the travel path of metal drips in gas metal arc welding.

The sensing of the resulting welding seam is done in [33] where a stroboscope at a post-process position is installed to extract the welded area and to evaluate it. This system has no direct welding observation but still has to cope with high intensity changes from the arc during welding.

Passive Direct Observation

For a passive direct observation of the weld pool without any external lighting, different approaches exist. In [34] a CCD camera inspects the weld pool from the top through the welding torch with the wire electrode in the middle. This coaxial view onto the weld pool suppresses the direct view onto the welding arc. The contrast dynamics in the scene are minimized and can be recorded by the CCD sensor.

Meanwhile the extinction of the welding arc in a short arc welding, the contrast dynamic is the lowest during the process. At that moment it can be used to acquire an image of the welding pool and achieve good quality images [35].

The idea of bandpassing specific wavelengths as done with a laser lighting, can be transferred to avoid too high contrast dynamics on the camera chip. An IR filter in front of the camera lens filters the visible light and remains the important information from the high temperature welding pool. An implementation of this technique is described in [36] where it is applied to a TIG process to control the weld pool size. The same idea is applied in [37] where it extracts information about the weld pool size with for aluminium alloy welding. A general overview about this topic with the focus of work on Chinese research is given in [23, chapter 1].

Charge-Coupled-Device Cameras

The basic principal of a Charged Coupled Device (CCD) camera is the collection of photon induced electrons in a bounded area within a predefined time. An array of light sensitive cells integrates the amount of light, which falls onto every single picture cell [pixel] of the sensor. By that an optical image projected by a lens system is converted to a digital image, which can be processed with the computer. The single pixels use the inner photovoltaic effect. This effect produces free electrons by pushing an electron from the valence band to the conduction band in silicon. The probability of a photon to be dissolved rises with its energy, which depends on its wavelength (see equation 2.3).

$$\begin{aligned} E_{Photon} &= h f & \text{Frequency :} & f \\ &= \frac{h c}{\lambda} & \text{Wavelength :} & \lambda \\ & & \text{Planck's constant :} & h := 6.626 * 10^{-34} Js \\ & & \text{Light Speed :} & c := 2.997 * 10^8 m/s \end{aligned} \tag{2.3}$$

The photon absorption depth up to which 90% of all photon are absorbed, is connected to its energy and therefore wavelength. High energy photons like in the band of UV light are absorbed directly under the surface or already in the covering glass of the chip. Visible light is absorbed deeper inside the chip while far IR light may pass through the thin CCD-sensor (see figure 2.7). The sensitivity of a CCD starts with a wavelength of 400 nm up to 1100 nm. Related to the human eye the sensitivity in the IR band is higher and this may be used for night vision.

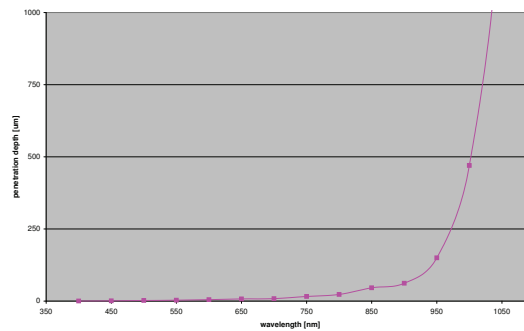


Figure 2.7.: Depth up to which 90% of Photons are absorbed depending on wavelength

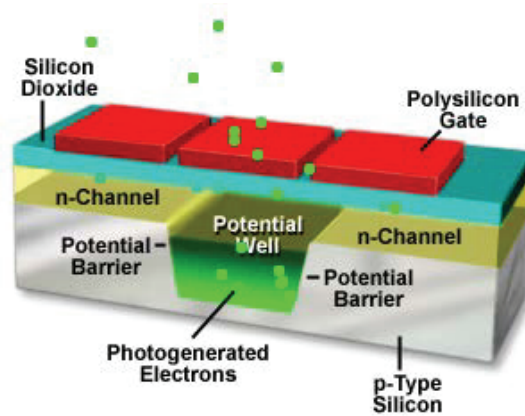


Figure 2.8.: Inner Photo Effect for a Pixel on a CCD-sensor [courtesy: Olympus AG]

The setup of a CCD-chip consists of an array of light sensitive devices, which collect the photogenerated electron by a MOS over np-contact Diode (see figure 2.8). After every readout the collected charge of the pixel is reset. One problem of CCD technique is the blooming and smear effect. The blooming occurs while the amount of light -and thus the amount of charges- gets too high for the pixel and the surrounding regions are flooded by these affluent electrons. In the image it is recognized as a blooming white area. The smearing effect can be deduced from a traditional analogue film camera with its exposure time. The image will be blurred on the film if the scene changed too much during exposition. The CCD sensor has an equivalent to the exposure time. Within the integration time of the sensor, changes in the lighting conditions or scene effect the pixels of the sensor. The effect is that the contours of the objects occur not sharp or smeared. The dynamic as the ratio between the darkest to the brightest area in an image, which can be mapped by a CCD ranges up to 58 db.

High Dynamic Range Sensor

The mapping of high dynamic contrast to a digital image, implies a change in data compression from absolute to relative scaling. Discretization of linear analogue measurements project the absolute values to a digital scale. The available scale of e.g. 256 grey values, is linearly used independently from the range. If an 8-bit digital output is used for the maximum brightness of 100 *lux*, then the slope of the linear analogue to digital conversion is 2.56 digital numbers per lux. At maximum white two pixels with 10% difference i.e. 100 *lux* and 90 *lux* have a difference as digital numbers of 25 which can be easily detected. A 10 % difference one decade lower which then are two pixels seeing 10 *lux* and 9 *lux* results in the digital difference of 2.56 digital numbers or rounded 3 which is barely detectable.

Logarithmic mapping as used by the human eye can compress the data while still supplying an appropriate relative precision. Relative precision means that the relative difference of two measurement does not depend on the range of measurement. For a general optoelectronic conversion function of a camera pixel from brightness x to output y :

$$y = f(x) \quad (2.4)$$

The relative contrast sensitivity ΔC can be stated as:

$$\Delta C = \frac{\Delta x}{x} = \frac{\Delta y}{x \cdot df/dx} \quad (2.5)$$

Which is in the case of a logarithmic optoelectronic conversion function:

$$y = a \ln x \quad (2.6)$$

$$\Delta C = \frac{\Delta y}{a} = \frac{1}{a} \quad (2.7)$$

if $\Delta y = 1$ last significant bit in the case of a digital output.

If now a mapping of N bits for a range of M decades is done, then the mapping function can be written as

$$\Delta C = \frac{1}{a} = \frac{M \ln 10}{2^N - 1} \quad (2.8)$$

Table 2.2 shows the minimum brightness change in percentage to extract a value change of 1 Bit depending on the input contrast range and used number of output bits.

It may be stated that the logarithmic compression is useful to map scenes of high dynamic contrast to a digital image. The sensing element for incident light is selected as silicon photo diodes in Metal Oxide Silicon (MOS) technique. In figure 2.9 the circuit at every pixel on the light sensing chip is shown. The photo diode (D_1) element senses the incoming light and maps it linearly to the photo current. A N-MOS transistor (T_1) is used to map the current logarithmical to a voltage signal (V_{log}). The voltage signal is then amplified by a second N-MOS transistor (T_2). The third transistor is used to select the pixel for readout [38].

The first functional High-Dynamic-Range Sensor prototypes were produced in 1992 and tested for driving assistance in automotive applications [39]. The first chips started with a

Output N Bit	8 bit	9 bit	10 bit
Input M decades			
3 dec	2.7	1.35	0.675
4 dec	3.6	1.8	0.9
5 dec	4.5	2.25	1.175
6 dec	5.4	2.7	1.35
7 dec	6.3	3.15	1.575

Table 2.2.: Contrast sensitivity of the last significant bit in percentage for logarithmic mapping [38]

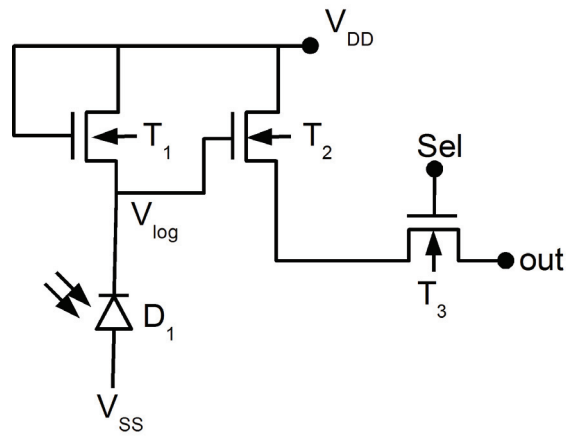


Figure 2.9.: Circuit for one HDRC Pixel

2. State of the Art

resolution of 64 by 64 pixel and reached a resolution of 1024 by 1024 pixels. For the image readout a rolling shutter is mostly available. This means that one pixel line is connected to a sample and hold block before readout. As the photo diode reacts instantly to scene changes, this line by line readout may introduce wrong impressions of the scene. Critical situations exist if rotating or moving objects are observed by the camera. Depending on their relative movement to the camera translated objects are stretched or compressed. High global illumination changes during readout generate an average brightness change of an entire pixel line.

Specific for the high dynamic range C-MOS camera pixels is the fixed pattern noise (FPN), which effects every pixel individually. The FPN depends on the two independent phenomena:

1. Distribution of dark currents for low light levels
2. Distribution at bright levels by the individual transistor parameter like its threshold voltage

The FPN correction can be assumed to be constant in a wide range of illumination. To achieve a good FPN correction during welding, it is sufficient to have a static offset subtraction for every single pixel. The calibration of the FPN correction is done by grabbing a frame of a unicoloured white surface at a bright illumination level. The deviation of every pixel from the mean value of the image is subtracted for FPN correction (see figure 2.10 and figure 2.11).

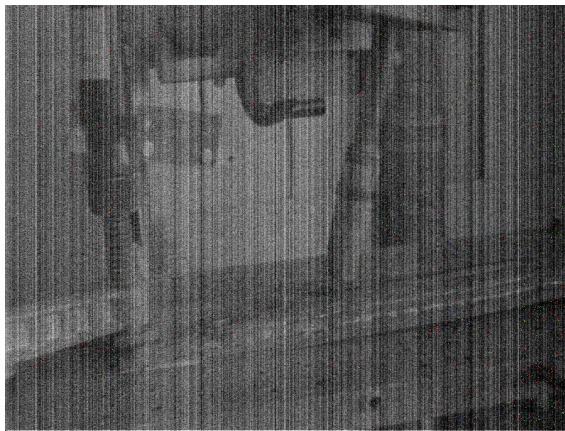


Figure 2.10.: *Image of the automatic test stand without FPN correction*



Figure 2.11.: *Image of the automatic test stand with FPN correction*

Optics

As the High dynamic range camera chip senses relative brightness information already at a low minimum brightness level, the lenses used for CCD camera do have negative effects on

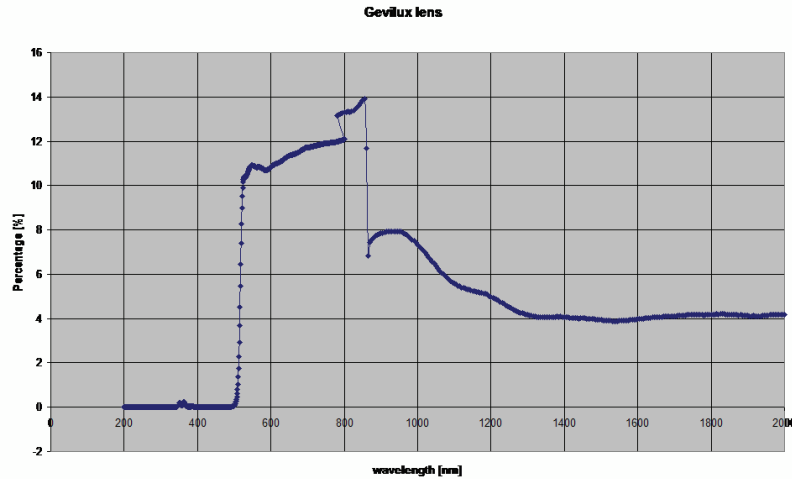


Figure 2.12.: Spectral response of Gevilux lenses [40]

the image quality. The reflection at the annealed glass-air surface are the source for reflex image. The intensity of the reflex images is below the lower bound to be sensed by a CCD camera but are recorded by the logarithmic high dynamic range sensor as ghost images. Lenses for CCD sensor lead to a setup of numerous free-standing lenses where every glass-air surface is a source for ghost images visible for high dynamic range sensors. Theses new boundary lead to a new setup for specialized optics with a minimized number of lenses and high quality reflective coatings [40].

A second change for the boundary conditions is the different sensitivity for near-IR light so that a correct focus for this bandwidth is needed and a lower cut-off frequency is implemented. The figure 2.12 and figure 2.13 show the spectral response of a specialized high dynamic range lense type "Gevilux" from the company gevitec¹ and a standard CCD tube lense from the company QIOPTICS². The differences in the spectral response can be clearly seen. The Gevilux lense has its cut-off wavelength of 550 nm at the bottom and a sharp fall-off at 830 nm for the upper bound, while the CCD lense starts at 400 nm and has a smooth upper blocking.

2.3. Image Processing

The enhancement of images cover the fields of denoising distorted images as it occurs for dim scenes, deblurring of unsharp images e.g. due to movement and enhancing the contrast for compressed scene data. Basic techniques for image processing can be found in recommended books like [41], [14], [42] or [43]. Here the issues for contrast enhancement for low contrast images is visited for global and local operators.

¹GeViTec, Ettlingen, Germany: <http://www.gevitec.de/>

²QIOPTIQ, Asslar, Germany: <http://www.qioptiq.de/>

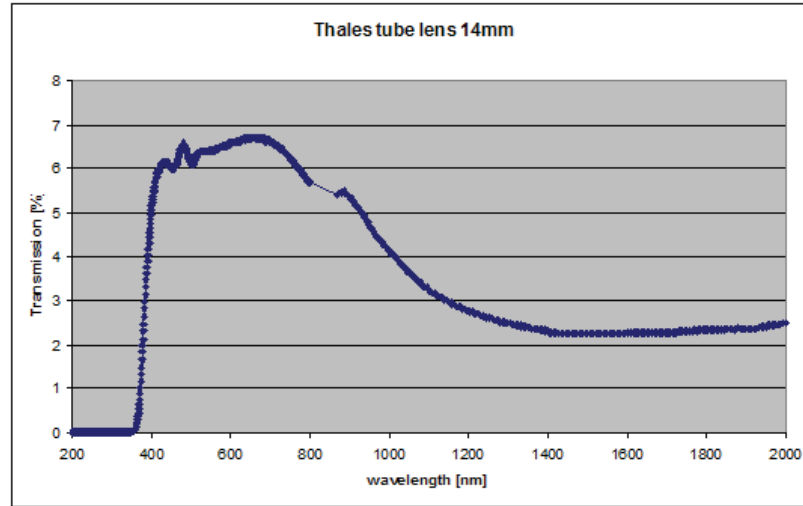


Figure 2.13.: *Spectral response of standard tube lense system*

2.3.1. Spatially Uniform Enhancement

Spatially uniform enhancement normally has the property of being a monotonic mapping. It means that a mapping of a pixel value of the input image to a new pixel value in the output image does not depend on the position in the image. The most classical approach is using the gamma correction for compensating the non-linear luminance response of the eye. Other approaches use logarithmic, sigmoid or bezier function. If the input image does not use the entire available range of pixel values then a histogram stretching to redistribute the pixels among the available values is the basic approach. This kind of image enhancement does not take care about the content of the image. It just redistributes the values either to fit a model (as done with the gamma correction) or to statistically re-distribute the values for a better use of the available range.

The approach called grey-level-grouping by Chen et al. [44] merges the histogram bin with the lowest number of pixels with its smallest direct neighbour and redistributes them to the resulting gap. The contrast is measured by a contrast measurement function. Measuring the contrast of an image is not clearly defined. The used contrast measurement function (Tenengrad criteria) is approved only for grey-level-grouping or other histogram based approaches. The upcoming step takes the resulting image and merges the next bin with the smallest amount of pixel with its smallest direct neighbour, redistributes it and measures the contrast. This is done until a minimum amount of bin remains. At the end the grey-level-grouping assignment is used for the image which maximises the contrast measurement.

2.3.2. Spatially Varying Enhancement

Algorithms which do not apply global mapping functions to an image take care about the local luminance changes. They are based on the widely accepted assumption that the human

visual system extracts information by local and not global illumination changes [45]. This assumption cannot be used for machine vision as it changes the information of the image. The algorithm introduced by [46] refers to the technique of overlapped sub-block histogram equalization, where the neighbourhood of every single pixel is used to calculate the histogram equalization mapping function and to map the single pixel to a new value.

Tiling the image in a predefined number of squared areas which are enhanced independently and merged in a succeeding step, is an approach which integrates a family of similar algorithms [47]. A special implementation is the contrast limited adaptive histogram equalization, which constricts the intensity of the contrast improvement for every tile [48].[49]. All these algorithms are not content based, as they do not consider about the objects, shape, areas etc. included in the image.

2.3.3. Noise Filtering

Existing noise in images is mostly amplified if the image is enhanced. Kernel based filtering techniques often use a gaussian kernel, which filters noise and blurs existing edges. Using the median instead of the weighted mean is popular to be used for salt and pepper noise [14]. The 2D Wiener filter described by the cybernetician Norbert Wiener in [50] -an optimal filter- uses an a priori know noise model. Although its optimization approach minimizes the still existing blurring of the image, the precise real noise is seldom known.

An edge preserving techniques exist with the bilateral filtering. which is a combination of two filters. The influence of a neighbourhood pixel is weighted by its distance similar to the gaussian filter and second its colour difference to the center pixel [51], [52]. Another edge preserving and robust approach is the mean shift filter, which calculates for every single pixel the governing mean shift using a kernel density estimator, shifts the kernel by this value, until it converges to a local extreme point where the mean shift equals zero [53]. This algorithm will be introduced and applied more deeply in the following chapter 3.

2.4. High Dynamic Range Increase

The abbreviation HDRI has two denotations. One is the meaning of High Dynamic Range Increase as a technique to merge a number of differently exposed images in order to retrieve a higher dynamic image and secondly has the meaning of a High Dynamic Range Image.

Before going into deep into the subject of High Dynamic Range Increase [HDRI], the basic and concept of High Dynamic Range Images shall be introduced:

The dynamics of images is connected to a set of techniques for representing, displaying and building images without the boundary of a fixed amount of available colours. Very common for representing images is here the storage of either 8 Bit grey scale, which gives 256 grey

2. State of the Art

level or a palette of three channel coding using the colour channels red, green and blue (RGB)³.

Using here 8 Bits for each channel, results in 16.777.216 different countable colours. This paradigm of clearly discriminable countable colours, is abolished or at least abated in the field of high dynamic range images by using floating point numbers -or any other adequate type. By that the opportunity to calculate pixel values covering a range of values⁴ and not a predefined set of values [15].

It is comparable with the step made from the set of natural number \mathbb{N} to the set of rational numbers \mathbb{R} from number theory.

Instead of using integer values with their fixed step size between different colours or grey values, a floating point value is used in order to allocate the abilities for a more precise image mapping. By providing such a data domain, an infinite number of colour steps is available. If we take the dynamic of an image as the number of available steps, an infinite number of dynamic can be mapped to the image. As an example a grey value image with 256 grey levels has an maximum light dynamic between the minimum and maximum value of 1 : 256. Now assuming the minimum value defines the smallest step size and expand the data to a floating point with any desired precision, then the light dynamic is enhanced to an infinite available dynamic.

This representation of an image as the fundament of the new paradigm has to be aligned to the opportunities of the available display devices. Looking at a high dynamic floating point greyscale image, with the unlimited ratio between the smallest (darkest) and brightest pixel value produces a theoretical unlimited contrast ratio that can be stored. Normal technical limitations, as every technical system is limited, makes it impossible to fully display this contrast. This means a mapping between the unlimited representation with its undetermined minimum and maximum values and its display device is an immanent need for the HDRI technique. Additionally for this "tone mapping" called operation, the human eye needs to be comprised. Its response curve, following the Weber-Fechner law describing the relationship between the physical magnitudes of stimuli and the perceived intensity of the stimuli for the eye (see equation 2.1 take non-linear mapping into account for maximizing the sensation of viewing.

Nevertheless the term High Dynamic Range Increase (HDRI) is widely used in photography for merging a number of differently exposed images. Images are taken from an identical viewport and each one covers a specific bandwidth of light dynamic. The widely used idea from Debevec [54] calculates the camera chip response function in order to remap the pixels of the different shots to the radiance map of the environment. The knowledge of the exposure time is here indispensable for the algorithm. The resulting image contains the complete bandwidth of light dynamic covered by the single shots.

³The RGB colour space is only one of many. It is presented exemplary for the available colour spaces

⁴It may be stated that a variable of type floating point represents a set of countable values due to its binary representation in the computer

2.4.1. Recovering Radiance Map

For merging the single differently exposed images their radiance map needs to be recovered. Following [54] the exposure time of a single image j is chosen by Δt_j and it is assumed to have a static scene and the film irradiance values E_i for each pixel i are constant. The pixel i.e. the grey level values can be denoted by Z_{ij} where i is the spatial index of the pixel and j is the index over the exposure time Δt_j . The film reciprocity equation may be stated as:

$$Z_{ij} = f(E_i \Delta t_j) \quad (2.9)$$

with E_i as the radiance value on the film (chip).

The assumption of its monotonical behaviour give the existence of the inverting function:

$$f^{-1}(Z_{ij}) = E_i \Delta t_j \quad (2.10)$$

$$\ln f^{-1}(Z_{ij}) = \ln E_i + \ln \Delta t_j \mid g(\cdot) := \ln f^{-1} \quad (2.11)$$

$$g(Z_{ij}) = \ln E_i + \ln \Delta t_j \quad (2.12)$$

The values of Z_{ij} are known, as are the Δt_j while the irradiances E_i and the set of functions $g(\cdot)$ are unknown.

The recovering process includes these two issues E_i and $g(\cdot)$ that best satisfy the set of equations arising from equation 2.10. in a least-squared error sense. The recovery of $g(\cdot)$ only requires recovering the finite number of values that $g(\cdot)$ can take, as the domain of available pixel values is finite. Let Z_{min} and Z_{max} be the minimum and maximum occurring integer pixel values, then the problem can be formulated as to find the $Z_{max} - Z_{min} + 1$ values for the function $g(\cdot)$ for the N selected spatial distributed pixels with its corresponding irradiance E_i .

This problem can be written as the least square minimization problem of N equations for the P different images:

$$0 \approx \sum_{i=1}^N \sum_{j=1}^P [g(Z_{ij}) - \ln E_i - \ln \Delta t_j]^2 + \lambda \underbrace{\sum_{z=Z_{min}+1}^{Z_{max}-1} g''(z)^2}_{\text{smoothness term}} \quad (2.13)$$

The smoothness term to emphasize a low curvature is chosen as:

$$g''(z) = g(z-1) - 2g(z) + g(z+1) \quad (2.14)$$

The smoothness has to be chosen appropriately for the amount of noise expected in the measured pixel value Z_{ij} .

2. State of the Art

This overdetermined system of linear equations is robustly solved using the singular value decomposition (SVD) method. By using SVD a solution for the values of $g(\cdot)$ and E_i can only be determined up to a scale factor. An additional constraint will fix the pixel in the middle between Z_{min} and Z_{max} having unit exposure

$$g\left(\frac{Z_{min} + Z_{max}}{2}\right) = 0 \quad (2.15)$$

To make the solution more smooth at the center of the curve, a weighting factor is introduced. Its shape is a simple hat function:

$$\omega = \begin{cases} z - Z_{min} & \text{for } z \leq \frac{1}{2}(Z_{min} + Z_{max}) \\ Z_{max} - z & \text{for } z > \frac{1}{2}(Z_{min} + Z_{max}) \end{cases} \quad (2.16)$$

With the above the equation 2.13 becomes now:

$$0 \approx \sum_{i=1}^N \sum_{j=1}^P \{\omega(Z_{ij}) [g(Z_{ij}) - \ln E_i - \ln_{\Delta} t_j]\}^2 + \lambda \sum_{z=Z_{min}+1}^{Z_{max}-1} [\omega(z) g''(z)]^2 \quad (2.17)$$

Summarizing this equation means to solve the overdetermined system based on the input of several P images where N well distributed pixels are taken from. The values of the pixels are weighted by a hat function and the complete smoothness is carried out by the term instantiated by the second derivative.

As the amount of overdetermination does not require to use every available pixel, the amount for 256 grey scale levels needs to be selected. As an example for 11 different exposed images [54] suggests the selection of 50 well distributed pixels from areas with low intensity variances in order to assure a constant radiance on the pixel area and to minimize the appearance of optical blur due to the imaging system.

Now after the response curve i.e. the mapping of the pixel with its assigned exposure time Δt_j to the natural logarithm of the irradiance E_i can be used to recover the radiance map of the image.

$$\ln E_i = g(Z_{ij}) - \ln_{\Delta} t_j \quad (2.18)$$

For robustness and noise reduction all available pixel values for a certain spatial position shall be used. The pixel values are weighted the more their value aims the mid-range of the greyscale. Due to the weighting function, blooming artefacts are suppressed as their pixel weight is low due to its border position. The formerly introduced hat weighting function $\omega(Z_{ij})$ will be used here.

$$\ln E_i = \frac{\sum_{j=1}^P \omega(Z_{ij}) (g(Z_{ij}) - \ln_{\Delta} t_j)}{\sum_{j=1}^P \omega(Z_{ij})} \quad (2.19)$$

One of two major problems here is that by taking single successive shots the scene has to be static. Changes of the scene in between the single shots bring the problem of ghost artefacts

if objects move and occur at different positions in the images (like moving people or tree leaves do). One approach as presented in [55] tries to warp pixels for successive frames by dividing up the successive images into corresponding regions. For these corresponding region the homographies are calculated. This technique fails if the movements are too big between the single shots. A more simple and reliable technique is described in [15]. The detection of ghost is based on the fact that each single shot is self-consistent, which means that all information appear more or less in every image and that in regions of ghost the calculation of pixel merged from different exposure is turned off and the image with the best quality in that region supplies the pixel. It is done by computing the variance based on a weighted average from the already merged and low scaled image. Now all regions where the variance exceeds a threshold and area are defined as regions with a ghost. For these regions the substituting original data is taken individually from the best available single shot.

The second problem are the global movements of the camera system, which can be easily aligned for translation by using a pyramidal approach to align the image from coarse to fine as suggested in [56]. Movement with complete 6 degree of freedom (DOF) can be done by calculating the homography between the images.

So, more information of the real scene is stored in an image than before by a single shot from the camera. The new problem arising is how to display this information enhanced data, due normal available displays like LCD/TFT have a maximum contrast ratio of $1 : 10^3$, which is much lower than a contrast ratio of $1 : 10^6$ as it occurs in the natural world. If a HDRI shall be displayed it needs to have a dynamic as much as the monitor can display and as distributed as the human eye can perceive. For that different tone mapping algorithms are suggested to keep the stored information available for the human viewer [57], [58], [59]. These algorithms can be divided up into fast global approaches and cost intensive local operators.

In figure 2.14 the content of the thesis is shown on a high abstraction level using a mindmap. The two aims of welding protection and observation form the two main branches. The green sub-branches emphasize the subjects beyond the State-of-the-Art. The new application of SADF and by that the use of a GLCD has not been done yet. The problem of synchronizing the camera onto the welding arc without depending on the welding machine or process has not been solved yet. All solutions used the measured voltage or are directly connected by wire to the welding machine [32]. The trigger drives the camera and a supporting miniaturized light sources like they are newly available by high power LEDs. The contrast enhancement for an image where the most important information is stored in the minority of the pixels like the welding arc, contradicts one of the most basic assumption that the image information is stored in the majority of occurring grey values. So here a deeper investigation is needed.

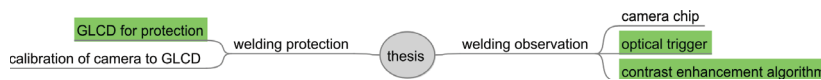


Figure 2.14.: *Subjects of the thesis beyond the State-of-the-Art (with green background)*

3

IntARWeld system

In this chapter 3 the setup for achieving valuable high contrast welding images and the Selective Automatic Darkening Filter (SADF) system for the IntARWeld project, as introduced in chapter 1.4.3, is presented.

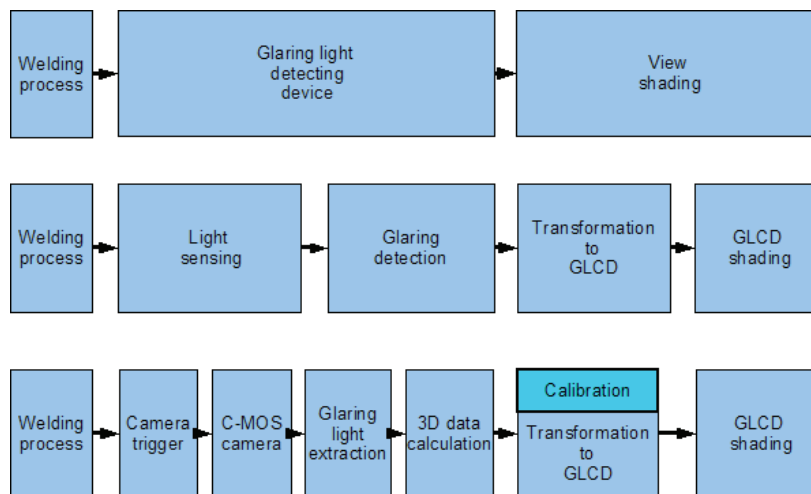


Figure 3.1.: *Top-down approach for a SADF setup*

The conceptual design of a SADF system can be built up by using a top-down approach where the view onto the system starts on the highest level of abstraction of the entire system. It goes down to a finer granularity for modularizing to subsystems (see figure 3.1). This approach starts by dividing the problem up into a sensing and actor unit for the glaring light detection and view shading on the highest abstraction layer. A sensor needs to detect the position of the glaring lights from the welding process and the actor shades the corresponding point in

the welders view. By selecting a specific sensor, the sensing task needs to be split up into a sensing hardware part and an algorithmic arc detection. As well as the view shading may be subdivided into a proper projective transformation from the glaring light detecting device to the shading device and the shading itself by a physical device. Choosing the devices by using an high dynamic range camera for sensing and a graphical LCD (GLCD) for shading, other additional tasks have to be defined for a proper use of the hardware. The camera hardware needs a synchronization to the welding process and the glaring light detection needs the extraction of the glaring light. In order to know the constant transformation between the camera and users view through the GLCD, it is needed to calculate a proper a priori calibrated transformation. The transformation for compensation of the parallax error is needed in every case as the camera cannot be in the same line of sight as the welders eyes.

For the welding observation of the IntARWeld system, a high dynamic grey scale camera is used. Two approaches to receive a good image are implemented. One approach uses the sensed camera image and applies image enhancement techniques to make all available information visible for the user. A second approach uses an alternating acquisition of images taken with different camera parameters. These are merged for the resulting image. The merged image contains already an higher amount of information than displayable by standard monitors and that is why a basic linear tone mapping operation is applied before displaying. Both approaches need a synchronization of the camera to the welding process if others than MIG/MAG spray transfer arc or DC-TIG processes shall be recorded.

3.1. Image Acquisition

The image acquisition is related to the use of the FuGa1000 camera chip and its implementation in the camera system as provided by the company Falldorf GmbH ¹ (Bremen). However, the eight bit A/D converter used in the implementation and the so called rolling shutter cause problems which will be explained in the following sections.

3.1.1. High Dynamic Range Camera System

The selected Falldorf FuGa1000 camera does not directly supply the complete available data as digital data. In a first step an offset is added to the analogue signal and amplified by two independent analogue amplifiers. The analogue signal is then converted by an 8 bit analogue/digital converter (see figure 3.2). The range of the A/D converter is fixed to the range of 2 Volts. Pixel values which exceed this upper border are clipped to the maximum pixel value of 255 and pixels which undershoot due to the applied offset the value of 0 volt are clipped to the pixel value of zero.

¹<http://www.falldorfsensor.de/>

The selection of the amplification and offset has to be chosen as a trade-off between good stepping and covering the range of the pixel signals without clipping any important information to the pixel value of 255 (white) or 0 (black). This means if a high dynamic scene with its broad signal range will be amplified with an high analogue gain, then the upper voltage pixels containing the welding arc information may be clipped to the maximum digital value of 255.

The limitations of the A/D converter urge to adjust the camera parameters during welding depending on the image data. The offset is selected to have an overall pixel mean value of 128.

Lenses Another usually unconsidered issue is the fact that a high dynamic contrast range camera needs lenses which may be used for high contrast with high luminous flux. The lenses applied for CCD or photographic film camera do not have to cope with such highly changing irradiances at once as their field of application does not contain such scenes.

The boundary conditions for a typical CCD camera are

- a relative low lens contrast of maximum $1 : 10^3$ or $60dB$,
- no low intensities of light,
- an equal or smooth illumination in the image field,
- a system immanent linear response curve of the grey tone conversion.

The boundaries for a CCD camera application contradict the new field of high dynamic contrast range cameras. The boundary conditions for the lenses change significantly as the case of high dynamic contrast range the remaining stray light of the annealed glass can be sensed by the camera. Especially by the glass to air surfaces or at the lens edges, reflections of the scene content are spread as ghost images over the acquired image. A CCD camera chip with its lower sensitivity does not sense these low lighted reflections but with a more sensitive high dynamic contrast range camera they are now sensed and by that visible in the acquired image. An improvement with less ghosts e.g from glaring light sources, is achieved by improving the design boundaries for the lenses. Minimizing the number of free-standing lenses, which minimizes the amount of glass air surfaces, causes less reflections. Maximum

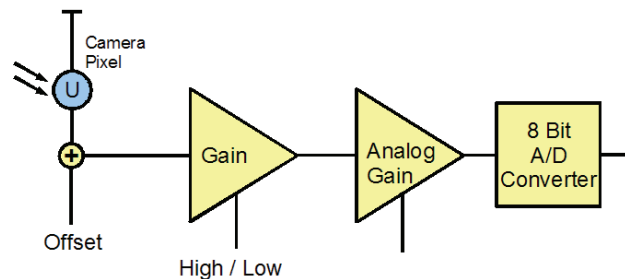


Figure 3.2.: Signal diagram for a single pixel of the used Falldorf FuGa1000 camera

3. IntARWeld system

blackening and matting of all surfaces outside the optical path (e.g. lens holder and frames) as well as using high quality deflective back side coatings, does absorb prospective ghosts before reaching the camera chip [60]. In the IntARWeld system specialized lenses from Gevitec² (Esslingen) of the type Gevilux are used. These lenses lens covers all the presented boundaries for an high dynamic contrast scene.

3.1.2. Optical Camera Trigger

The used high dynamic C-MOS camera chip FuGa1000 from FillFactory³ reacts instantly to the brightness changes during the welding process. This chip does not have an electronic global shutter which may freeze all pixel values before readout and by that maps the lighting conditions and scene view of a single moment. Instead of the global shutter this chip has a so called rolling shutter, which alternates in freezing one single line, does a readout of this line before going further to the next line.

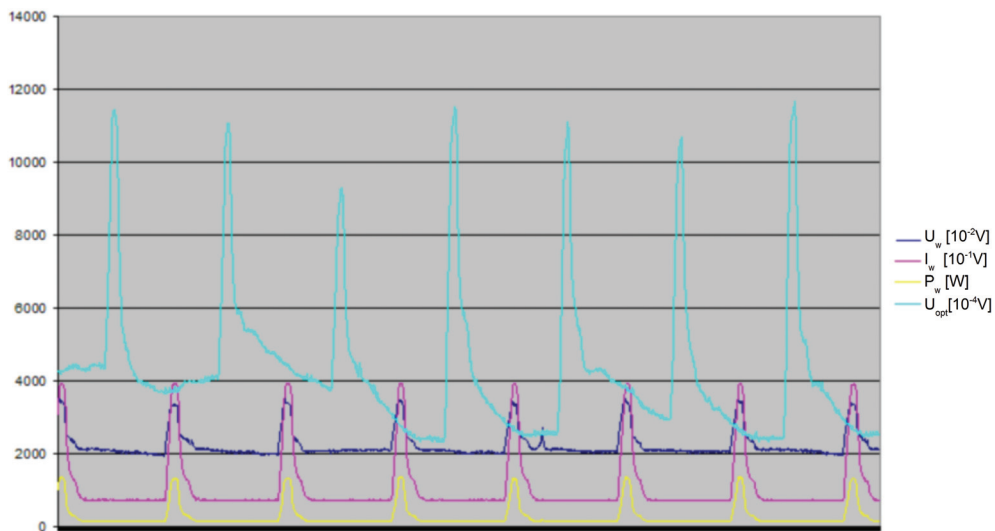


Figure 3.3.: *Impulse Arc: 23 V, 122 A, Gas with 82% Argon and 18% CO₂, mild steel*

Using an impulse or short circuit arc (as introduced in section 1.2) the brightness change of the process is a process immanent characteristic. During every pulse or short circuit the arc becomes brighter and darker, up to a complete extinction of a short circuit arc. In figure 3.3 and figure 3.4 the characteristic voltage U_w , current I_w and optical brightness signal U_{opt} during the welding process for two different arc characteristics are shown. It can be seen that the impulse arc does not extinct but the short circuit arc does. The short circuit arc has a phase of complete darkness before it re-ignites while the pulsed process remains a minimum burning arc over time.

²<http://www.gevitec.de/>

³The company Fillfactory from Belgium is now part of Cypress semiconductors

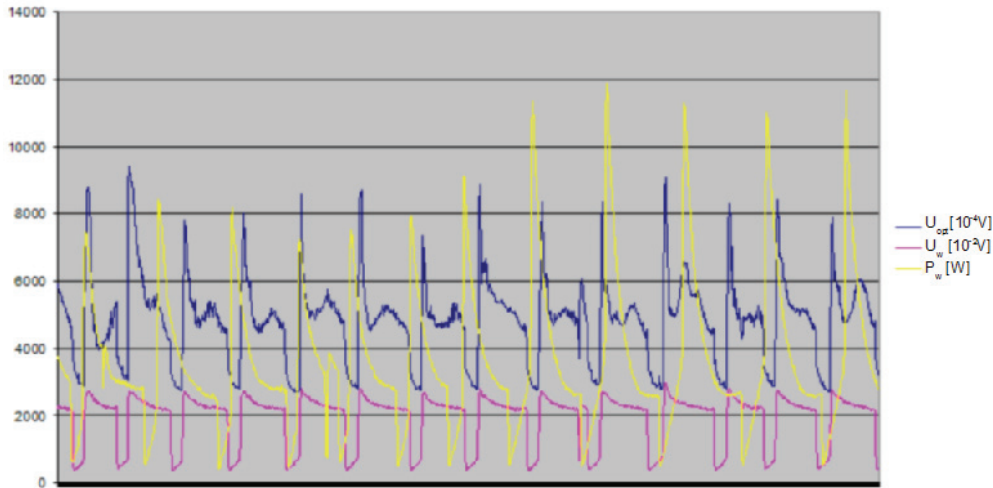


Figure 3.4.: *Short-arc: 22 V, 150 A, Gas with 82% Argon and, 18% CO₂, mild steel*

The light emitted by the arc can be divided into three phases. The peak time is the phase of ignition and bright burning while the electrode melts and a metal drop is formed at the tip. The electromagnetical forces start pinching off the liquid drop from the electrode. After pinching off, the drop is accelerated by the same forces in direction to the weld pool. In order not to accelerate too much the current is attenuated while the arc keeps on burning. After an idle period the process restarts by rising the current, which rises the arc, melts the electrode and so the process repeats (see figure 3.5 and chapter 2).

The brightness change during one pulse causes problems. During the line by line readout of the FuGa1000 camera chip one or more white stripes occur in every single image and add irregular lighting conditions to the image (see figure 3.6). Additionally to the appearance of these stripes in the image, they do not recur at the same position in the image if the welding process and the beginning of the image readout are not synchronized. Hence, if a video stream is taken into account, the white stripe hops from frame to frame to different rows in the images (see figure 3.7). In order to get it stable to one position a synchronization by extracting a trigger for the camera from the welding process gives the opportunity to achieve a better video impression [61].

In the first approach a synchronization signal supplied by welding source is used. The synchronization signal is given for every single impulse, when the arc re-ignites. The biggest shortcoming here is that this signal is only available for machine driven processes. Hence, in this case the camera can only be triggered for pulsed arcs. For a short-circuit arc no signal is supplied, as it is a free running process depending on the short circuits caused by the wire electrode.

In the second approach an optical sensor directly measures the brightness characteristic and uses a trigger criteria on the rising edge or falling edge of this signal. The process supplies a steep rising brightness edge for a pulsed arc, if the arc is re-ignited or forced up. A smoother falling edge exists for the low burning phase. The pulse frequency as well as the up-time of the signal may change during the process due to the changing process parameter by different

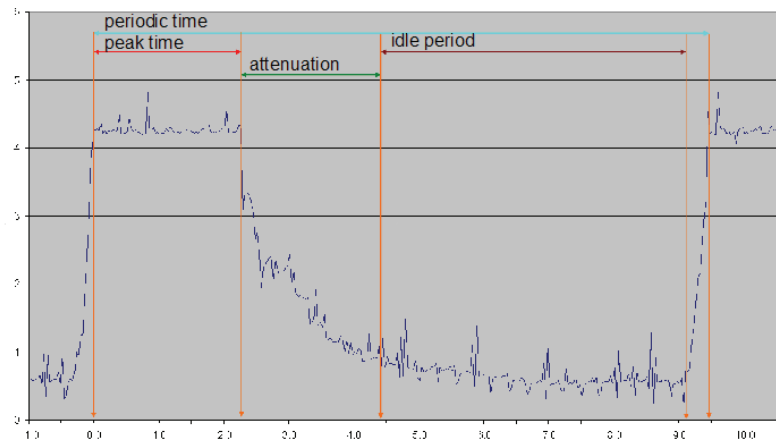


Figure 3.5.: *Phases during an arc segment (pulsed)*

torch distance, seam shape and temperature of the work piece. If the camera is triggered with a delay on the rising edge, then the period of low lighting may not be perfectly exploited as the peak time is not constant i.e. the falling edge is not statically linked with the rising edge. The extraction of the trigger on the falling edge arises the drawback that the smooth falling edge is harder to extract as it is less unambiguous. A concept to accomplish the detection is to use an optical sensor including a signal amplifier, a differentiator and a Schmitt-Trigger (see figure 3.8). The functionality for this optical trigger approach is connected to the brightness of the welding arc. The luminous flux is influenced by the welded material, the used gas, the welding parameters (e.g. voltage and current/wire feed speed) and distance of the sensor to the arc (see table 3.1). So the brightness conditions vary in a wide range. It may cause saturation or low signals for the sensor / amplifier circuit and no trigger criteria is extracted. The optical sensor model OPT101 used in the IntARWeld system is a highly

factor	effect on the emitted light
base material	spectral
electrode material	spectral & intensity
gas	spectral
wire feed speed / current	intensity
sensor distance	intensity

Table 3.1.: *Factors forming the arc emitted light*

integrated solution from Texas Instruments⁴ which includes the sensing and amplification device with a controllable amplification factor. It has been chosen due to its flexible signal amplification and high integration. The trigger extraction concept is enhanced by filtering the amplified signal with a bandpass filter before applying the differentiator. The bandpass

⁴<http://www.ti.com/>

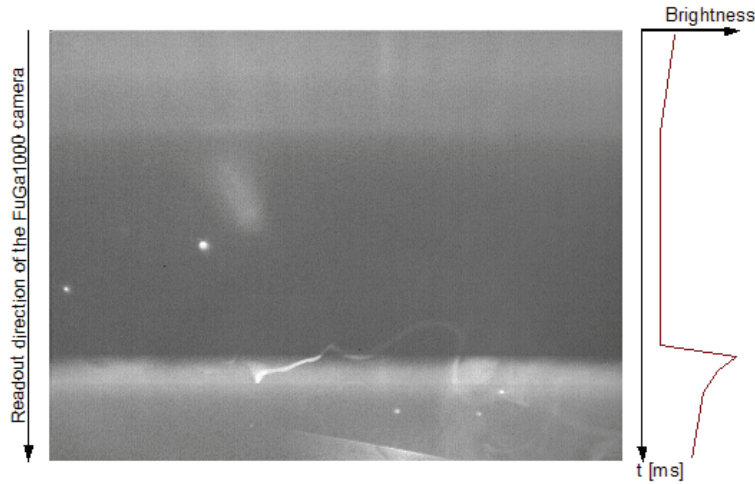


Figure 3.6.: *White stripe in camera image caused by brightness change*

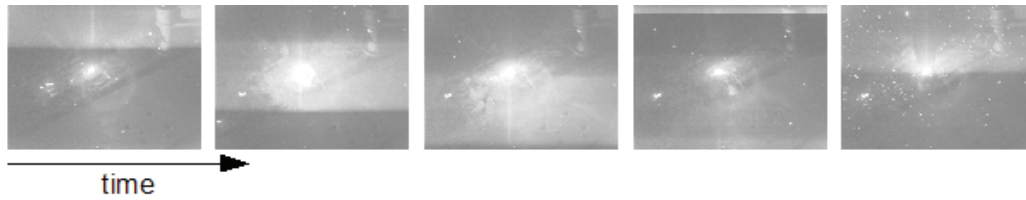


Figure 3.7.: *Sequence with hopping white stripe*

of 28-4000 Hz is used to reject noise from electromagnetic distortions and suppress constant (DC) voltage components (see figure 3.9). A customized inverting Schmitt-Trigger maps the signal to a rectangle logical signal with $U_{up} = 4.1$ V and $U_{low} = 3.3$ V for the upper and lower boundary of the Schmitt Trigger hysteresis (see figure 3.10).

Beside the filtering of the signal from the optical sensor, its amplification factor is dynamically adjusted if no trigger signal is sensed. This may happen if either no welding is done or if the amplification of the optical sensor needs to be adjusted. An additional microcontroller (μC) is connected to the output of the Schmitt-Trigger. If no trigger signal is detected, then the μC produces a default trigger signal to avoid a freezing video. By the start of the default trigger the amplification of the optical sensor (OPT101) is changed by the μC and a count down is started. If now again no trigger signal is detected and the count down expires then the amplification of the sensor is changed again. If all values for the signal amplification have been set one after another the search restarts at the lowest value. But, if a trigger

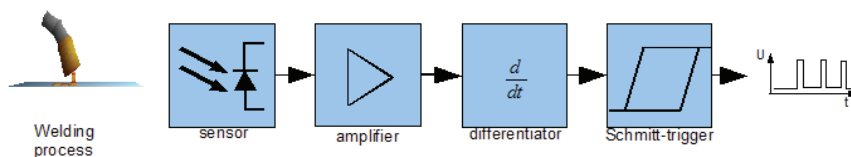


Figure 3.8.: *Simple optical trigger on the welding process*

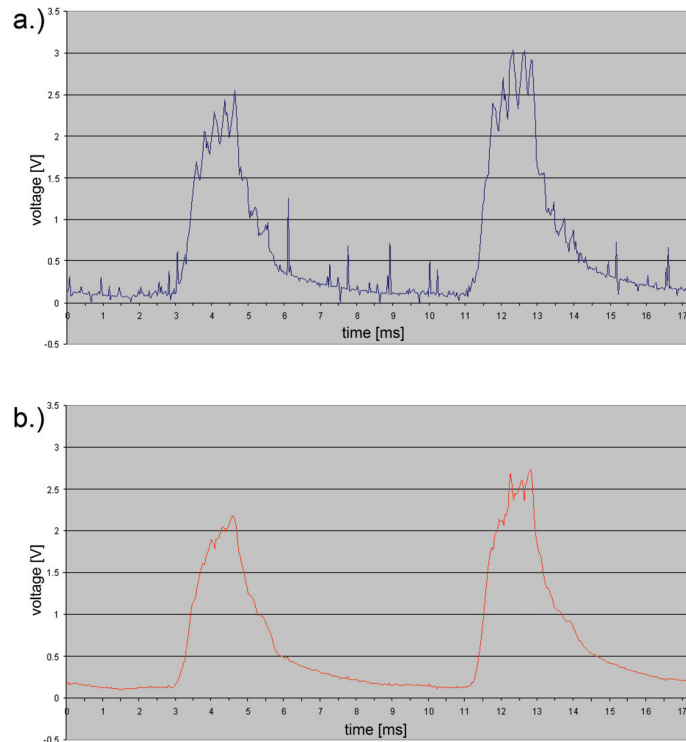


Figure 3.9.: a.) noisy signal from optical sensor, b.) bandpass filtered signal

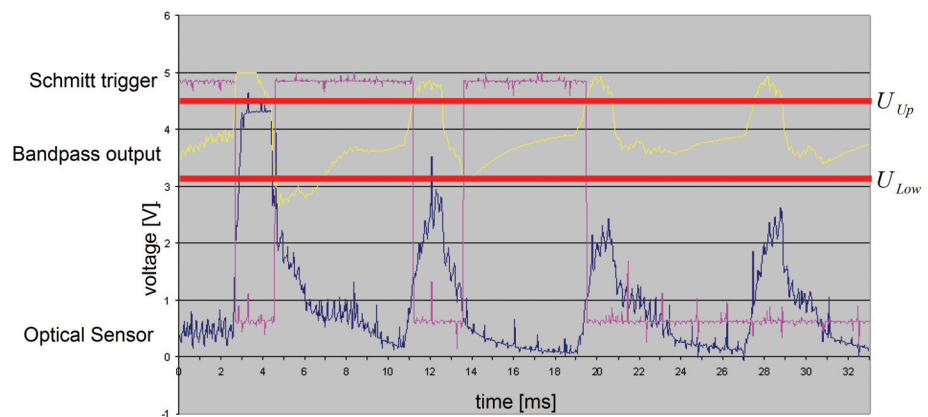


Figure 3.10.: Schmitt-Trigger signal of optical sensor signal

is detected due to the new amplification factor, then the countdown is reset every time a trigger occurs and the amplification is not changed (see figure 3.11).

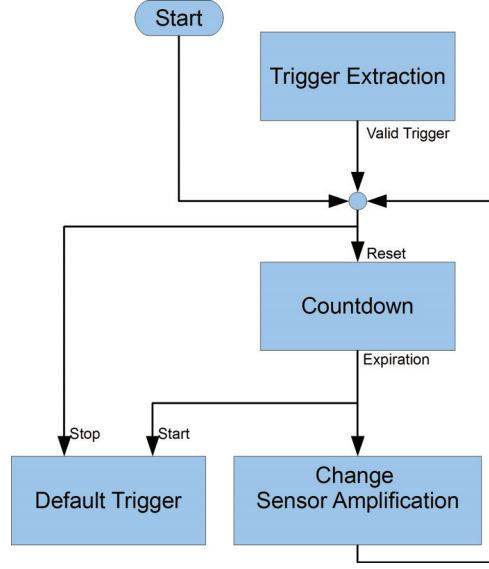


Figure 3.11.: *Sensor amplification control*

3.1.3. Active LED Lighting

In order to enhance the abilities of the camera system, the image acquisition is augmented with an active illumination part. High power LEDs flash the process scene and by that reduce the occurring contrast dynamic of the scene by lighting significantly the low lighted regions. The contrast dynamic d of a scene is the ratio between the darkest areas with its radiance E_{dark} and the brightest area E_{bright} . If additional light is added with the amount E_{add} then the contrast ratio changes to:

$$d_{add} = \frac{E_{bright} + E_{add}}{E_{dark} + E_{add}} \quad (3.1)$$

For the welding scene it can be assumed that the arc as the brightest spot has no reflectivity, so that the equation simplifies to:

$$d_{add} = \frac{E_{bright}}{E_{dark} + E_{add}} \quad (3.2)$$

Accordingly the contrast dynamic characteristic changes depending on the light reflection of the surface. An example how the contrast dynamic changes if additional reflected light is added to the scene is given for $E_{dark} = 10$ lux and $E_{bright} = 10^7$ lux. In figure 3.12 the contrast ratio of a scene is shown as a function of the added light E_{add} . It shows that the contrast ratio may be lowered by one order of magnitude or 20 dB from $1 : 10^6$ to $1 : 10^5$ if the irradiance of the darkest area is enhanced with 90 lux of reflected light.

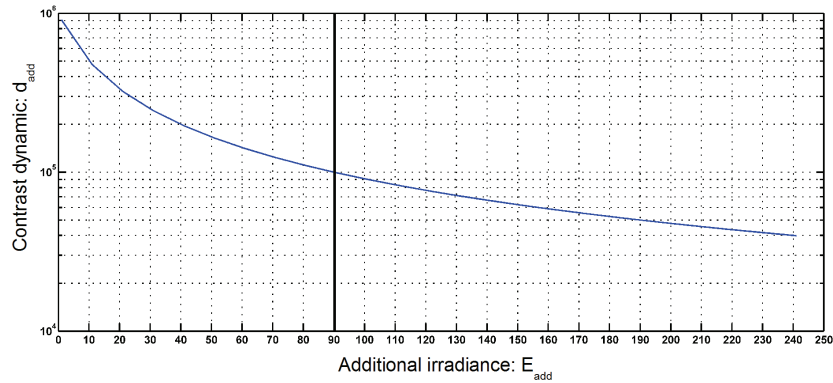


Figure 3.12.: *Change of contrast dynamic by additional reflected light*

A setup with four high power LEDs, as they are available with the XR-E 7090 Q5 LED from CREE lighting solution may provide a luminous flux of 228 lumen (lm) per LED. These LEDs need a backside mounted cooling unit. To achieve a high lux value the LED light is focussed by an condensing reflector (see figure 3.13). In the IntARWeld project two of these LEDs are grouped on an aluminium holder with a circuit board on the backside to operate the LEDs with a constant current regulator (see figure 3.14). Here a LM3404⁵ current regulator from National Semiconductor is used. It has an adjustable output current of maximal 1A, an external control input to enable the LED for flashing and related to the housing size, an integrated MOS-FET. As the LEDs shall be in a fixed position related to the camera and as near as possible to the process, two packs with two LEDs each are mounted onto the welding helmet. The entire setup is covered by an active cooled housing to transport the heat away from the LEDs (see figure 3.15). Spotting these four LED to a unique point and using optical reflectors with a 7° cone angle, the measured maximal brightness in a working distance of 50 cm results in a measured direct illuminance of 4000 lux.



Figure 3.13.: *CREE XR-E 7090 Q5 LED, Cooler and Optics*

Using these high power light emitting diodes (LEDs) gives the ability to flash the scene. They have the advantage to be compact, robust with a small rise time.

If the rise time is not taken into account it causes a not fully lighted scene seen by the camera. Experiments showed that the delay between starting the LED and the camera readout has

⁵National Semiconductors: Data Sheet: LM3404/04HV ; 1.0A Constant Current Buck Regulator for Driving High Power LEDs. <http://www.national.com/>. Version: 2007

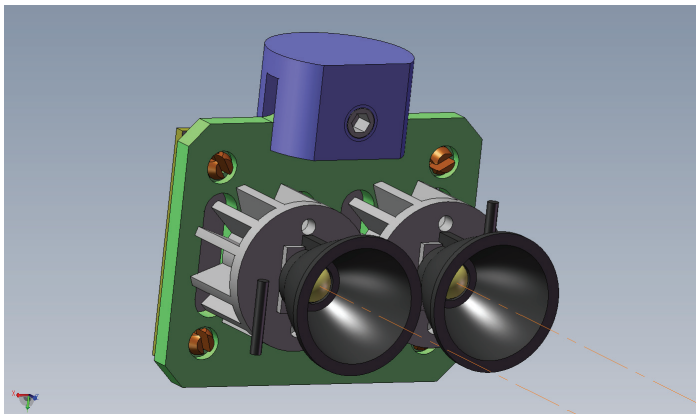


Figure 3.14.: *Lighting unit with two CREE Q5 LEDs*



Figure 3.15.: *Mounting four CREE Q5 LEDs with active cooled housing on a welding helmet*



Figure 3.16.: *Rise-time of the CREE Q5 setup*

to be $16\mu s$ for the used setup with the Cree XR-E 7090 Q5 LEDs and a constant current regulator LM3404. In figure 3.16 can be seen the delay between the input signal and the LED start-up.

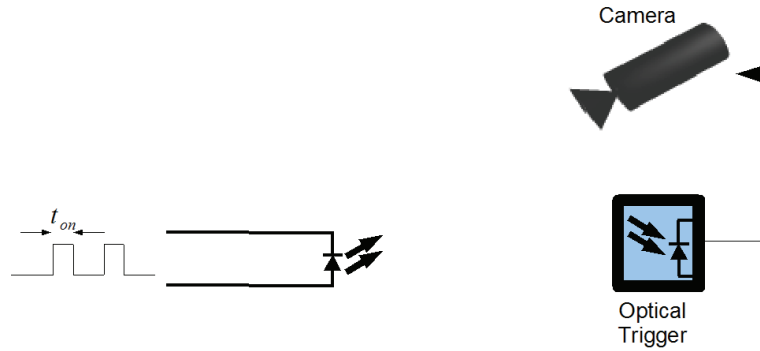


Figure 3.17.: *Setup for measuring the delay between the triggersignal and the first line read-out*

In the moment of extinction or during the low burning phase of the impulse arc, the least appearing brightness difference and consequently contrast ratio is available in the scene. By triggering the camera and LEDs on this low contrast phase, this moment can be used to acquire an image with less hard mapping boundaries for the used camera. If done so, this ratio can be minimized twice: Firstly by the active lighting and secondly by the right camera trigger.

The camera readout-time depends on the pixel resolution selected on the chip. For a single pixel using a FuGa1000 chip driven with 25 MHz the readout time of 40 ns is needed. So the readout time for a single image with a resolution of 300x400 Pixel is accumulated to 4.8ms. This read-out does not include the transfer from the camera chip via the ethernet stack to the computer. The bottleneck here is the ethernet interface with its upper limit of 100 MBit

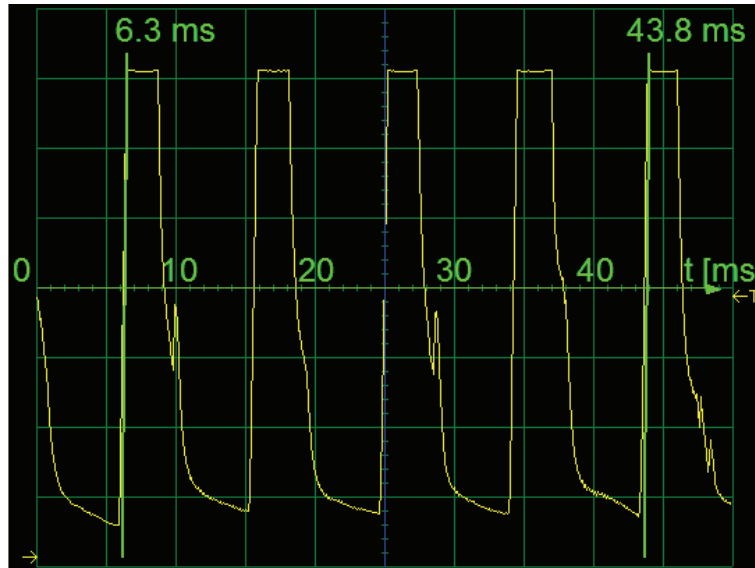


Figure 3.18.: *Qualitative waveform of arc light intensity at pulsed MAG process with 120A, mild steel and a massive electrode with 1.2mm diameter*

physically. It results for an image size of 300 by 400 pixel using an 8 Bit grey value and a maximum frame rate of 90,8 fps, in a transfer rate of 83,13 MBit/s. The pulse frequency of a standard pulse MAG is in between 20-200 Hz which corresponds to a cycle duration of 50-5 ms. A standard application uses a 120 A pulsed MAG process on mild steel with a massive wire electrode with a diameter of $\emptyset = 1,2$ mm. Using a EWM Phoenix welding source the resulting arc is pulsed in a frequency of 106 Hz. The peak time is around 3 ms, while the idle period is a smooth falling edge with a corresponding light intensity changes (see figure 3.18). Based on this knowledge, it can be seen that a precise trigger of the camera to achieve images without a white stripe is hardly available, especially for higher resolutions than 300 x 400 pixels.

3.1.4. Toggle Merging for High Dynamic Range Increase

Toggle Merging means the alternating acquisition and merging of two images acquired by two different camera configurations [62]. Converting the pixel voltages on the camera chip to a digital image, an Analogue to Digital (A/D) converter is used. The A/D-converter used in the Falldorf Fuga1000 camera covers a specific voltage range of only 0 – 2 V.

Merging several shots using a CCD camera needs the inverse response function of the acquisition process. The shutter time or the aperture is the information which is used to calculate the extended information for the radiance map, delivered by several images. In case of a high dynamic C-MOS video camera a shutter time does not exist as the pixels react instantly to changing lighting conditions. It is more the problem of exploiting the conversion process from radiance to a digital pixel value. The available data domain of the used Analog/Digital (A/D) converter bounds the value representation for the acquired image. If an 8 Bit A/D

converter is used, the huge contrast ratio of $1 : 10^6$ is mapped to only $2^8 = 256$ grey levels for the pixel value.

Between the light sensitive pixel and the A/D converter an offset control and amplifier adjusts the output of the pixel to the input range of the A/D converter (see figure 3.2).

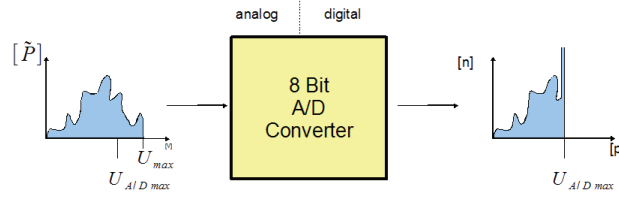


Figure 3.19.: Histogram clipping by saturation of A/D converter

If the highest voltages delivered by the brightest pixels exceed the upper input range of the A/D-converter ($U_{A/D_{max}}$), then these values saturate the digital output to its maximum value. In case of an 8 Bit A/D converter the values are saturated to 255 (see figure 3.19).

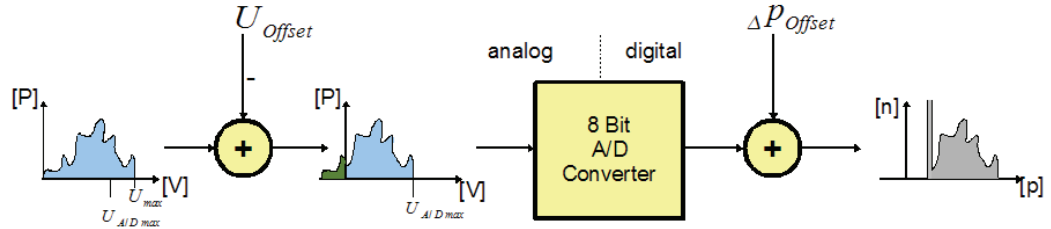


Figure 3.20.: Histogram clipping for dark pixels

In order to cover the complete range of voltages delivered by the pixels, a gain factor and offset can be chosen in order not to exceed the limits of the A/D converter. In this case the scenery will be mostly mapped to much less than 256 grey values.

To increase the amount of available pixel range for maximising the available information in the image, is the idea to compose an image by merging two acquisitions. The first measurement covers the low voltages while saturating the upper pixel voltages. The second measurement with an offset subtraction converts the higher voltages while too low values are clipped to zero. In order to distinguish the pixel values from the first measurement to the second measurement the formerly subtracted voltage has to be re-added as a digital offset (see figure 3.20).

By comparing the two measurements it can be clearly seen, that parts of the image information are complementary, so that the fusion of both image result in an image with more information. The information exceeds the maximum of 255 because the negative offset was re-added. Optimally the ranges of these two measurements do not overlap but are directly neighboured. But if overlapping exists these mid-range areas with data from both images are fused by taking the mean i.e. average of both measurements I_1 and I_2 (see figure 3.21). The resulting image is calculated:

$$I'(u, v) = \begin{cases} I_2 & \text{if } I_1(u, v) = 255 \\ I_1 + \delta p_{Offset} & \text{if } I_2(u, v) = 0 \\ \frac{I_1 + I_2}{2} & \text{else} \end{cases} \quad (3.3)$$

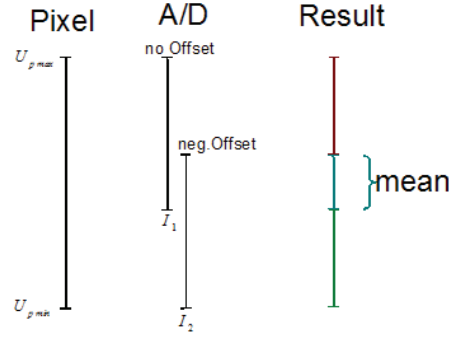


Figure 3.21.: Image merging of two images I_1 and I_2 mapping two different ranges of values

$$\text{with } \delta p_{Offset} = U_{Offset} \frac{2^n}{U_{A/D_{max}} - U_{A/D_{min}}} \quad (3.4)$$

$$\text{and } n : \text{number of bits for A/D converter} \quad (3.5)$$



Figure 3.22.: Underexposed image

The acquisition of images is done with the camera at a resolution of 450 x 600 pixels. The frames per second (fps) rate depends on the optical synchronization and thereby on the welding process. An example for an under- and overexposed pair of images will be used to exemplarily show the functionality of the algorithm. In the underexposed image, which contains the information of the high radiance areas a huge part of the background environment is clipped to black and no information is available there. The glaring areas like the welding arc contain distinctive image information within several grey levels (see figure 3.22).

The overexposed image contains explicit information about the environment, while the glaring areas are saturated to pure white with 255 as pixel value (see Figure 3.23) Using equation



Figure 3.23.: *Overexposed image*

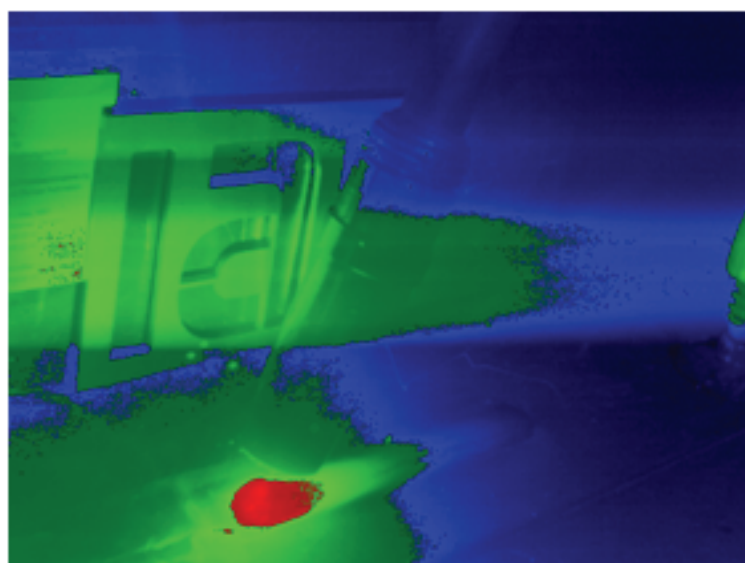


Figure 3.24.: *Composition from high (red), mid (green) and low (blue) radiance information from images in figure 3.22 and figure 3.23*

3.3 the information from these images can be divided into low, mid and high range pixels (see figure 3.24).

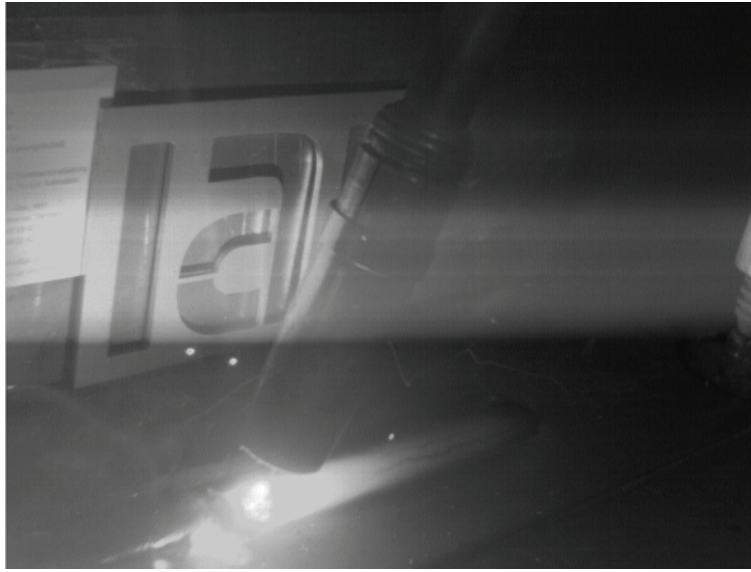


Figure 3.25.: *Resulting image by merging images in figure 3.22 and figure 3.23*

The composition may result in a grey level image with maximumly 512 levels. The introduced example covers a range of 351 different grey levels. It results in an image where the environment and the welding process are visible at once (see figure 3.25). The high amount of grey levels can neither be used for the direct view on a monitor device with the ability of only 256 grey levels, nor can the human eye distinguish such a high amount [14], [63]. In order to segregate more clearly the available information, a pseudo-color image is calculated (see figure 3.26). For showing this image in grey levels on a screen, a histogram compression is done by linear mapping the minimum and maximum value to zero and 255 grey value and linear redistribute the original values between these two bounds.

The pseudo-color image shows distinguishably the full amount of the existent 351 grey levels. It can be seen that the information at the welding pool makes the arc and the pool with its temperature gradient visible. This step beyond the technical and human abilities does not impair the ability of using the data for image processing, segmentation and information extraction, where more than the number of perceptible grey value can be processed.

3.2. Image Enhancement

After acquiring the image by hardware the raw image data has to be processed in order to achieve the maximum information from the images. Existing global as well as local enhancement techniques are described and evaluated regarding welding observation. Also a new local shape based algorithm is presented to be content independent and by that robust

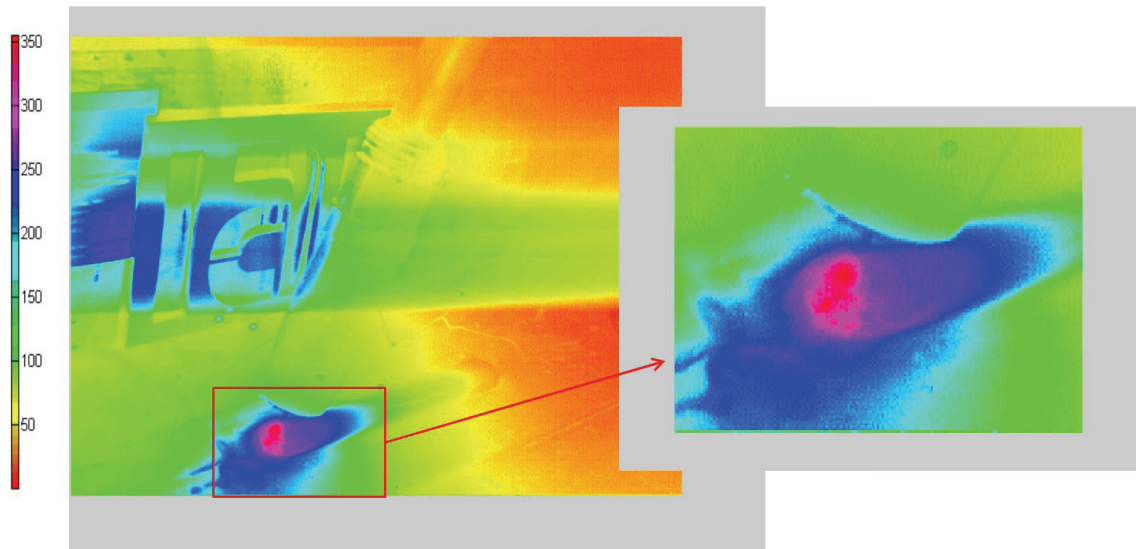


Figure 3.26.: *Pseudocolour image with 351 grey levels corresponding to figure 3.25*

regarding the image content. The algorithm first divides the image into segments, which are independently enhanced and afterwards re-merged to a complete image with high contrast.

3.2.1. Using Histogram Equalization

The technique of histogram equalization does equalize the histogram to the predefined flat (uniform) distribution. It assumes to have either unused pixel values in the image or the mapping is a priori done to an amount of grey values, which is lower than 256. The effect of

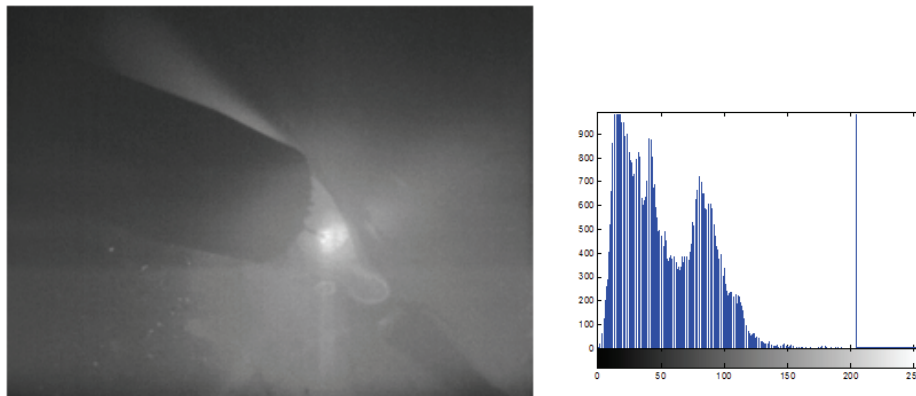


Figure 3.27.: *Original camera image from Figure 3.28.:* *Histogram of the welding scene with torch, arc and seam*
Original image as given in figure 3.27

the histogram equalization is that bins of the original image histogram with an high amount of pixels occupy a wider range in the resulting image histogram than bins with a low amount

of pixels. This reciprocally proportional distribution does depend on the amount of free unused grey values and number of bins in the destination image histogram [14].

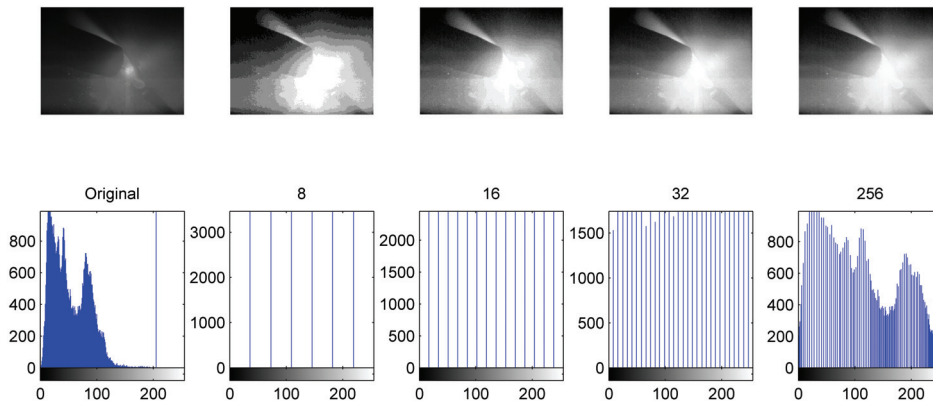


Figure 3.29.: (top) Resulting grey level images of Histogram Equalization for 8, 16, 32 and 256 different resulting bins. (bottom) Corresponding histograms

An example of the histogram equalization applied to the original image in figure 3.27 is given in figure 3.29 for 8, 16, 32 and 256 bins in the resulting image histogram.

It can be seen that the higher the number of destination bins is, the more similar is the qualitative shape of the resulting histogram related to the original image. Also it can be seen that the higher the amount of pixels in a bin is, the wider is the distance to the neighbored bin. It is the basic assumption of histogram equalization that bins with an high amount of pixels contain an high amount of information. For welding the special problem occurs, that the high specific information of the welding arc is contained in bins with small amounts of pixels. These very bright bins are mostly automatically merged to one bin and their assigned width in the histogram is narrow in contrast to the huge background pixel which are not merged and mapped to a wider bin. Hence, the global histogram equalization is not useful for image enhancement related to welding observation.

3.2.2. Using Grey Level Grouping

Grey-Level Grouping (GLG) tries to overcome the drawback of classical global histogram equalization by realigning the used histogram bins to the available number of grey values. It does not change the interregional information in the sense of smaller and larger grey values of two pixels in the entire image. The basic GLG techniques enumerates the used grey values into bins or so called groups. One after another, it merges the bin with the smallest amount of pixels with its smallest direct neighbour. The borders of the groups are updated and the number of groups are equally distributed by assigning each group a constant division of the entire grey scale. If a group was composed by merging different grey levels, then these grey levels are un-grouped and equally distributed over the available division. The resulting

contrast is measured after applying the mapping function received of the un-grouping step. The contrast measure function is related to the average grey value distance the histogram bin to the remaining bin in the image. The step of grouping, mapping and measurement is repeated until only two groups remain. At the end, the specific mapping function is selected which effects the highest contrast measured in the intermediate steps.

After the informal overview, the algorithm is introduced here more elaborated as described in [44]. A basic example describes its functionality starting with figure 3.30 :
Let $H_n(k)$ denote the histogram of the original image, with k representing the grey levels. The set of grey levels found in the image is in the interval $[0, M - 1]$. The n nonzero histogram components are assigned to enumerated bins / groups.

$$G_n(i) = H_n(k) \left| \begin{array}{l} \text{for } H_n(k) \neq 0 \\ k = 0, 1, 2, 3, \dots, M - 1 \\ i = 1, 2, 3, \dots, n \end{array} \right. \quad (3.6)$$

In the case of grey level images $M = 256$ and the number n of groups depends on the number of non-zero histogram bins and by that $n \leq 256$.

At the beginning of the GLG procedure the left and right limits are noted accordingly

$$L_n(i) = R_n(i) = k \left| \begin{array}{l} \text{for } H_n(k) \neq 0 \\ k = 0, 1, 2, 3, \dots, M - 1 \\ i = 1, 2, 3, \dots, n \end{array} \right. \quad (3.7)$$

Now, the first occurring group with the smallest number of pixels is selected and merged with the smaller of its two adjacent neighbours. The group index is:

$$i_a : a = \min G_n(i) \text{ with } i = 1, 2, 3, \dots, n \quad (3.8)$$

and b is the smaller amount of pixels of the adjacent neighbour:

$$b := \min \{G_n(i_a - 1), G_n(i_a + 1)\} \quad (3.9)$$

The index of the merged groups is constituted by:

$$i' = \begin{cases} i_a - 1, & \text{for } G_n(i_a - 1) \leq G_n(i_a + 1) \\ i_a, & \text{otherwise} \end{cases} \quad (3.10)$$

Based on these two selections, the re-grouping for the number of pixels in the bins is made as follow:

$$G_{n-1} = \left\{ \begin{array}{ll} G_n(i) & \text{for } i < i' \\ a + b & \text{for } i = i' \\ G_n(i + 1) & \text{for } i > i' \end{array} \right\} i = 1, 2, 3, \dots, n - 1 \quad (3.11)$$

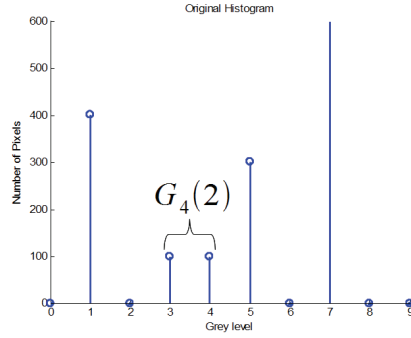


Figure 3.30.: Histogram example for the grouping and ungrouping process

The respective group related limits are updated by:

$$L_{n-1} = \begin{cases} L_n(i) & \text{for } i \leq i' \\ L_n(i+1) & \text{for } i > i' \end{cases} \quad i = 1, 2, 3, \dots, n-1 \quad (3.12)$$

$$R_{n-1} = \begin{cases} R_n(i) & \text{for } i < i' \\ R_n(i+1) & \text{for } i \geq i' \end{cases} \quad i = 1, 2, 3, \dots, n-1 \quad (3.13)$$

An example histogram with 5 initial groups is given in figure 3.30. Group $G_5(2)$ is merged with $G_5(3)$ and results in the successive step to group $G_4(2)$. The updated border to L_4 and R_4 is shown in table 3.2

Group	$G_5(1)$	$G_5(2)$	$G_5(3)$	$G_5(4)$	$G_5(5)$
Number of pixels	400	100	100	300	600
Left border, L_5	1	3	4	5	7
Right border, R_5	1	3	4	5	7
<i>New grouping</i>					
Group	$G_4(1)$	$G_4(2)$	$G_4(3)$	$G_4(4)$	
Number of pixels	400	200	300	600	
Left borders, L_4	1	3	5	7	
Right border R_4	1	4	5	7	

Table 3.2.: Groups and borders of the example given in figure 3.30

Next, the calculation of the contrast is performed. For that the consolidated bins are ungrouped by linearly redistributing the grey levels within the average section available for a bin. The resulting transformation function $T_{n-1}(k)$ will be applied to the image and the resulting contrast is measured. Every bin will occupy an average number of N_{n-1} grey levels as the proportion of the available number of grey values divided by the number of used bins.

$$N_{n-1} = \frac{M-1}{n-1} \quad (3.14)$$

The background, which is the first bin of the lowest grey level, may occupy many grey level although only one grey level is assigned to it $L_{n-1}(1) = R_{n-1}(1)$. In that case to prevent

this occupation the first bin is mapped to 0 and an heuristic alignment is introduced for N_{n-1} :

$$N_{n-1} = \frac{M-1}{n-1-\alpha} \mid \text{with } \alpha \approx 0.8 \quad (3.15)$$

The first group of the example fulfills the condition of identical values of the left and right border. So the α will be considered in the calculation of the ungrouping and mapping for the greyscale transformation.

While constructing the transformation function $T_{n-1}(k)$ four different cases have to be considered:

1. The grey level k falls inside a grey level bin $G_{n-1}(i)$ which is attached to more than one grey level with $L_{n-1}(1) \neq R_{n-1}(1)$. So the grey level k as a part of the bin is linearly re-mapped to the section assigned to the bin using the equation 3.16. This equation is split into the two cases of a monovalued background bin and the general case as introduced:

$$T_{n-1}(k) = \begin{cases} \left(i - \alpha - \frac{R_{n-1}(i)-k}{R_{n-1}(i)-L_{n-1}(i)}\right) N_{n-1} + 1, & \text{for } L_{n-1}(1) = R_{n-1}(1) \\ \left(i - \frac{R_{n-1}(i)-k}{R_{n-1}(i)-L_{n-1}(i)}\right) N_{n-1} + 1, & \text{for } L_{n-1}(1) \neq R_{n-1}(1) \end{cases} \quad (3.16)$$

If the bin occupies only one grey value then the transformation differentiate between a background group o and others

$$T_{n-1}(k) = \begin{cases} (i - \alpha) N_{n-1}, & \text{for } L_{n-1}(1) = R_{n-1}(1) \\ iN_{n-1}, & \text{for } L_{n-1}(1) \neq R_{n-1}(1) \text{ with } i > 1 \end{cases} \quad (3.17)$$

2. If the grey level k falls between two grey level bins $G_{n-1}(i)$ and $G_{n-1}(i+1)$, so that this grey level is not used in the image, then for the sake of completeness, its transformation function is identical to equation 3.17. This ensures that $T_{n-1}(k)$ is monotonically increasing.
3. The grey level k is below the lowest used grey level bin, then it is mapped to zero

$$\text{If } k \leq L_1(1), \text{ then } T_{n-1}(k) = 0 \quad (3.18)$$

4. The grey level k is above the highest used grey level bin, then it is mapped to the highest grey value:

$$\text{If } k \geq R_{n-1}(1), \text{ then } T_{n-1}(k) = M - 1 \quad (3.19)$$

The resulting grey level transformation for the first and second grouping can be seen in figure 3.31.

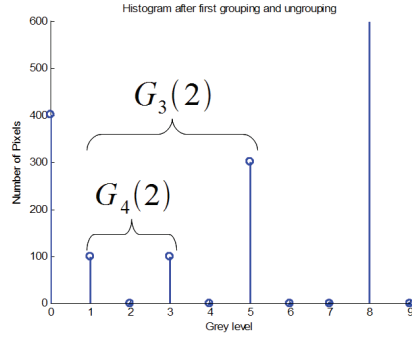


Figure 3.31.: *Histogram after first grouping and ungrouping process*

This constructed grey level transformation $T_{n-1}(k)$ needs to be stored for eventual later use. Its use depends on the resulting contrast which is calculated as the average distance D_{n-1} between pixels on the grey scale for the entire image. The calculation is done by summing up all products of available pairing of bins and weighting these pairing by their grey level distance. If a histogram transformation produces in the final rating of all $H_{n-1}(i)$ the maximum contrast, then this transformation will be selected as the final to achieve the best result:

$$D_{n-1} = \frac{1}{N_{pix}(N_{pix} - 1)} \sum_{i=0}^{M-2} \sum_{j=i+1}^{M-1} H_{n-1}(i) H_{n-1}(j) (j - i) \quad (3.20)$$

$$; \text{for } i, j \in [0, M - 1] \quad (3.21)$$

where N_{pix} is the total number of pixels in the image.

Now the process continues just after the first binning, by searching the bin with the smallest amount of pixels and merge it with its smallest adjacent neighbour. Then ungroup everything by constructing the transformation function T_{n-2} and calculate the contrast D_{n-2} . Continue by binning the residual bins, ungroup, calculate contrast....until only two bins/groups are left. At the end the transformation is selected for the best image transformation with the highest average pixel distance.

In figure 3.32 the result for different selected transformation is given. The original image starts with 206 occurring grey values and by that 206 groups. The contrast measure is shown in figure 3.33. The algorithm starts with the maximum number of groups which is here 206 groups. Then the number of groups is decreased by merging two neighboured groups and the contrast is measured again until a minimum amount of groups is reached As it can be seen the lower bound was set to a minimum of two groups. After merging and contrast measure the grouping and its transformation /mapping function is selected which results in the highest contrast. The example supplies the highest contrast measure for 102 groups.

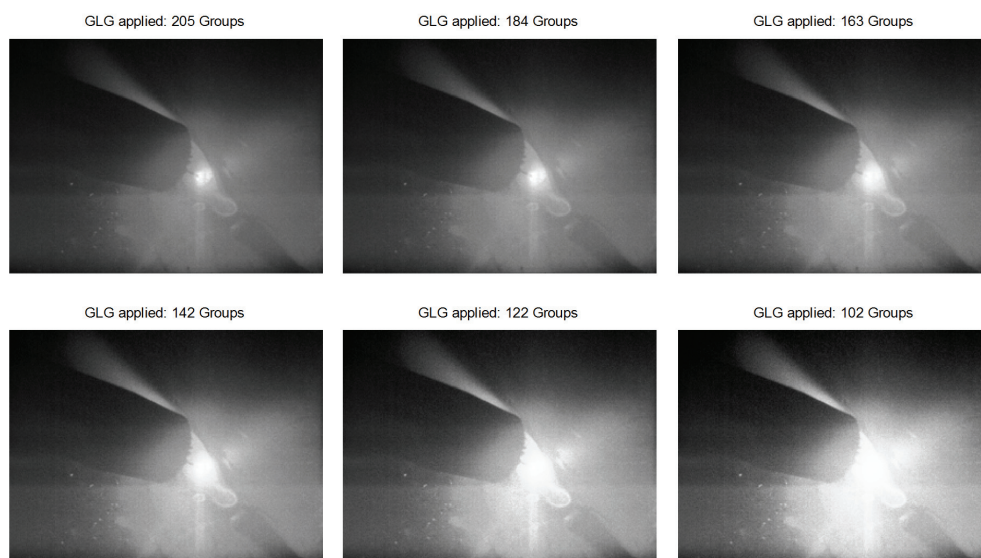


Figure 3.32.: *Mapping for a different amount of selected groups*

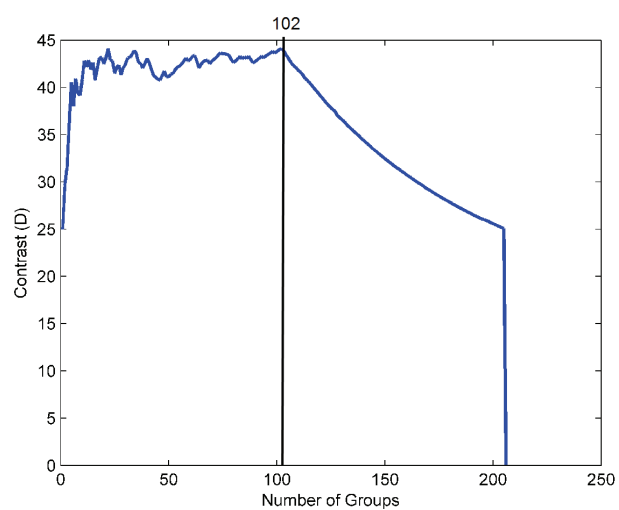


Figure 3.33.: *Contrast measure for different amount of groups*

3.2.3. Using Contrast Limited Histogram Equalization

Digital camera images of the welding scene often suffer of the low available contrast due to the low amount of 256 available grey levels which can be used to present the information of a contrast of $1 : 10^6 / 120$ dB. If the contrast of the image is enhanced globally then the possibilities of enhancement are bounded to a bijective mapping from the original set of grey values to the entire set of 256 grey scales. By improving the contrast locally the bijectivity of the mapping can be lost as two pixels with the identical resulting grey value do not automatically have identical original grey values. For local enhancement a basic approach is to subdivide the image into fixed regions and to enhance them individually. The **Adaptive Histogram Equalization (AHE)** improves the regions by histogram equalization and merges them by a bilinear interpolation of neighboured regions. It weights for a specific pixel the mapping of neighboured region depending on distance of the pixel from the region centres. Plain "coloured" areas will be enhanced, too, so that the information consisting of a single colour plus noise is enhanced to its maximum i.e. the noise will become predominantly visible. The result of AHE of the original image in figure 3.27 is shown in figure 3.34.

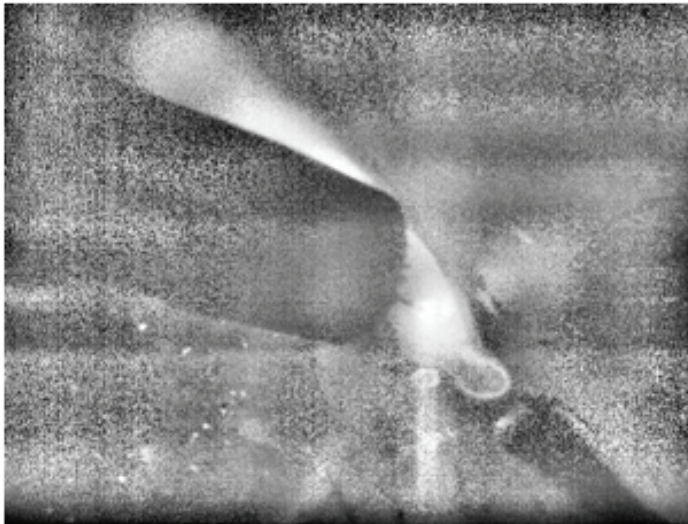


Figure 3.34.: *Camera image processed using AHE approach*

Contrast Limitation By limiting the contrast enhancement as done by the approach of **Contrast Limited Adaptive Histogram Equalization (CLAHE)**, the noise problem of AHE can be reduced [48]. The limitation is done by allowing only a maximum number of pixels in every bin of the local histogram. The pixels which are clipped by that boundary are equally re-distributed over the whole histogram to keep the total histogram count identical. If a small clip limit is selected the re-distribution effects a non-changing 1:1 mapping. The result provides an enhancement based on a priori defined square regions which are enhanced independently. The merging of the independent regions after contrast enhancement is done by a bilinear interpolation of the surrounded regions depending on their grey level mappings.

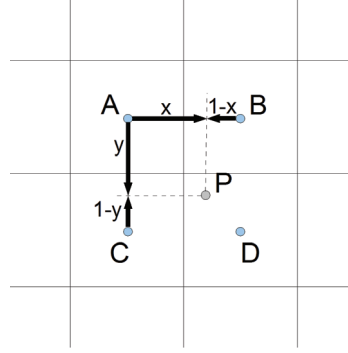


Figure 3.35.: *Bilinear merging of contextual regions A, B, C, D*

Let the grey level mappings of the contextual regions $\{A, B, C, D\}$ be denoted as $g_A(p)$, $g_B(p)$, $g_C(p)$ and $g_D(p)$. Each region has a center point named with the regions letter (see figure 3.35). The distance between two horizontal or vertical neighbored region is normalized to one. The new grey level value p' of the pixel p is calculated by weighted sum of the surrounding mappings. The weighting is done based on the portion of the pixel distance to the center of the contextual regions (see equation 3.22).

$$p'(u, v) = (1 - y) ((1 - x) g_A(p) + x g_B(p)) + y ((1 - x) g_C(p) + x g_D(p)) \quad (3.22)$$

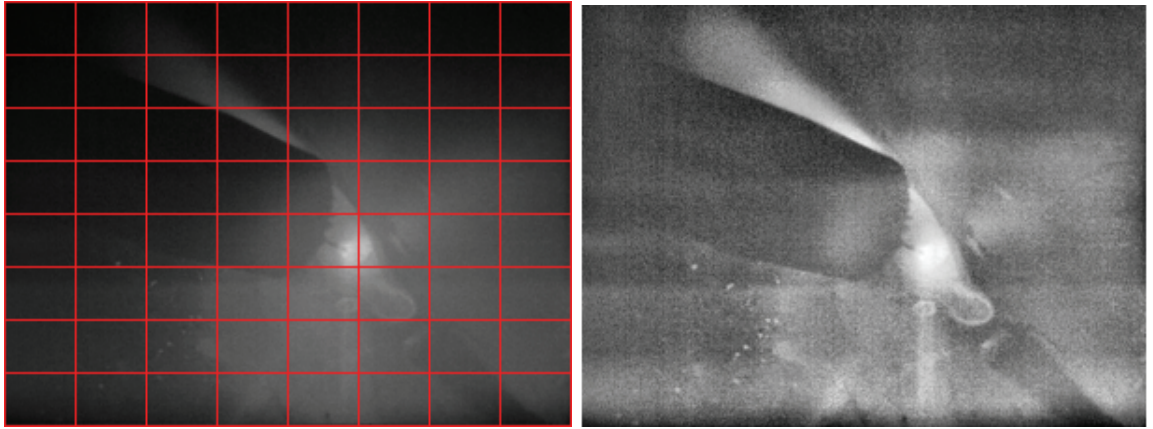


Figure 3.36.: *Camera image with an 8x8 grid of tiles (red lines)* **Figure 3.37.:** *Camera image processed by the CLAHE algorithm*

In figure 3.36 the grid for the squared tiles is sketched with red lines. The grid approach causes artefacts in the resulting image in figure 3.37, where new horizontal and vertical soft lines can be seen in between the tile borders. This algorithm keeps plain areas plain, but improves where image information is available (see figure 3.37). The predefined size and shape of the contextual regions does not consider the content of the image. Hence, it is not robust for different image scenes as the achieved contrast enhancement differs for different object size.

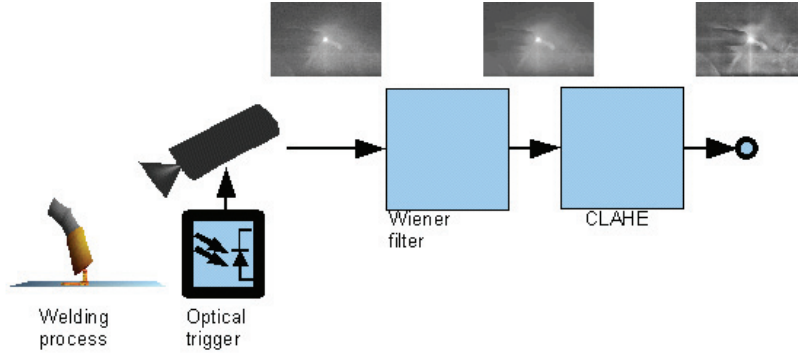


Figure 3.38.: Noise suppression in the image processing queue using a Wiener Filter

Adaptive Wiener Filter Filtering the time relevant Gaussian noise by an optimal filter named by its author Wiener filter, as suggested in [50], can improve the content of a signal by minimizing the noise. This filter can be used in the image processing queue as a preparative step before using the CLAHE algorithm as shown in figure 3.38).

Wiener approached the problem to be a least square minimization problem. Assuming a distortion model of the camera image being the sum of the signal $s(u, v)$ plus additive noise $n(u, v)$:

$$i(u, v) = s(u, v) + n(u, v) \quad (3.23)$$

The Wiener filter can be understood in the frequency domain as a filter $H(\omega_x, \omega_y)$ which restores the image $I(\omega_x, \omega_y)$ to the original data $I'(\omega_u, \omega_v)$ without noise:

$$i(u, v) \circ \bullet I(\omega_u, \omega_v) \quad (3.24)$$

$$I'(\omega_u, \omega_v) = H(\omega_u, \omega_v) I(\omega_u, \omega_v) \quad (3.25)$$

The filter $H(\omega_u, \omega_v)$ can be chosen so that the error function $E[]$ is minimized:

$$\min (E [S(\omega_u, \omega_v) - H(\omega_u, \omega_v) I(\omega_u, \omega_v)]) \quad (3.26)$$

The Wiener filter function for a two dimensional case can be stated using the power spectrum $P_s(\omega_u, \omega_v)$ of the signal representing the image and power spectrum of the noise $P_n(\omega_u, \omega_v)$:

$$H(\omega_u, \omega_v) = \frac{P_s(\omega_u, \omega_v)}{P_s(\omega_u, \omega_v) + P_n(\omega_u, \omega_v)} \quad (3.27)$$

The power spectrum of the image is assumed to be globally constant over the entire image. An improved version applicable to image processing is the Adaptive Wiener Filter, which does not use a fixed filter for the entire image [64], [65]. But here no proper information about the local noise is available, so that the assumption of a constant global noise is used. The power spectrum of the noise P_n is widely assumed as white noise with zero mean $m_n = 0$, so that it simplifies down to the constant of variance $P_n = \sigma_n^2$. If now locally the signal can be modelled by a white noise process $w(u, v)$ independent of the distortion with its own mean $m_s(u, v)$ and variance $\sigma_s(u, v)$, then it can be modelled as:

$$f(u, v) = m_s(u, v) + \sigma_s(u, v) w(u, v) \quad (3.28)$$

The filter function then reduces to :

$$H(\omega_u, \omega_v) = \frac{\sigma_s^2}{\sigma_s^2 + \sigma_n^2} \quad (3.29)$$

or written in the time domain:

$$h(u, v) = \frac{\sigma_s^2}{\sigma_s^2 + \sigma_n^2} \delta(u, v) \quad (3.30)$$

By that the processed pixels can be calculated based on the source pixels $p(u, v)$ by

$$\tilde{s}(u, v) = m_s + (i(u, v) - m_s) * \frac{\sigma_s^2}{\sigma_s^2 + \sigma_n^2} \delta(u, v) \quad (3.31)$$

$$= m_s(u, v) + \frac{\sigma_s^2(u, v)}{\sigma_s^2(u, v) + \sigma_n^2} (p(u, v) - m_s(u, v)) \quad (3.32)$$

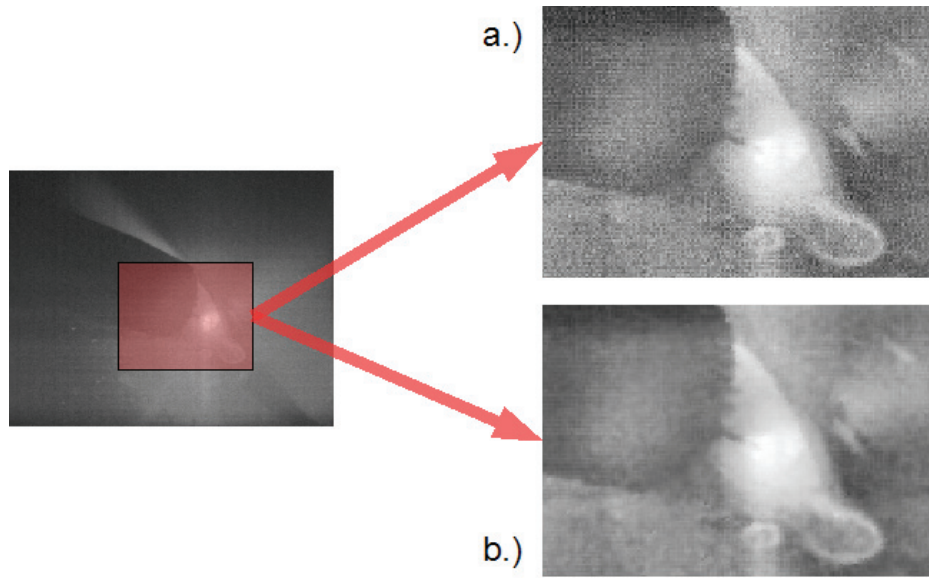


Figure 3.39.: a.) CLAHE without pre-filter, b.) CLAHE with Wiener filter

Applying the Wiener filter does smoothen the image less than applying a classical Gaussian low pass, which is still a small disadvantage. The purpose is to minimize the noise so that the following histogram stretching, inputs only the image information with less noise. The difference between the amplification of noise using the CLAHE with and without pre-filtering with a Wiener filter can be seen in figure 3.39. In figure 3.41 the improvement of the original camera image from figure 3.40 by using the Wiener filter followed by the CLAHE algorithm can be seen.

A technique called unsharp masking, which is the subtraction of a blurred image from the original has been widely used in the publishing industry to sharpen images [14]. The application of this techniques improves the details but produces a degradation by artefacts. The Wiener filter can be used here as a final step to lower the amplified noise. In figure 3.42 a comparison is given where in a.) the unsharp filter is used as the final step and in b.) the Wiener filter.

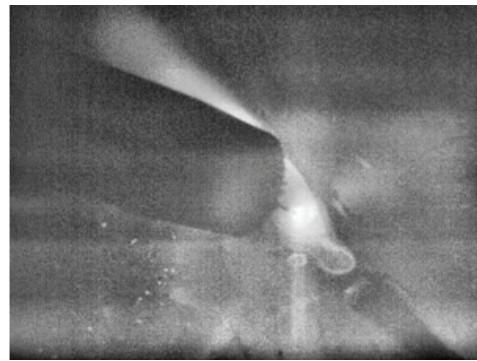
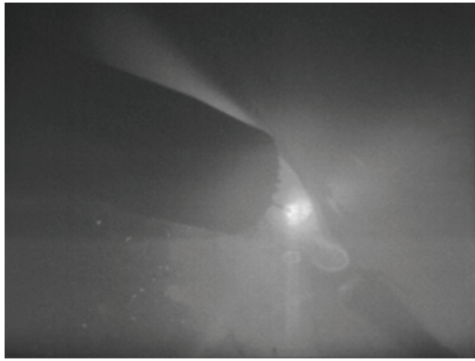


Figure 3.40.: *Original camera image from*

Figure 3.41.: *Improvement by Wiener filtering and processing with CLAHE algorithm*

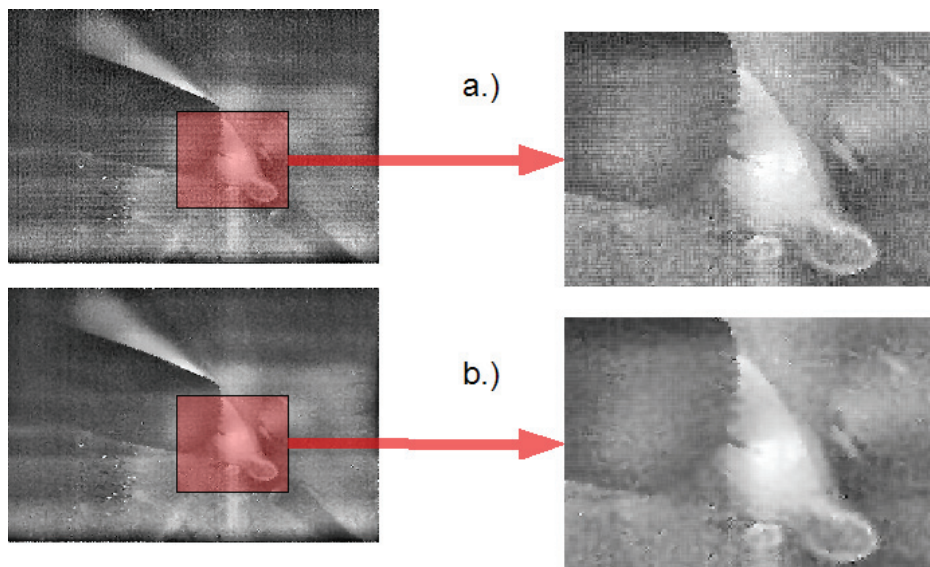


Figure 3.42.: *a.) Filter sequence Wiener → CLAHE → unsharp filter*

b.) Filter sequence Wiener → CLAHE → Wiener filter

3.2.4. Variable Block Shape Adaptive Histogram Equalization

The Variable Block Shape Adaptive Histogram Equalization (VBSAHE) [66] is developed in this thesis as an improvement of the classical CLAHE algorithm. As said, the CLAHE algorithm enhances independently a predefined number of $n \times m$ tiles of a tiled original image, which are consolidated by an interpolation process. The area and the shape of the tiles are fixed so that the content of the image does not allow an individual subdivision of the image. By abolishing the fixed size and shape by a concept with segments depending on the content with individual size and shape, the enhancement does not statically depend on the a priori selection of $n \times m$ tiles.

The basic mathematical concept of the VBSAHE is to compute for every pixel an assigned convergence point where the probability density function attains its maximum in a feature space i.e. mode of the probability density function (PDF). The feature space consists of the position and pixel value so that in the case of a grey image, a probability function is calculated for the feature space given by the row, column and grey value of the pixel. The feature space can be clustered into regions by searching the local maxima, where the gradient of the PDF is zero, for the starting position \vec{x}_1 . Now all starting points/ pixels which converge to similar local maxima are clustered together. Clustering the pixels into segments is done by using a flood fill approach where all modes which deviate from an initially set boundary are clustered together with their corresponding pixels. The retrieved segments are individually enhanced and in a succeeding step the re-composition to a complete image is done (see figure 3.43).

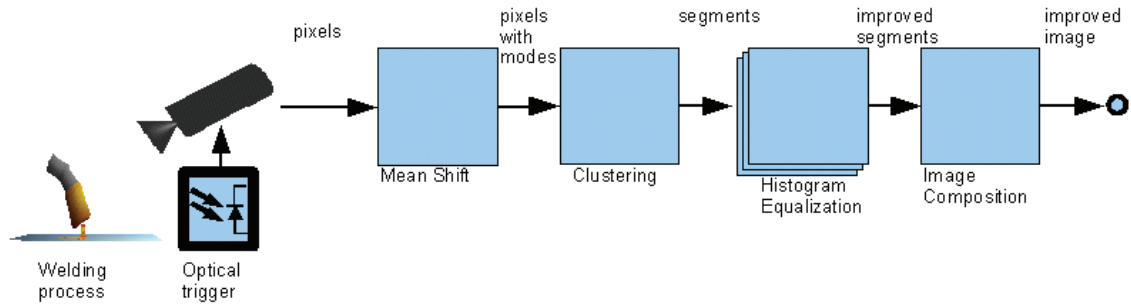


Figure 3.43.: Basic Variable Block Shape Adaptive Histogram Equalization setup

So the Mean Shift algorithm does segment the image based on a statistical approach for a feature space. The Mean Shift states, that it points in the direction of the gradient of the PDF. For the feature space the position and the value of a pixel can be used, whereby the value can be one of the various available colour spaces like greyscale, RGB, HSV, $L^*u^*v^*$ depending on the application. For a deeper understanding the reader is recommended to an introduction to colour spaces and colour image processing as given in [67].

The Mean Shift is defined as the difference with respect to the local mean $E(\cdot)$ regarding the proximity $\{\Delta \vec{X}\}$ at the position \vec{x} [53].

$$m(\vec{x}) = E_{\Delta \vec{X}}(\vec{x}) - \vec{x} \quad (3.33)$$

The question that arises is whether the mean shift vector converges from a starting point to a local maximum. If we regard the feature space to be described by an empirical density function of the represented parameters, then the PDF can be estimated by a kernel density estimation, as well known as Parzen window techniques.

Kernel Density Estimator An image gives n data points \vec{x}_i with $i = 1, \dots, n$ in a d -dimensional feature space R^d . As introduced the dimension of the feature consists of the location (row, column) of the pixel and the used colour space (grey, RGB, HSV etc.). The multivariate density estimator is given by

$$\hat{f}(\vec{x}) = \frac{1}{n} \sum_{i=1}^n K_{\mathbf{H}}(\vec{x} - \vec{x}_i) . \quad (3.34)$$

Where $K_{\mathbf{H}}$ uses a kernel function $K(\Delta\vec{x})$ like the Gaussian or Epanechnikov kernel to weight the input data depending on its difference $\Delta\vec{x} = \vec{x} - \vec{x}_i$.

$$K_{\mathbf{H}}(\Delta\vec{x}) = |\mathbf{H}|^{-1/2} K(\mathbf{H}^{-1/2} \Delta\vec{x}) \quad (3.35)$$

While \mathbf{H} is a symmetric positive definite $d \times d$ bandwidth matrix. The scalar result of equation 3.34 gives the probability density at the point \vec{x} of the feature space. The number of n data points may include all available data as given by an entire image but the kernel truncates to points in the proximity $\Delta\vec{x}$ of \vec{x} . The weighting of the dimensions and their interaction for the density estimation is configured by the bandwidth matrix \mathbf{H} . It scales the input data so that by up- or down scaling of the input data a smaller or wider region is covered by the kernel function $K(\cdot)$. This matrix \mathbf{H} can be simplified by choosing as a constant diagonal matrix with the bandwidth factor h . This simplification does equally weight the dimensions of the feature space:

$$\mathbf{H} = h^2 \mathbf{I} \mid \text{where } \mathbf{I} \text{ is the identity matrix} \quad (3.36)$$

$$= \begin{bmatrix} h^2 & & & \\ & h^2 & & \mathbf{0} \\ & & h^2 & \\ & \mathbf{0} & & \ddots \\ & & & & h^2 \end{bmatrix} \quad (3.37)$$

$$= \text{diag}(h^2) \quad (3.38)$$

The d -variate symmetric kernel $K(\Delta\vec{x})$ is a bounded function which integrates to $\vec{1}$:

$$\int_{R^d} K(\Delta\vec{x}) d\Delta\vec{x} = \vec{1} \quad (3.39)$$

is symmetrical with every positive value being compensated by its negative counterpart:

$$\int_{R^d} \Delta\vec{x} K(\Delta\vec{x}) d\Delta\vec{x} = \vec{0} \quad (3.40)$$

and has finite support by infinite values multiplied with the kernel value result to zero:

$$\lim_{\Delta\vec{x} \rightarrow \infty} \|\Delta\vec{x}\| K(\Delta\vec{x}) = 0 \quad (3.41)$$

Using the density estimator given by equation 3.34 with the simplified bandwidth matrix \mathbf{H} from equation 3.36 leads to:

$$\hat{f}(\vec{x}) = \frac{1}{nh^d} \sum_{i=1}^n K\left(\frac{\vec{x} - \vec{x}_i}{h}\right) \quad (3.42)$$

Which gives the result of the kernel density estimator at the position \vec{x} using the entire data (of the image) by \vec{x}_i .

For image processing, a radial symmetric kernel is mostly produced by using a profile function $k(r^2)$ with $r \geq 0$ as the euclidian distance $r = \|\Delta\vec{x}\|$ from the origin. A normalization constant c_k multiplied with $k(r^2)$ norms the integration of the function to one as demanded by the boundary conditions of equation 3.39 - 3.41.

$$K(\Delta\vec{x}) = c_k k(\|\Delta\vec{x}\|^2) \quad (3.43)$$

As a profile the Epanechnikov profile is often used for the kernel density estimation, as it optimizes the mean integrated squared error [MISE] for the density estimation. This optimal criteria is calculated as the expectation value $E()$ for the difference between the probability density f and the estimated density \hat{f} .

$$E(\|\hat{f} - f\|) = E \int (\hat{f}(\vec{x}) - f(\vec{x}))^2 dx \quad (3.44)$$

Fulfilling the MISE optimum criteria give no assumption about the error distribution. It may happen that the error function has a peak at the maximum and by that a huge deviation between the estimated density and real value may occur at that point. This issue is not investigated in the research community up to now.

The Epanechnikov profile which minimizes the preceeding equation 3.44 is given by

$$k_E(\|\Delta\vec{x}\|^2) = \begin{cases} 1 - \|\Delta\vec{x}\|^2 & 0 \leq \|\Delta\vec{x}\|^2 \leq 1 \\ 0 & \text{else} \end{cases} \quad (3.45)$$

Another advantage of the Epanechnikov profile is its limited expansion and the fact that it does not need to be cut off like a normal (Gaussian) profile with its infinite support. In figure 3.44 the Epanechnikov profile is zero at the border of the kernel, instead of the normal Gaussian kernel in figure 3.45 which is unequal to zero at the border of the kernel matrix (see figure 3.44 - 3.45).

The density estimator in equation 3.42 can be written with the Epanechnikov profile as

$$\hat{f}_{h,K}(\vec{x}) = \frac{c_k}{nh^d} \sum_{i=1}^n k_E\left(\left\|\frac{\vec{x} - \vec{x}_i}{h}\right\|^2\right) \quad (3.46)$$

After setting up the kernel estimation, the next step is to find the gradient of the estimated PDF with the aim to calculate the maxima where the gradient equals zero.

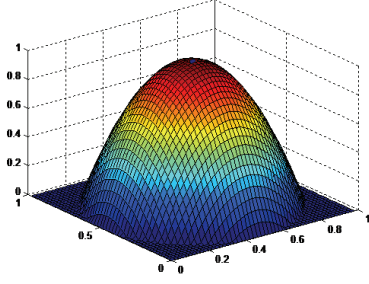


Figure 3.44.: Epanechnikov kernel

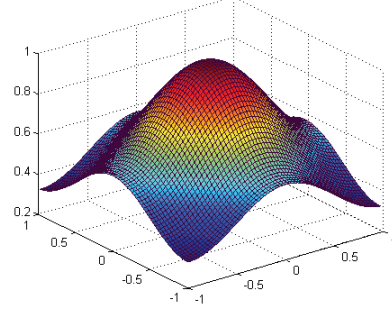


Figure 3.45.: Normal Gaussian kernel

Gradient The gradient of the density kernel estimator of equation 3.46 is

$$\hat{\nabla} f_{h,K}(\vec{x}) = \frac{c_k}{nh^d} \sum_{i=1}^n 2 \left(\frac{\vec{x} - \vec{x}_i}{h^2} \right) k'_E \left(\left\| \frac{\vec{x} - \vec{x}_i}{h} \right\|^2 \right) \quad (3.47)$$

$$= \frac{2c_k}{nh^{d+2}} \sum_{i=1}^n (\vec{x} - \vec{x}_i) k'_E \left(\left\| \frac{\vec{x} - \vec{x}_i}{h} \right\|^2 \right) \quad (3.48)$$

By substituting $g(x) = -k'_E(x)$ in equation 3.48 the gradient can be written as

$$\hat{\nabla} f_{h,K}(\vec{x}) = \frac{2c_k}{nh^{d+2}} \sum_{i=1}^n (\vec{x}_i - \vec{x}) g \left(\left\| \frac{\vec{x} - \vec{x}_i}{h} \right\|^2 \right) \quad (3.49)$$

while expanding equation 3.49 with

$$\sum_{i=1}^n g \left(\left\| \frac{\vec{x} - \vec{x}_i}{h} \right\|^2 \right) \quad (3.50)$$

it comes to:

$$\hat{\nabla} f_{h,K}(\vec{x}) = \frac{2c_k}{nh^{d+2}} \left[\sum_{i=1}^n g \left(\left\| \frac{\vec{x} - \vec{x}_i}{h} \right\|^2 \right) \right] \left[\frac{\sum_{i=1}^n x_i g \left(\left\| \frac{\vec{x} - \vec{x}_i}{h} \right\|^2 \right)}{\sum_{i=1}^n g \left(\left\| \frac{\vec{x} - \vec{x}_i}{h} \right\|^2 \right)} - x \right] \quad (3.51)$$

which results in two terms. The first term is linear related to a probability density, estimated with a different kernel and similar to equation 3.46. The second term gives the mean shift following the equation 3.33 as initially introduced by [68]:

Mean Shift The Mean Shift is established as

$$m_{h,G}(\vec{x}) = \frac{\sum_{i=1}^N \vec{x}_i g \left(\left\| \frac{\vec{x} - \vec{x}_i}{h} \right\|^2 \right)}{\sum_{i=1}^N g \left(\left\| \frac{\vec{x} - \vec{x}_i}{h} \right\|^2 \right)} - \vec{x} \quad (3.52)$$

The Mean Shift uses a kernel profile $g(\vec{x})$. To recall the kernel profile $k_E(x)$ in equation 3.45 results in scalar values as it is a simplification due to the Epanechnikov kernel.

The first term of equation 3.51 can be seen as corresponding to a kernel density estimator $\hat{f}_{h,G}(\vec{x})$. If so, then the kernel

$$G(\vec{x}) = c_g g(\vec{x}) \quad (3.53)$$

needs to fulfil the condition of a bounded symmetrical function with finite supports as stated in equations 3.39.

The proof that the mean shift points in the direction of the local density maximum can be given by reinserting the density estimator $\hat{f}_{h,G}(\vec{x})$ and the mean shift $m_{h,G(\vec{x})}$ in equation 3.51:

$$\hat{\nabla} f_{h,K}(\vec{x}) = \frac{2c_k}{h^2 c_g} \frac{c_g}{n h^d} \sum_{i=1}^n g\left(\left\|\frac{\vec{x} - \vec{x}_i}{h}\right\|^2\right) m_{h,G(\vec{x})} \quad (3.54)$$

$$= \hat{f}_{h,G}(\vec{x}) \frac{2c_k}{h^2 c_g} m_{h,G(\vec{x})} \quad (3.55)$$

$$\mapsto m_{h,G(\vec{x})} = \frac{1}{2} h^2 c \frac{\hat{\nabla} f_{h,K}(\vec{x})}{\hat{f}_{h,G}(\vec{x})} \quad (3.56)$$

It can be seen that the mean shift points in the direction of the density gradient and so in the direction of the maximum increase of the density. The step size is controlled by the PDF in the denominator. Regions with low density are not of interest for the feature space analysis. Nearby local maxima with high densities in the proximity refine the step size of the mean shift and by that the Mean Shift is an adaptive gradient ascent method.

Up to here it is described that the Mean Shift leads from a starting point to the density maximum or so called mode with a zero gradient. If all neighbored starting points which lead to the similar modes are clustered to a segment, then the segmentation of the image is done. A simple floodfill algorithm is used starting at the upper left corner and clustering all connected pixel in the neighbourhood within the colour distance c_d related to the starting pixel \vec{x}_i .

The segments can be defined by

$$S_i = \left\{ \vec{x}_n \in S_l \mid \|\vec{x}_i - \vec{x}_n\| \leq c_d, \vec{x}_i \in R^d \right\} \quad (3.57)$$

In figure 3.47 the mean shift algorithm is applied to the original camera image from figure 3.27. The pixel values of the resulting image show the grey value of the assigned maximum and by that give only one dimension of the 3D feature space consisting of the pixel position u and v plus the grey value. It can be seen that the mean shift algorithm is edge preserving for object larger than the used bandwidth of 16 pixel.

In figure 3.48 a segmentation of figure 3.47 is done using the floodfill algorithm to cluster the pixels. Here it has to be mentioned that the number of segments can be controlled choosing different colour distances. Segments with a minimum number of pixels smaller than 50 are merged to the nearest mode.

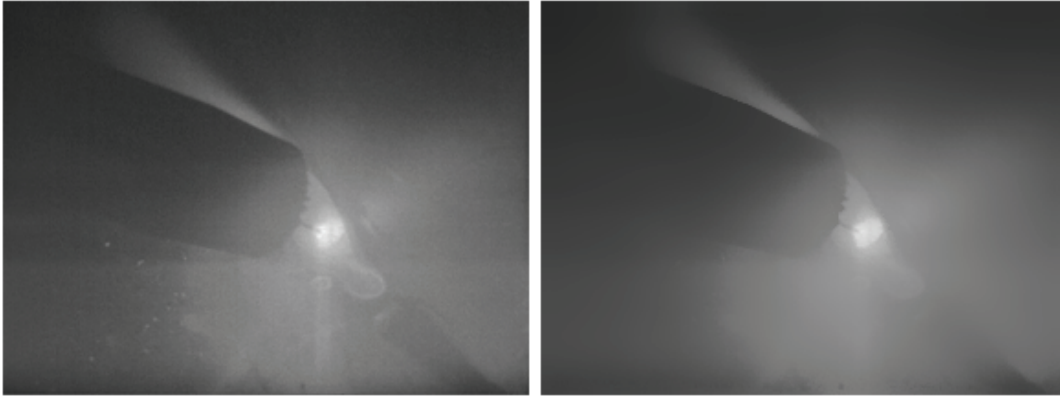


Figure 3.46.: *Original camera image* **Figure 3.47.:** *Mean shift applied to figure 3.46 identical to figure 3.27*

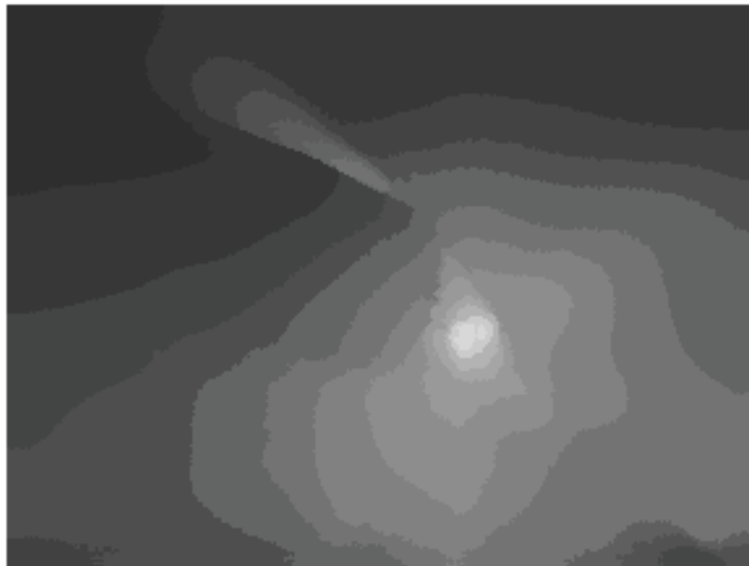


Figure 3.48.: *Floodfill clustering of figure 3.47 with colour distance $c_d = 20$*

The Mean Shift algorithm is computational costly but robust, as it clusters the data based on its statistical occurrence of a multidimensional feature vector and by that is based on the image content.

Enhancing the Segmented Image After segmenting the image using the non-parametric adaptive gradient ascent method Mean Shift, the segments are individually enhanced by a contrast limited histogram equalization as it is used in the CLAHE (section 3.2.3). For every segment with the mode at position \vec{x}_n an individual histogram mapping function $s_{i,\vec{x}_n}()$ is calculated which maps the original pixel value to a new one. The contrast limitation avoids the amplification of noise in flat areas which contain low information, as mentioned in section 3.2.1.

Interpolation After the individual enhancement of the segments, they need to be reunited to a new image. As known from the CLAHE section 3.2.3, an interpolation process is needed to avoid rough edges between the segments. The CLAHE uses an interpolation scheme based on the distance of the pixel to the three nearest neighbored tiles (see figure 3.35). As the tiles are replaced by segments, which are individual in shape and size, this approach will fail. In this thesis it is suggested to use a kernel based approach, where the mapping function for a pixel is a weighted sum of the surrounding histogram mapping functions of segments. The proximity can be weighted by a kernel function such as radial kernels based on the normal (Gaussian) or Epanechnikov profile.

Let the image I consist of a set of positions $X = \{\vec{x} | \vec{x} \in I\}$ and the assigned pixel values $p(\vec{x})$.

After segmentation the image consists of $k \in \mathbb{N}$ segments

$$S = \{S_1, S_2, \dots, S_k\} \quad (3.58)$$

and the set of segments includes all positions of the image $X = \bigcup_{i=1}^k S_i$.

For a pixel value p at position $\vec{x} = (u, v) \in S_i$, $i \in \{1 \dots k\}$, a histogram mapping function $s_i(p)$ is surjectively assigned for this position.

$$\check{p}(u, v) = s_i(p(u, v)) \quad (3.59)$$

so that $s_{i,\vec{x}_n}()$ designates the assigned histogram mapping function at position \vec{x}_n .

To avoid harsh edges due to the segments border a new interpolation approach is used. The new improved and interpolated pixel value $\tilde{p}(u, v)$ for the composed image is calculated by an interpolation of the histogram mapping functions in the kernel bounded proximity $\Delta X(\vec{x}) = \left\{x_m \mid |\vec{x}_m - \vec{x}_n|^2 \leq \epsilon\right\}$.

Analogously to the kernel density estimator a radial kernel (such as Epanechnikov, normal or unit kernel) with its centre at the position \vec{x}_0 (u_0, v_0) is used.

The weighting value at the position \vec{x}_n with the kernel at position \vec{x}_0 is given by

$$K(\vec{x}_0, \vec{x}_n) = c_{k,d} k \left(\left\| \frac{\vec{x}_0 - \vec{x}_n}{h} \right\|^2 \right) \quad (3.60)$$

The new pixel value $\tilde{p}_i(\vec{x}_0)$ is interpolated as a weighted sum depending on the distance and the participating histogram mapping functions s_{i,\vec{x}_n} for the proximity positions \vec{x}_n .

$$\tilde{p}(\vec{x}_0) = \frac{c_{k,d}}{N h^D} \sum_{n=1}^N s_{i,\vec{x}_n} (p(\vec{x}_0)) k \left(\left\| \frac{\vec{x}_0 - \vec{x}_n}{h} \right\|^2 \right) \quad (3.61)$$

The summation in equation 3.61 is influenced only by the limited amount of different histogram mapping functions and the weighting kernel $K(\cdot)$.

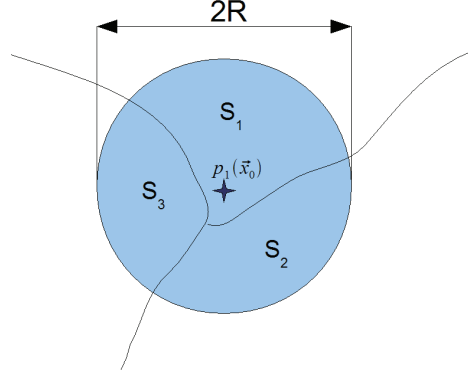


Figure 3.49.: *Interpolating the pixel value by histogram mapping functions of the proximity*

An example is given in figure 3.49 with three participating segments S_1 , S_2 and S_3 . The kernel is a radial kernel with the diameter of $2R$ pixels. The new pixel value for $p(\vec{x}_0)$ is calculated as:

$$\tilde{p}_1(\vec{x}_0) = \frac{c_{k,d}}{3 \cdot 4R^2} \left(\sum_{\forall x_n \in S_1} s_1(p_1(\vec{x}_0)) k \left(\left\| \frac{\vec{x}_0 - \vec{x}_n}{2R} \right\|^2 \right) \right) \quad (3.62)$$

$$+ \sum_{\forall x_n \in S_2} s_2(p_1(\vec{x}_0)) k \left(\left\| \frac{\vec{x}_0 - \vec{x}_n}{2R} \right\|^2 \right) \quad (3.63)$$

$$+ \sum_{\forall x_n \in S_3} s_3(p_1(\vec{x}_0)) k \left(\left\| \frac{\vec{x}_0 - \vec{x}_n}{2R} \right\|^2 \right) \quad (3.64)$$

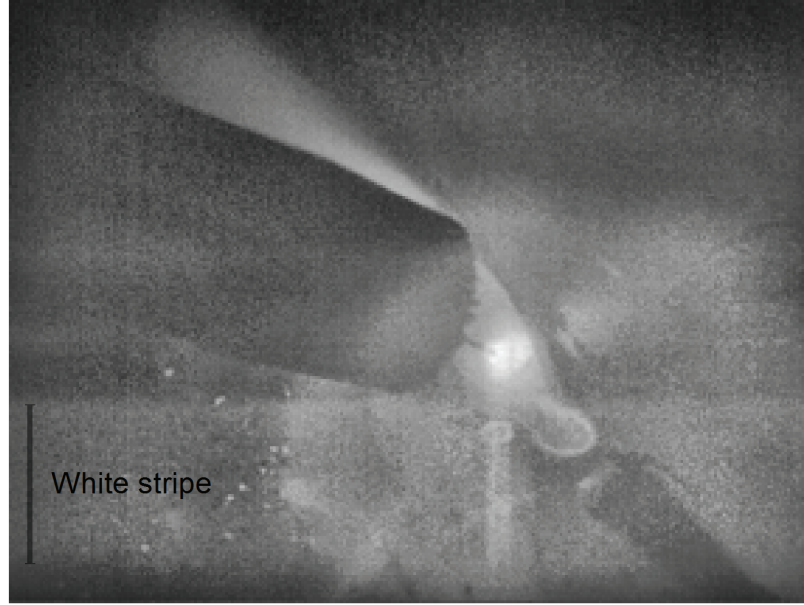


Figure 3.50.: *VBSAHE applied to the original image in figure 3.27*

In figure 3.50 the entire algorithm has been applied to the original image with bandwidth of 16 pixels and an interpolation kernel size of 32.

3.2.5. Stripe denoising

The white stripe in figure 3.50 is a distortion from the welding process. The process highly changes its brightness in time and the camera chip reacts instantly during the line by line readout of the chip. The mean value by row changes, depending on the occurrence of the white stripe which signifies a global illumination change. But if in comparison the mean value by column is taken into account it can be as well seen that in any case the average pixel value depends on the image content, too. In figure 3.51 the green graph gives the average by row in terms of distance from the left border and the red graph gives the mean value per column rising in terms of the distance from the top. Due to the dependency of the average values from the content, these average parameters cannot be taken into account for finding the starting and end point of the white stripe. In every case the content of the image may override the extraction criteria, so that the robustness of this criteria is diminished. An alternative approach is to use morphological operations with its basic functions of opening and closing. The operation called "top-hat" is defined as the subtraction of its opening from the original.

$$I' = I - (I \circ b) \quad (3.65)$$

with \circ being the morphological opening operator and b as the structuring element.

As the white stripe ever occurs horizontal perpendicular to the camera readout direction a structuring element with bar shape and a width equal to the image width gives a boundary for the operation.

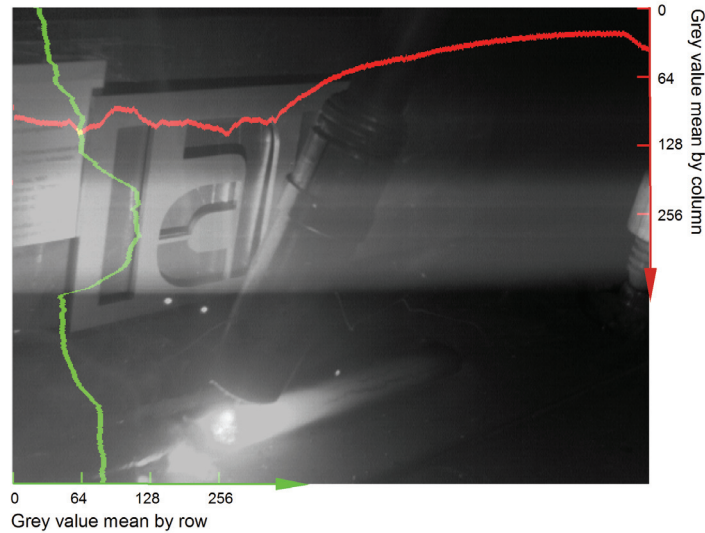


Figure 3.51.: *Mean value by row and column as the distance from left or from the top of the image*

Tests done with different height structuring elements effect in different amount of minimizing the white stripe (see figure 3.52). For a resolution of 600×450 pixel the best result is achieved by using the height of 40 pixel for the structuring element. This filtering can be applied before enhancing any contrast so that the white stripes -meaning distortion- will not be amplified by contrast enhancement algorithms for welding observation.

3.3. Selective Automatic Darkening Filter

The aim of the SADF is to darken the users view where glaring lights occur. A graphical liquide crystal display (GLCD) is mounted in front of the users eyes. Those pixels of the GLCD shall be darkened, which cover the users line of sight to a glaring light. The sensor for such a system needs to extract the 3D position of the glaring light and the transformation from the camera coordinate system to the users view needs to be known. The system consisting of the users eye and the GLCD may be modelled as a second camera system. The plane of the GLCD can be seen as the image plane where the extracted glaring light position is mapped. So if the position of the glaring light on the GLCD is known then the position of the pixel to be darkened is identical.

The GLCD and a camera is integrated in a welding helmet. In figure 3.53 the setup of the system is shown. The GLCD substitutes the Automatic Darkening filter with its single pixel. The electronic for the GLCD is situated in the area nearby the welders chin. The camera is split into two pieces. One is the pure camera chip with the lense and second the interfacing electronic device, which is integrated in a housing under the top shell of the helmet.

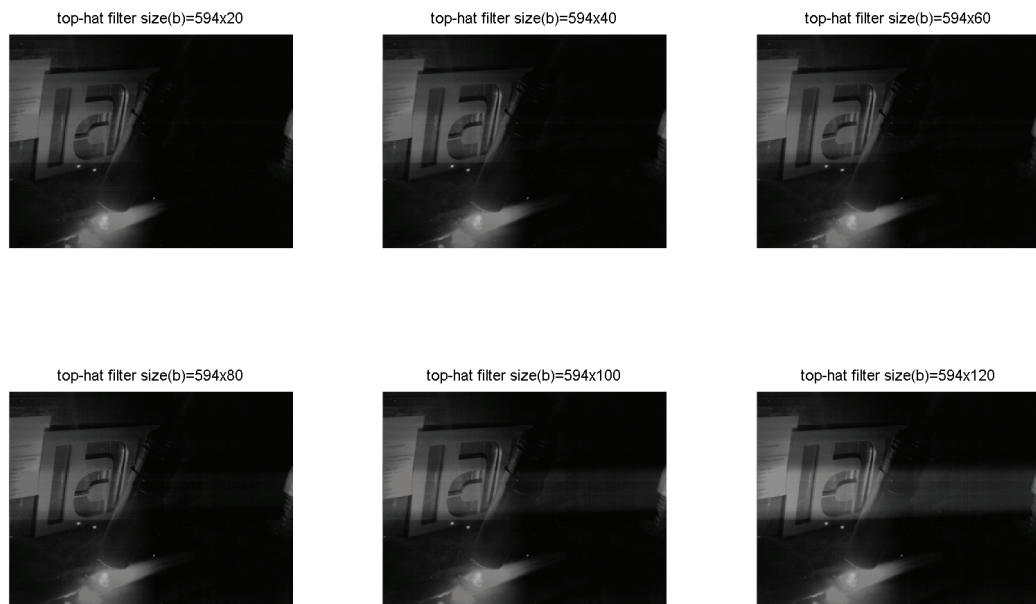


Figure 3.52.: *Minimizing the white stripe using top-hat operator with different structuring elements*

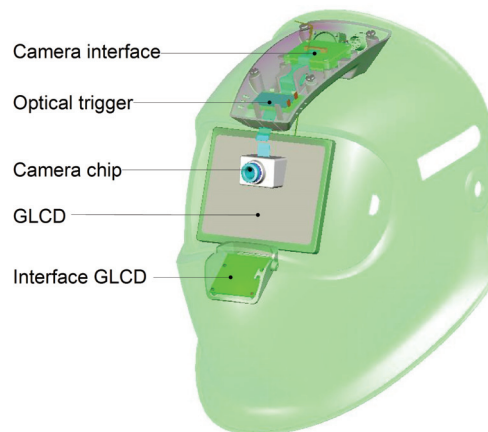


Figure 3.53.: *Prototype setup for the SADF system*

Total Area	8.6 x 8.7 cm^2
Display Area (see-through)	7.55 x 6.80 cm^2
Display Area (renderable)	7.35 x 6.60 cm^2
One Pixel Area	0.05 x 0.05 cm^2
Resolution	147 x 132 <i>pixels</i>
Depth	2 <i>bits</i>

Table 3.3.: *GLCD Specification*

A stereo camera system can extract the 3D position of any object in the environment. Alternatively planar 2D-marker may be used with a monoscopic camera to extract its 3D position. Widely used software for such an extraction is the ARToolkit or the Studierstube framework [69], [70] which use squared print-out markers. Using such a software needs only a proper calibration of the intrinsic camera parameters, which is available with the used marker extraction software or by additional free software.

Extracting the marker position in 3D can be used to calibrate the unknown 3D-transformation between the camera coordinate system and the GLCD system (see figure 3.55). For this a set of corresponding 3D from the camera system to 2D points in the GLCD system is extracted and the data for the calibration.

After computing the 3D-transformation from the camera to the GLCD system the system shall be used further without any artificial marker. It is assumed that the manual welding process is done at a constant working distance so that the z-coordinate is assumed to be known of the welding arc. Deviations from this constant distance assumption cause parallax errors, which will be examined in the following chapter.

For understanding these principles, following [71], short introductions to the camera model and the epipolar geometry are given in the Appendix A.1.

3.3.1. Graphical Liquid Crystal Display

The GLCD used in this new system has a resolution of 132×147 pixel with four grey levels from transparent to maximum shading. The basic dimensions of the device are given in table 3.3.

The single pixels on the GLCD are separated by a small transparent gap. If pixels are darkened then this gap is still open for light transmission. The use of the GLCD is critical for the shading mode in order to protect the welder. So all the boundaries have to be optimized for shading. The scattering light is minimized by permanently darkening this gap with a black matrix (see figure 3.54).



Figure 3.54.: *Black matrix on the GLCD to minimize the scattering light*

Measurement without any controller attached to this GLCD result in a shading equivalent to a protection level of 7.8 which corresponds to 0.0085% transmission. If a controller is used which sets the pixel by alternating through every row and column, then the shading is getting less to a protection level of 4.2 which corresponds to a light transmission rate of 0.8% and a protection level for the transparent mode of 2.6 which corresponds to a light transmission of 29%.

3.3.2. Calibration of a GLCD to the Camera

The system of the GLCD with the user's eye behind form a system similar to a camera. The GLCD form the image plane and together with the eye the lens system and camera center is defined. In figure 3.55 the principal setup of such a system is shown. It consists of a camera system with the optical axis nearby the users optical axis to achieve a similar viewport so that the parallax error is as minimal as possible.

The calibration of the GLCD system to the camera is needed in order to darken the camera extracted glaring light for the user on the GLCD.

The principle is to have the 3D Information of specific points in the camera coordinate system and to retrieve its 2D correspondence on the GLCD [72]. For that the user has to wear the system on his head and to overlay a square or crosshair blended on the GLCD with a predefined point in 3D. The proper overlay is done by head movement of the user. With the correspondences of the 3D marker position and its 2D equivalent on the GLCD, the mapping of 3D points in the camera coordinates to the 2D points on the GLCD can be calculated. The 3D information can be supplied by a stereo-rig or, as it is done here, by using artificial markers [69]. The coordinate system of the 3D data points extracting device needs to be transformed by an euclidian transformation compounded by a rotation and translation.

This transformation will be covered by the calibration and needs to be done for the left and right eye independently. In figure 3.56 the setup with the different coordinate systems is shown.

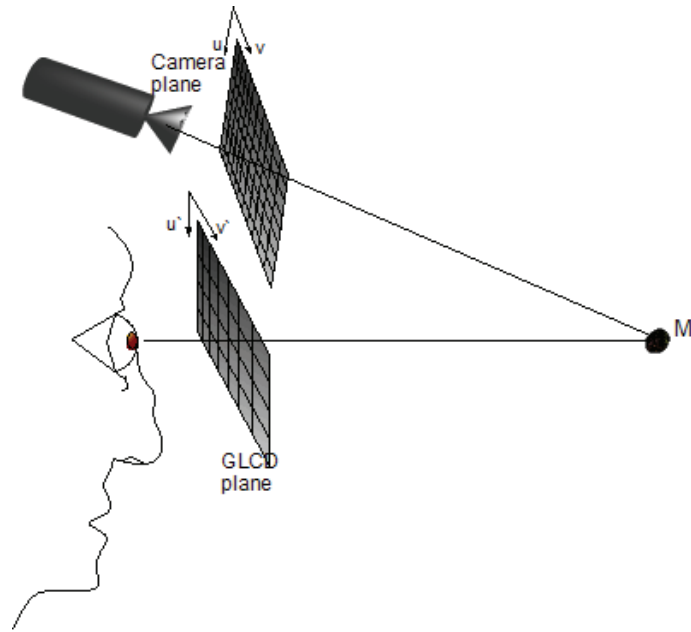


Figure 3.55.: *Camera and LCD Plane for SADP*

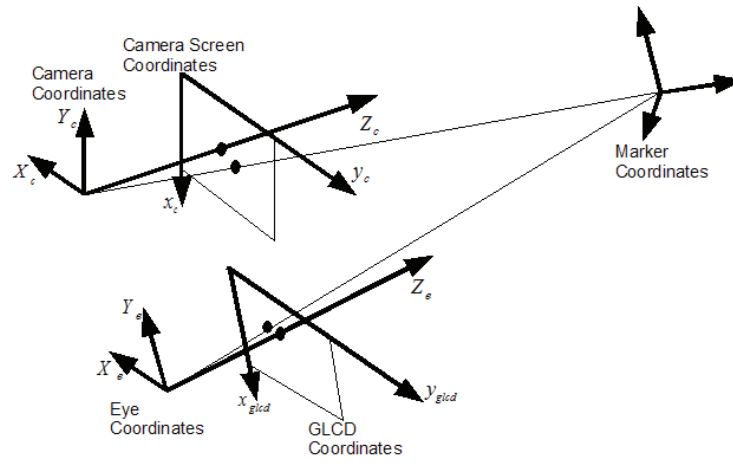


Figure 3.56.: *Coordinate Systems for SADP setup*

The mapping of 3D points which shall be darkened on the GLCD-eye system is done following the model of a camera as introduced in equation A.13 with the GLCD as the image plane. The GLCD may not sense any environmental information. A second camera may be used to form a stereo camera system and by that to measure the 3D position in the camera coordinate system. If now a 3D point from the extracting device shall be mapped to a 2D pixel in the coordinate system of the GLCD, then first this point will be transformed from the device coordinate system to the Eye/GLCD coordinate system using \mathbf{T}_{ec} and secondly this 3D point is mapped to the 2D GLCD image plane using Eye/GLCD camera matrix \mathbf{P}_e :

$$\vec{x}_{glcd} = \mathbf{P}_e \mathbf{T}_{ec} \vec{X}_c \quad (3.66)$$

$$= \begin{bmatrix} \alpha & x_0 \\ & \alpha & y_0 \\ & & 1 \end{bmatrix} \begin{bmatrix} R_{11} & R_{12} & R_{13} & T_x \\ R_{21} & R_{22} & R_{23} & T_y \\ R_{31} & R_{32} & R_{33} & T_z \end{bmatrix} \vec{X}_c \quad (3.67)$$

$$= \mathbf{C}_{ec} \vec{X}_c \quad (3.68)$$

where α , x_0 and y_0 refer to equation A.13 to be the focal length and principal point coordinates.

In order to be able to decompose the unknown matrix \mathbf{C}_{ec} during calibration into the Eye/-GLCD "camera" matrix \mathbf{P}_e and the transformation \mathbf{T}_{ec} an additional scalar k in the camera matrix \mathbf{P}_e is introduced. It can be physically interpreted as the slant between the x and y-axis on the image plane chip i.e. in our case the slant on the GLCD. Normally it will only be unequal to zero due to noise in the measurements. The decomposition of the computed \mathbf{C}_{ec} into the eye projection matrix \mathbf{P}_e and transformation matrix \mathbf{T}_{ec} can be done using RQ-decomposition (see Appendix A.2 and [73]).

$$\mathbf{P}_e = \begin{bmatrix} \alpha & k & x_0 & 0 \\ & \alpha & y_0 & 0 \\ & & 1 & 0 \end{bmatrix} \quad (3.69)$$

The equation 3.67 can be rewritten using homogeneous coordinates:

$$\begin{bmatrix} x_{glcd} \\ y_{glcd} \\ w_{glcd} \end{bmatrix} = \begin{bmatrix} c_{ec}^{1T} \vec{X}_c \\ c_{ec}^{2T} \vec{X}_c \\ c_{ec}^{3T} \vec{X}_c \end{bmatrix} \text{ with } \mathbf{C}_{ec} := \begin{bmatrix} c_{ec}^{1T} \\ c_{ec}^{2T} \\ c_{ec}^{3T} \end{bmatrix} \quad (3.70)$$

$$\vec{0} = \begin{bmatrix} x_{glcd} \\ y_{glcd} \\ w_{glcd} \end{bmatrix} \times \begin{bmatrix} c_{ec}^{1T} \vec{X}_c \\ c_{ec}^{2T} \vec{X}_c \\ c_{ec}^{3T} \vec{X}_c \end{bmatrix} \quad (3.71)$$

where x_{glcd} , y_{glcd} and w_{glcd} form the 2D point on the GLCD in homogeneous coordinates.

By using the skew symmetric matrix (see Appendix A.2) equation 3.71 can be reformulated to be used for the i-th measured 3D-2D correspondence

$$\vec{0} = \begin{bmatrix} 0^T & -w_i X_i^T & y_i X_i^T \\ w_i X_i^T & 0^T & -x_i X_i^T \\ -y_i X_i^T & x_i X_i^T & 0^T \end{bmatrix} \begin{bmatrix} c_{ec}^{1T} \\ c_{ec}^{2T} \\ c_{ec}^{3T} \end{bmatrix} \quad (3.72)$$

The equation 3.72 forms a homogeneous linear system. A solution can be retrieved by stacking the first and second line for the measured n correspondences to a $[2n \times 12]$ matrix. This overdetermined system can be computed by using the singular value decomposition of the stacked matrix, where the unit singular vector \vec{v} corresponding to the smallest singular value supplies the solution for \vec{c}_{ec} .

$$\vec{c}_{ec} = \begin{bmatrix} c_{ec}^{1T} \\ c_{ec}^{2T} \\ c_{ec}^{3T} \end{bmatrix} = \begin{bmatrix} v_1 \\ v_2 \\ \vdots \\ v_{12} \end{bmatrix} \quad (3.73)$$

One problem which occurs while computing numerical solutions is the error of the solution. If the problem is ill-conditioned caused by the input data, the result implies raised errors due to rounding errors. The conditioning of the problem to be solved can be enhanced by normalizing the input data using a scaling and translation to a new centroid with the origin $\vec{0}$ and an average distance to the origin of $\sqrt{2}$. The normalization \mathbf{T}_{3D} for the 3D point and the transformation \mathbf{T}_{2D} for the 2D points are calculated independently. After calculating the solution $\tilde{\mathbf{C}}_{ec}$ for the transformed data, the solution needs to be back transformed to \mathbf{C}_{ec} by:

$$\mathbf{C}_{ec} = \mathbf{T}_{2D}^{T-1} \tilde{\mathbf{C}}_{ec} \mathbf{T}_{3D} \quad (3.74)$$

Although the normalization is introduced at the end of the calibration it is an essential step and must not be considered optional [71].

After introducing the algorithmic part of the calibration the question arises how to implement it into a program and how a user will be prompted during calibration. If points in 3D and the correspondent 2D points on the GLCD are measured then the solution for \mathbf{C}_{ec} can be calculated. The measurement can be done by actively requesting the user to do the following task repeatedly.

- On the GLCD a cross-hair will be shown at a random position and the user has to align his head, and consequently the GLCD and camera, until the cross-hair seen by one eye covers the 3D point / marker.
- At the moment, when the 3D point and the cross-hair are aligned, the user presses a button to save the 3D position of the point and its image in the camera view.
- The covering of the cross-hair with the marker is repeated for several times to receive sufficient correspondences between the camera image and the GLCD.
- The complete procedure is done once for each eye separately

After computing the calibration, the mapping of 3D points onto the GLCD plane is known. This means that in the application during welding the 3D position of the glaring light which is the welding arc respectively, needs to be extracted. The welding arc has not the information like a planar ARToolkit marker has, so that only the pixel position on the camera image plane can be extracted. For simple application and according to that simple welding situations, it is assumed that the working distance between the welders eye and the torch is

3. IntARWeld system

fixed during welding. So that the 2D position can be used to calculate the 3D position under the assumption of the constant working distance i.e. the z-coordinate. For more complex scenarios with changing working distances, a 3D tracking of the welding arc or torch is needed.

4

Results

This chapter presents the evaluation of three different aspects of the SADF system. The first and most important section evaluates the performances of the different image enhancement algorithms as introduced in chapter 3. The global histogram equalization, grey-level-grouping, CLAHE and the new VBSAHE are evaluated for different welding processes. The high dynamic range improvement by merging two different shots of the image is included as well. The merging approach does not cover the subject of contrast enhancement like the preceding algorithms. Its results is presented in relation to the additional extracted amount of data, which covers better the available grey scale space.

Secondly in this chapter the LED lighting is compared with different bright welding arcs for standard welding processes to demonstrate the abilities of this setup. At last, a view is taken onto the SADF idea. Due to the lack of a GLCD, which darkens the arc sufficiently, only one process, the MAG process, is used.

The evaluation of the different image processing algorithms focusses on the GMAW processes with its subtypes of MAG and MIG welding. For these processes a range of three different currents are considered. The result of the VBSAHE algorithm is rated for the different welding current. The comparison of the histogram equalization, the grey-level-grouping (GLG), the CLAHE and the VBSAHE algorithm is done for one common welding current.

In order to evaluate the LED lighting, records are done with the LEDs turned "ON" and "OFF". The image merging technique needs a toggling camera parameter setup for under- and overexposed images. The raw data consist of a video with images of the alternating camera setup. Hence, for each welding current three recordings are made to retrieve the raw data for evaluation: LED on, LED off and the toggle video.

4. Results

To complete the range of welding processes, the image recording results are presented for TIG welding for a specific parameter setup with the LEDs turned off. All applied settings and image enhancement algorithms can be found in table 4.1. For all welding loops a semi-automated test stand is used (see figure 4.1). It consists of a movable table which is steered by the welding machine as it moves only during welding. The scenery has in the background a cut-out **iat**-logo, which moves with the table and a fixed mounted welding torch.

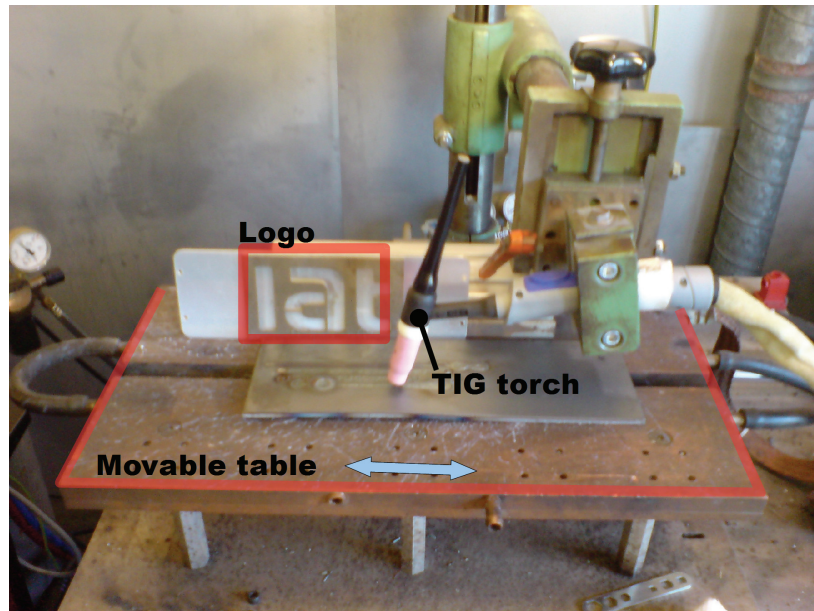


Figure 4.1.: Test-stand for semi-automated welding

4.1. Pulsed MAG process

The raw data for the evaluation is taken from the MAG, MIG and TIG processes. The setup of the application is a work bench for semi-automated welding. The welding torch is here at a fixed position and the position of the work bench is changed constantly by a linear drive. The chosen linear speed for the welding is $88 \frac{cm}{min}$.

4.1.1. Raw Data

The MAG process is used with mild steel and gas consisting of 82 % argon and 18 % carbon dioxide as the active component. The used wire is a low alloy wire electrode with a diameter of 1.2 mm. Following the European Norm EN440 this wire electrode is categorized into the type **G 42 4 M G3 Si1**. The used welding machine is of the type **PHOENIX 521 PULS coldArc** from the company **ewm** (Germany).

Lighting	Process	Current [A]	Algorithm
LED Off	MAG	85	VBSAHE
LED ON	MAG	85	VBSAHE
Toggle	MAG	85	ToggleMerge
LED Off	MAG	120	Histogram equ., GLG, CLAHE, VBSAHE
LED ON	MAG	120	VBSAHE
Toggle	MAG	120	ToggleMerge
LED Off	MAG	220	VBSAHE
LED ON	MAG	220	VBSAHE
Toggle	MAG	220	ToggleMerge
LED Off	MIG	80	VBSAHE
LED ON	MIG	80	VBSAHE
Toggle	MIG	80	ToggleMerge
LED Off	MIG	180	Histogram equ., GLG, CLAHE, VBSAHE
LED ON	MIG	180	VBSAHE
Toggle	MIG	180	ToggleMerge
LED Off	MIG	240	VBSAHE
LED ON	MIG	240	VBSAHE
Toggle	MIG	240	ToggleMerge
LED Off	TIG	230	Histogram equ., GLG, CLAHE, VBSAHE

Table 4.1.: *Series of measurements to evaluate different image enhancement algorithms*

Single images

Different welding currents of 85 A, 120 A and 220 A are selected in order to cover the mid and upper range of occurring brightness conditions. The images taken at 85A differ in the lighting by the LEDs, which are focussed onto the boundary area around the welding arc. It can be seen in figure 4.2 and figure 4.3 that the difference with and without lighting is small. Parts of the metal grid (B), the front edge of the metal plate (A) and the welding torch (C) are lighted by the LEDs. A difference with or without lighting by the LED can be merely seen but will be made visible by the enhancement algorithms.

The brightness of the arc differs over a wide range from $1.5 \cdot 10^3$ Lux for 85 A over $2.4 \cdot 10^3$ Lux at 120 A up to $8.13 \cdot 10^3$ Lux at 220 (see table 4.2). The measurement is done at a distance of 1 m at the height level of the welding torch and can be rated only as a qualitative value as it depends on the physical setup of the work bench, welding torch inclination and distance to the work piece. Differences caused by the LED lighting remain visible for the welding arc with 120 A and 220 A but get less the higher the arc current is (see figure 4.4 - 4.7).

As it can be seen, the white stripes on the images, which are caused by the instant brightness changes in connection with the rolling shutter of the used FuGa1000 camera chip, occur more often in the case of higher currents used. They depend on the pulse frequency of the

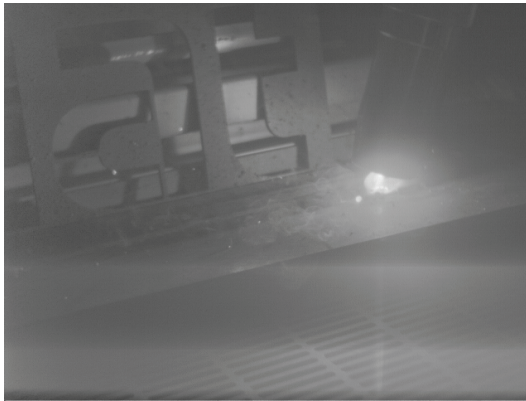


Figure 4.2.: *MAG, 85 A, LED Off*

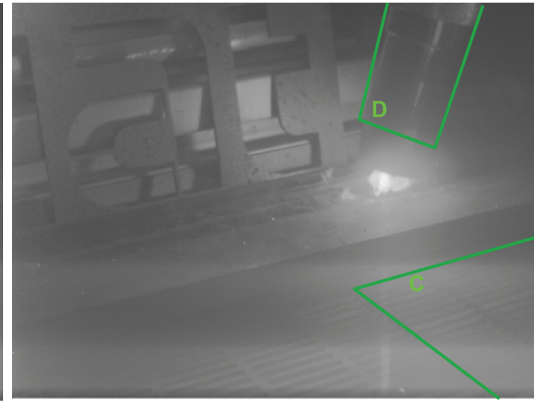


Figure 4.3.: *MAG, 85 A, LED On*

Welding Current [A]	Brightness [lux]
85	$1.5 \cdot 10^3$
120	$2.4 \cdot 10^3$
220	$8.13 \cdot 10^3$

Table 4.2.: *Brightness of pulsed MAG process at 1 m distance from the welding torch*

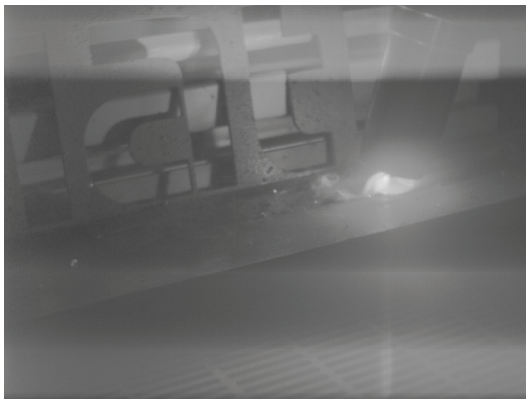


Figure 4.4.: *MAG, 120 A, LED Off*

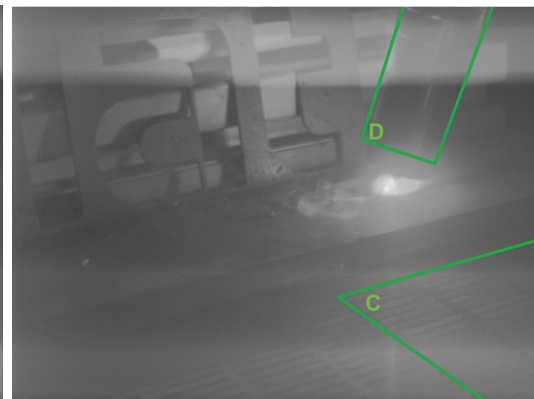


Figure 4.5.: *MAG, 120 A, LED On*

welding arc which is modulated depending on the current. This pulse frequency modulation is changed within the working range capacity of the welding machine.

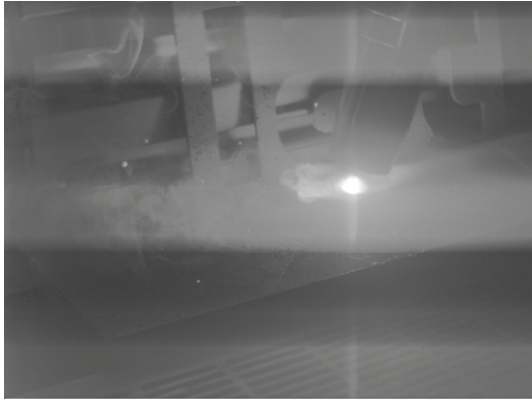


Figure 4.6.: *MAG, 220 A, LED Off*

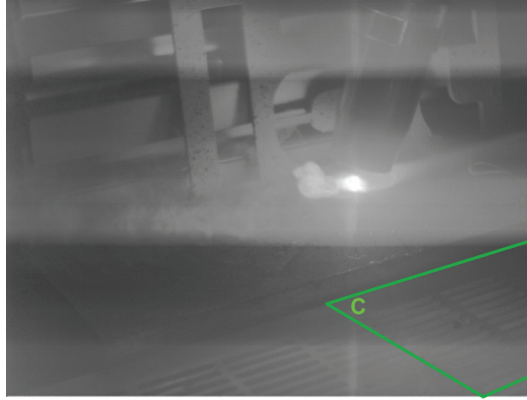


Figure 4.7.: *MAG, 120 A, LED On*

Toggle images

As it was explained in section 3.1.4 the quality expectations for an under- and overexposed image to be merged to obtain a new image differ significantly from those of a single shot. The overexposed image shall contain the darker areas like the background or shadowed areas and may overexpose the area of the welding arc. The underexposed image shall retrieve as much information of the welding arc area as possible without taking care of the image quality in the surrounding. The images are taken without any external lighting by the LEDs.



Figure 4.8.: *MAG, 85A, underexposed*

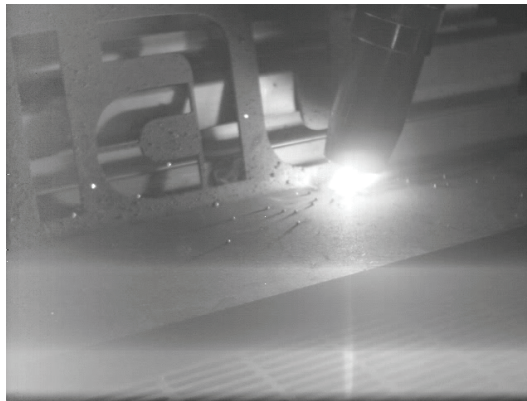


Figure 4.9.: *MAG, 85 A, overexposed*

It can be seen in figure 4.8 - 4.13, that the underexposed images on the left contains more information of the welding process. The surrounding areas which are less lighted by the arc are suppressed. The overexposed images give a good impression of the background and shadowed areas while the process area is clipped to maximum white (255 greyscale value).

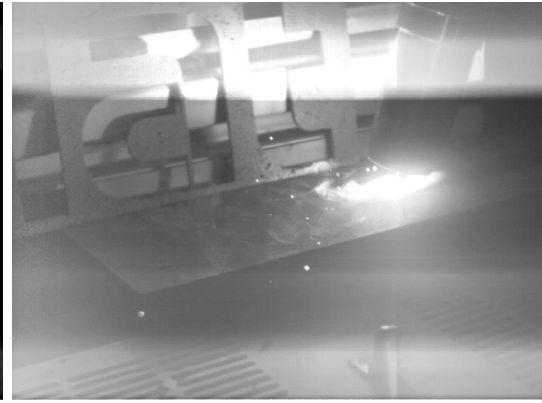
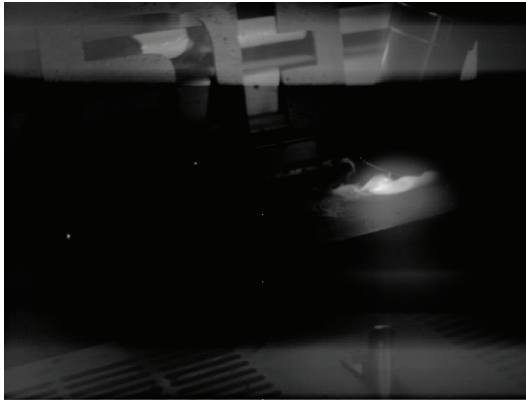


Figure 4.10.: *MAG, 120 A, underexposed* **Figure 4.11.:** *MAG, 120 A, overexposed*

The specific properties of the C-MOS camera chip technique can be seen in the overexposed areas. A CCD camera chip tends to bloom from the point of high brightness. A huger area than the real optical bright area appears in the saved digital image as maximum white. The electrons at the bright spot cause by means of the incoming photons, a flooding of the neighboured areas on the chip, so that they are measured as white, too.

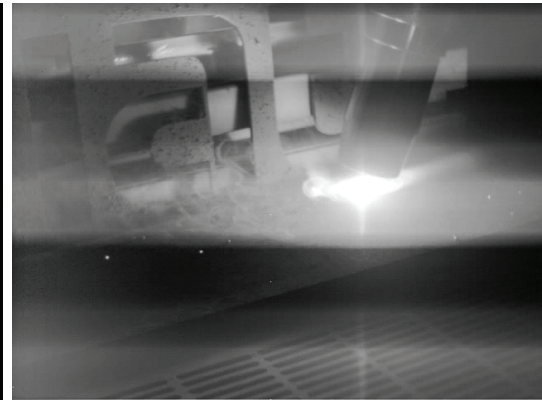


Figure 4.12.: *MAG, 220 A, underexposed* **Figure 4.13.:** *MAG, 220 A, overexposed*

4.1.2. Comparing Different Image Enhancement Algorithms

In this section the raw images shown in section 4.1.1 are processed by different image enhancement algorithms. The classical histogram equalization, the GLG, the CLAHE and the VBSAHE algorithms are used to compare their usefulness for welding images. The three different welding current of 85 A, 120 A and 220 A are used with the external LED lighting turned on.

MAG, 85 A The results for 85 A welding current are given in figure 4.15. The histogram equalization in subfigure a.) destroys the information in the process area by clipping it to maximum white. The background is over-amplified which means that the more bright regions are good visible while the darker regions occur more darkened and by that are less visible. This can be seen in figure 4.15 a.) nearby the **iat** logo on the left side. The same effect occurs for the difference at the white stripe which becomes more perturbing than in the original raw image of figure 4.3.

The GLG with its result in sub-figure b.) processes the background to darkness but does not bloom the welding process area which remains precise without losing image information. However the overall effect of enhancement is negative as the image details become less visible.

Enhancing the raw image with the CLAHE algorithm does change the welding process region to be less visible by lowering the contrast and adding brightness. As it can be seen in figure 4.15 c.), the background becomes highly structured, as single metal drips on the logos surface are now visible. The enhancement of the metal grid at the bottom of the image is improved without getting blended by an amplification of the white stripe.

The VBSAHE algorithm has been introduced in chapter 3. It segments the image by using the mean shift filter approach as presented in [53] with a succeeding floodfill segmentation. The single segments are individually enhanced by histogram stretching. In a final step the enhanced segments are merged for the resulting image. In figure 4.14 the segmentation of the raw input image in figure 4.2 is shown. Every edge is part of the border of a mono-coloured segment. Especially the area around the welding arc is divided into small segments and by that enhanced individually.

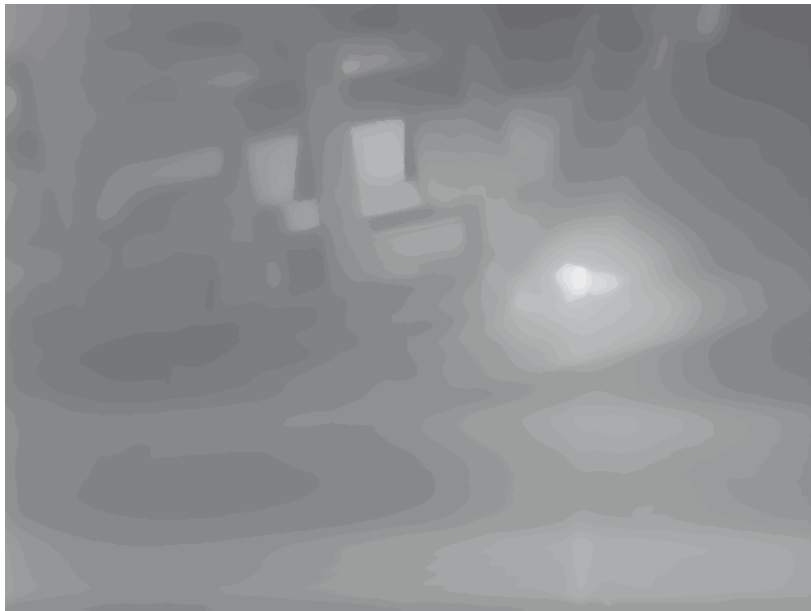


Figure 4.14.: *MAG, 85 A, LED On, Segmentation by Mean Shift approach*

4. Results

In figure 4.15 d.), resulted from the application of VBSAHE onto figure 4.3, the background is visible but with a slight lower contrast and it appears less exposed with respect to the CLAHE algorithm of figure 4.15 c.). The welding process is enhanced related to the original image while no aura artefact is added.

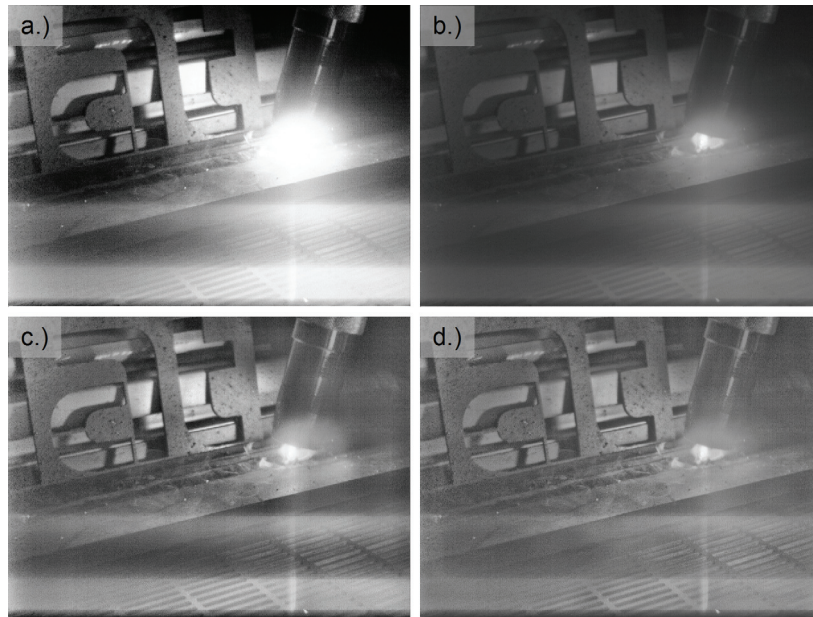


Figure 4.15.: *MAG 85 A: Enhanced with a.) Histogram Equalization, b.) Grey-Level-Grouping, c.) CLAHE, d.) VBSAHE*

MAG, 120 A Analogue to the result with a welding current of 85 A the histogram equalization for a welding current of 120 A boosts the area of the welding process and highly accentuates the low structured regions (see figure 4.16 a.)). The GLG algorithm remains the welding process to be visible but degrades the dark areas (see figure 4.16 b.)). The difference between the CLAHE and the VBSAHE improvement occurs in the welding process area with more contrast formed by the VBSAHE. Forming the bright and dark areas is more balanced for the VBSAHE, while the CLAHE does supply more dominant bright spots like the arc (see figure 4.16 c.) and d.)).

MAG, 220 A The three results for the GLG in figure 4.15 b.) - 4.17 b.) are not robust against the changes of the welding current. The first result for 85 A preserves the original viewing impression from the original image of figure 4.3, while the 120 A is processed to dark without touching the area of the welding process. For the process with 220 A welding current the image gets slightly darker related to the original. The reason is that the GLG maximizes an optimum criteria which measures the average distance of pixels on the greyscale. This maximum does not only depend on the grouping applied to the image, but as well on the image content. So different images may result in a different grey-level-grouping which maximizes the optimum criteria.

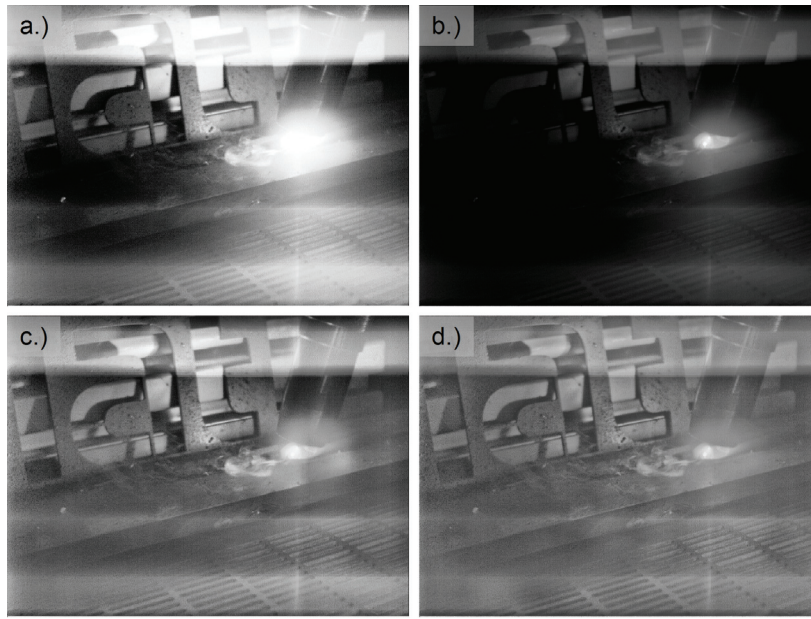


Figure 4.16.: *MAG 120 A: Enhanced with a.) Histogram Equalization, b.) Grey-Level-Grouping, c.) CLAHE, d.) VBSAHE*

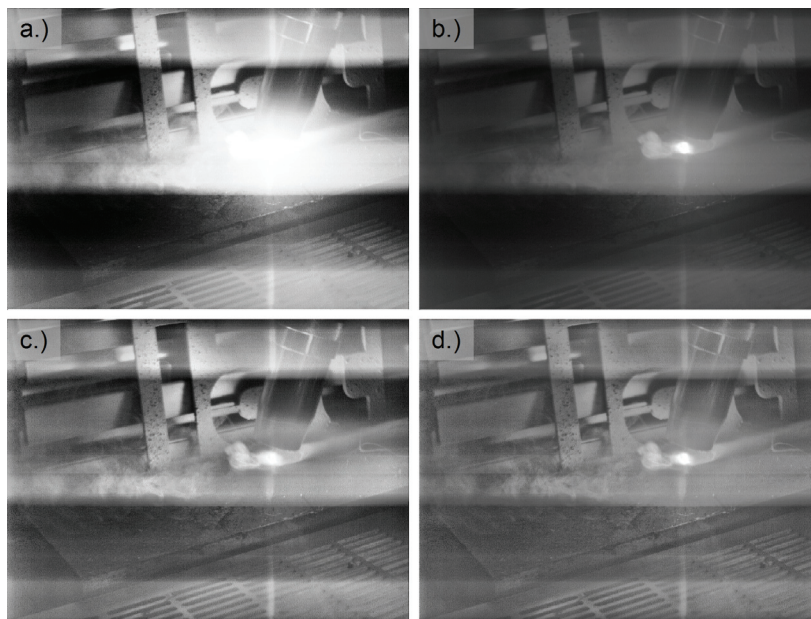


Figure 4.17.: *MAG 220 A: Enhanced with a.) Histogram Equalization, b.) Grey-Level-Grouping, c.) CLAHE, d.) VBSAHE*

4. Results

The evaluating of the results on the abstraction level of the local gradient change related to the original image gives an impression about the contrast improvement. The human visual system is not specifically taken into account as the reception quality of an image cannot be measured quantifiably. In the following figures 4.18 - 4.21 the differences between the gradient of the processed and the original image are shown. All the applied algorithms result solely in images of higher gradient than the original image has, so that no gradient decrease occurs i.e. no negative values are obtained. The colormapping is normalized to the 99.7 percentile¹ of the maximum contrast change of all algorithms. which is 54 supplied from the histogram equalization. For a better view the gradient images can be found enlarged in the Appendix A.5.

The histogram equalization enhances clear by edges such as the edges of the **iat** logo. It amplifies low structured areas whereby the high amount of local gradient change implies the amplification of noise (see figure 4.18). Regarding the rising welding current from left to right (85 A, 120 A, 220 A) in figure 4.18 the impression of a decreasing global intensity of the gradient enhancement is given. Calculating the mean values for figure 4.18 may only support but not prove this assumption as the image scene is and cannot be identical. Table 4.3 shows how the mean value decreases for the gradient, while the welding current is increased.

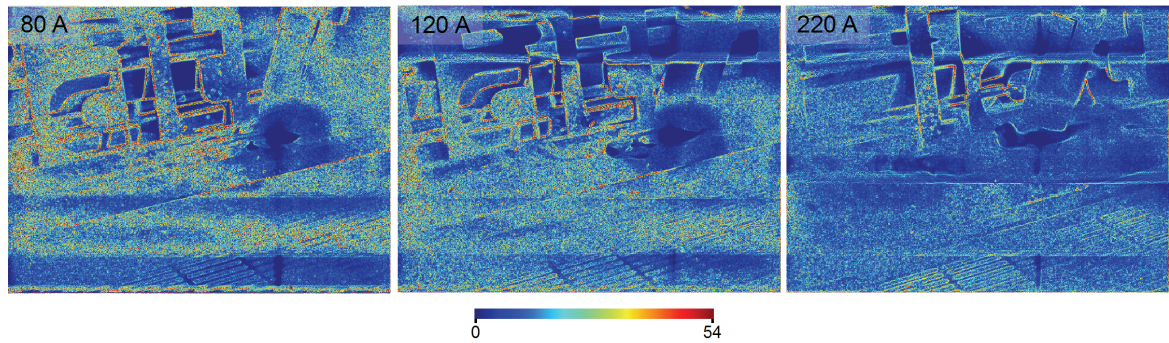


Figure 4.18.: *MAG: Gradient difference of histogram equalized images and original image for 85 A, 120 A and 220 A*

Welding Current	Mean value of gradient
85 A	15.82
120 A	13.188
220 A	10.24

Table 4.3.: *Mean values for the gradient differences*

The GLG merely enhances the gradient as it can be seen in figure 4.19. Neither low structured regions, nor the clear edges, nor the welding process are highly enhanced from the point of view of local contrast. Only some edges of single weld drops in the right image (220 A) are highly enhanced.

¹For Gaussian distributions the 99.7 percentile is covering three times the standard deviation from the mean value. By that the maximum outliers from (Gaussian) noise are filtered, while the content is remained

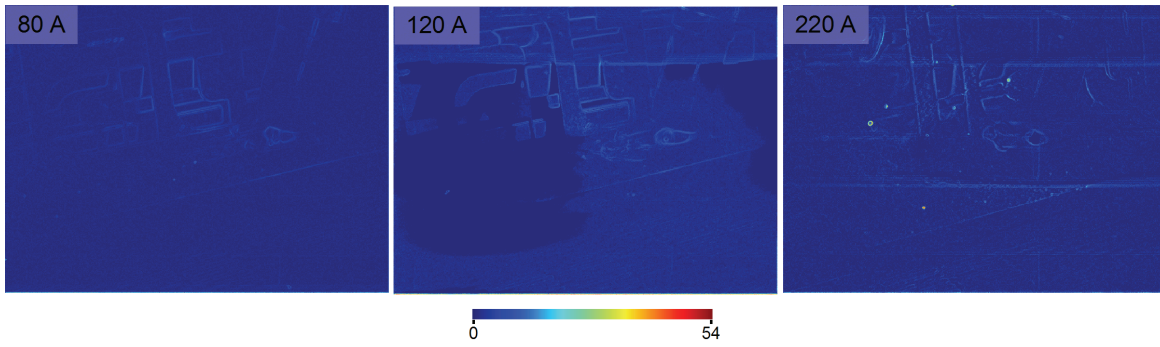


Figure 4.19.: *MAG: Gradient difference of GLG processed image and original image corresponding to 85 A, 120 A and 220 A*

The gradient difference image for the result of the CLAHE algorithm shows in figure 4.20 an intensive enhancement at clear edges such as the edges of the **iat** logo and a minimal effect at low structured regions. In contrary to the histogram equalization the noise is not amplified by the CLAHE algorithm.

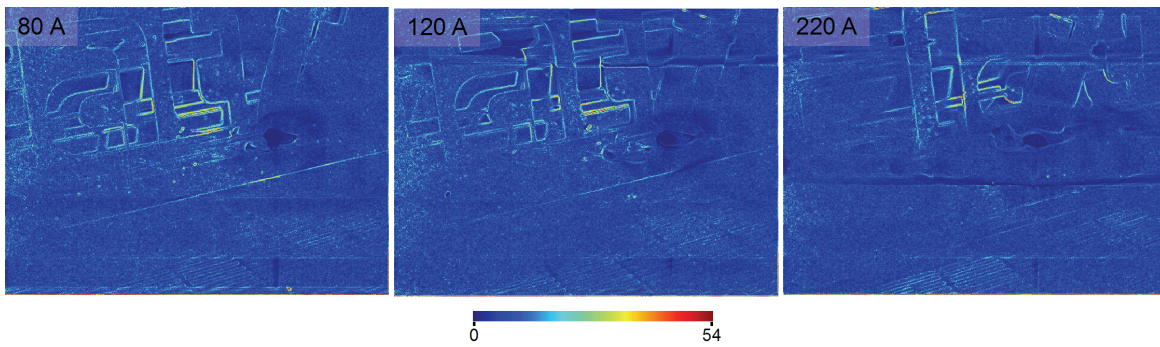


Figure 4.20.: *MAG: Gradient difference of CLAHE processed image and original image corresponding to 85 A, 120 A and 220 A*

Similar to the CLAHE algorithm, the VBSAHE enhances the clear edges such as the **iat** logo edges and merely changes the low structured regions. The global gradient change does not give the impression that it attenuated by a rising welding current.

In order to be able to compare the differences between the results of the CLAHE and VBSAHE algorithms a subtraction of the VBSAHE and CLAHE gradient is done and shown in figure 4.22. The colour mapping differs from the colour mapping of figure 4.18 - 4.20, where the mapping started from blue to green to red. The new colour mapping uses the red and green colour to map positive and negative values. Red pixels show -linear to their intensity- areas of higher improvement by the CLAHE. Green pixels represent regions where the VBSAHE enhances more the local gradient. As before, the colour mapping is bounded to the 99.7 percentile of the maximum difference in order to filter the outliers.

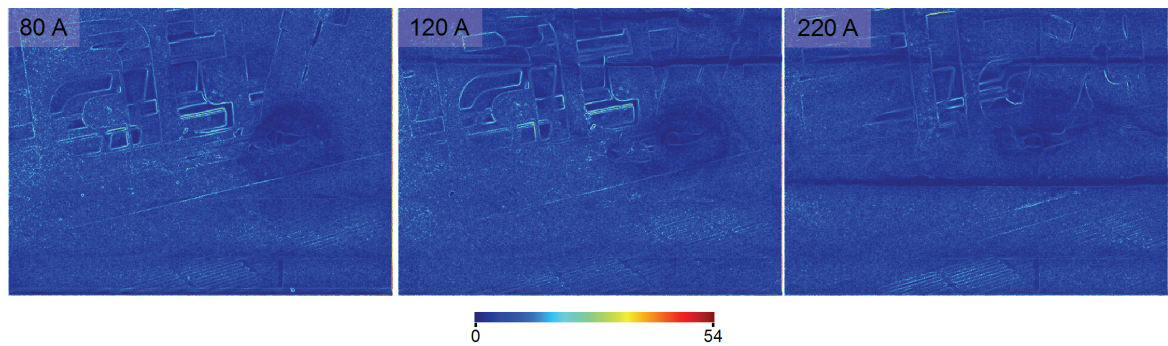


Figure 4.21.: *MAG: Gradient difference of VBSAHE processed image and original image corresponding to 85 A, 120 A and 220A*

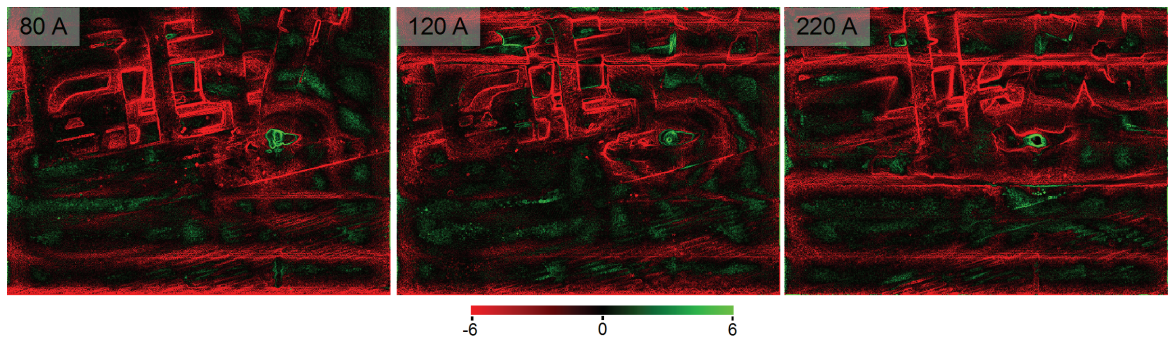


Figure 4.22.: *MAG: Gradient difference of VBSAHE and CLAHE results corresponding to 85 A, 120 A and 220A*

All three images give the same viewing impression independent of the welding current. The CLAHE algorithm improves more the clear edges while the VBSAHE amplifies more the low structured areas. Along with the view onto the real images resulting in figure 4.15 - 4.17, the gradient images of figure 4.22 support the well balanced impression for the VBSAHE in comparison to the CLAHE results.

4.1.3. Comparing Results of VBSAHE Processing with LED Lighting

In figure 4.23, the result of applying the VBSAHE algorithm on the raw image of figure 4.2 is given. In both cases with the LED on and off the image is enhanced from a smooth image with insignificant local contrast to an image with high local contrast and sharp edges. The metal grid in the foreground of figure 4.2 supplies a structured object which now becomes visible. The background with the **iat** logo is transformed from a dark area with low local structure to a surface with weld sputter on the metal and good visibility.



Figure 4.23.: *MAG, 85 A, VBSAHE Applied with LED Off (Left), LED On (Right)*

The comparison between the left and right image in figure 4.23 supplies the differences of the external lighting turned on and off. High power LEDs are used to highlight the surrounding. In region **A** the texture of the **iat** logo has a higher contrast as the LED have enough brightness to override slightly the welding arc light. In region **B** and **C** the LEDs highlight areas which are shadowed by the geometrical setup. In region **B** the far side from the welding torch can be seen after enhancement as well as the metal grid in region **B** where the shadowed edges of the grid are lighted. In region **D** reflections of the LED light source are visible. If the result of the contrast enhanced image is compared with the raw image in figure 4.3, then it can be seen that in the raw image the regions **A** and **B** were not identified to be highlighted by the LED although the contrast enhancement result of figure 4.23 makes it visible.

The more light is produced by the welding arc the less improvement is made by the LEDs as it can be seen in the regions **B**, **C** and **D**. No improvement is visible in the background at the **iat** logo of figure 4.24, which is highlighted in figure 4.23 as region **A**.

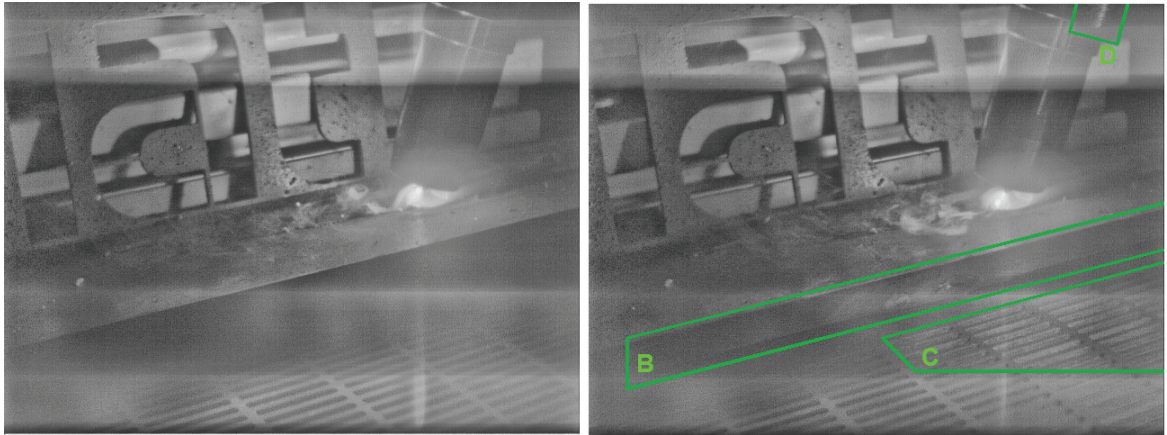


Figure 4.24.: *MAG, 120 A, VBSAHE Applied with LEDs Off (left) and LEDs On (right)*

A similar effect can be seen for the images taken at a welding current of 220 A in figure 4.25. The areas which are improved by the LED lighting are located only in areas shadowed from the welding arc (region **B** and **C**).

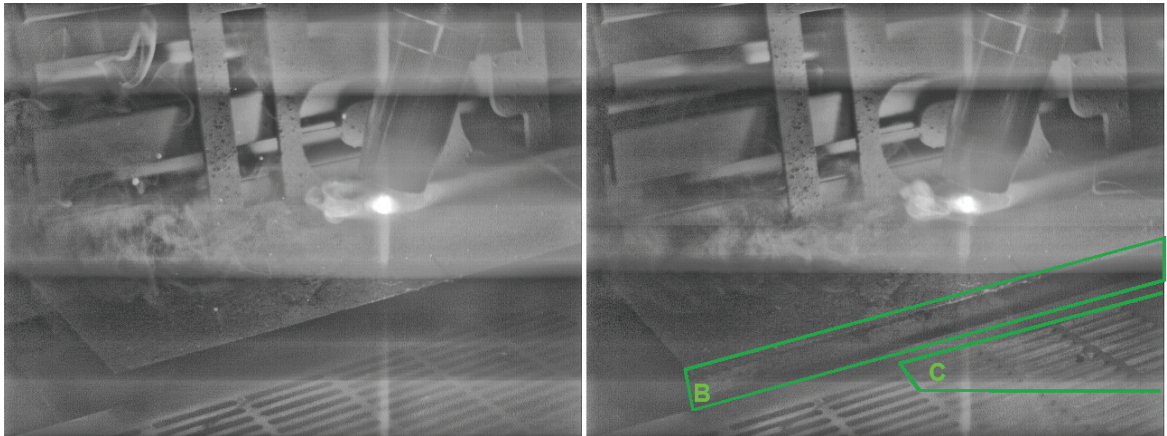


Figure 4.25.: *MAG, 220 A, VBSAHE Applied with LEDs Off (left) and LEDs On (right)*

4.1.4. Merging two Different Exposed Images

The composition of the resulting image from an under- and overexposed image consists of three types of pixels. Pixels around the welding process are supplied directly from the underexposed image. In figure 4.26 these pixels are marked with a red colour. The background pixels are taken directly from the overexposed image. They are marked in figure 4.26 with a blue colour. These pixels do not contain any information in the underexposed image as these pixels are clipped to black. Some regions are available in both images. Following the merging algorithm of section 3.1.4 they are merged by using the mean value from both images and are marked with a green colour.

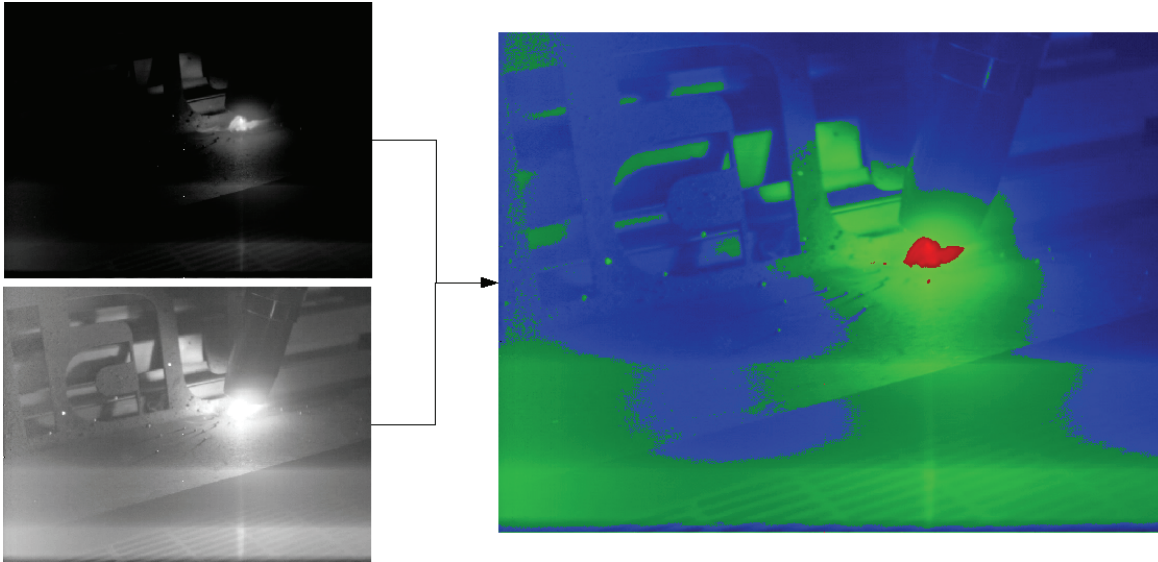


Figure 4.26.: *MAG process at 85 A: Merge composition of the resulting image from the underexposed (red), both (green) and overexposed (blue) image*

Merging the images results in data with exceeding the value range of a standard grey scale image of a computer. More than 256 different grey scales values are not available on the screen and nor the human eye can perceive all. One way to make it visible is to use false colours which map a high amount of different grey scale values to a colour map. The colour map is deviated from the hue-saturation-value colour model, where the hue component is varied (see [74]). The colour map begins with red, passes through yellow, green, cyan, blue, magenta and returns to red.

MAG, 85 A In figure 4.27 such a mapping is made to show the enhanced information contained in the merging result. The magnified area of the welding process shows that the image information contains a higher number of different grey values. If only the data taken from the underexposed image is taken into account (marked with red in figure 4.26) then 98 different grey values form the information of the welding process. By contrast the amount of an adequate area from a direct single shot as presented in section 4.1.1, covers 62 grey values. This measurement can only be used qualitatively as the region borders of the welding process are not clearly defined in the single shot image.

The resulting grey scale image in figure 4.28 is the linear transformation of the false colour image (figure 4.27) with 389 grey values to a 256 greyscale image. The transformation is equal to a histogram stretching where it is used for image improvement with the only difference that it is now done from a large data domain to a smaller one.

By applying the VBSAHE algorithm the source image needs to be segmented before enhancing. The result of the detailed segmentation of figure 4.28 is shown in figure 4.29. It gives an impression about the amount and individual shape of the regions. After enhancing, the merged regions form a new image enriched in details as given in figure 4.30.

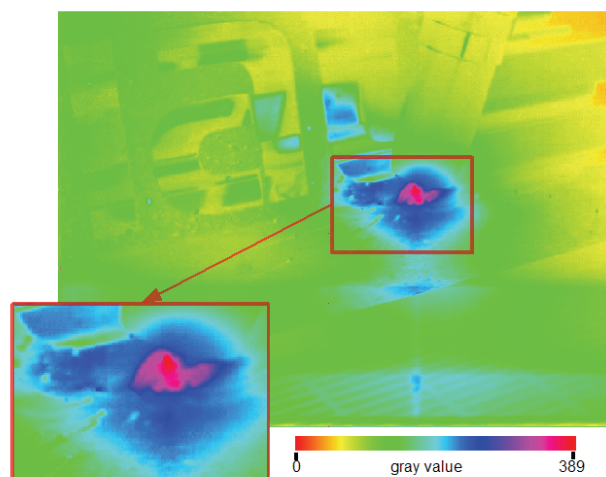


Figure 4.27.: *MAG, 85 A: False Colour of the merged images with 389 greyscale values*

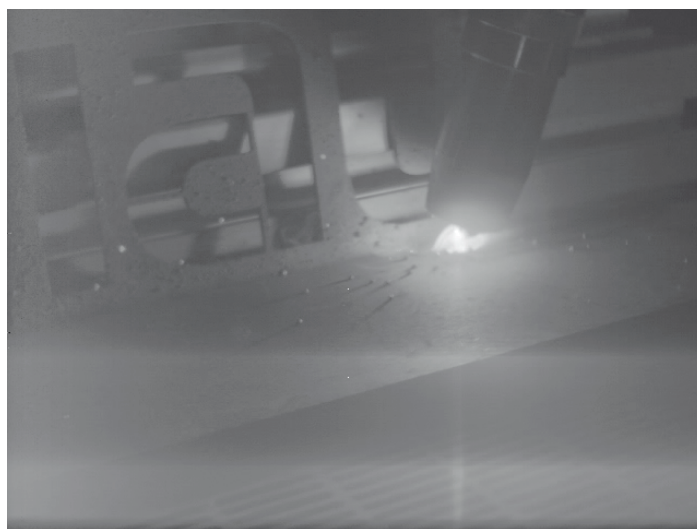


Figure 4.28.: *MAG, 85 A: Result of the merging process*

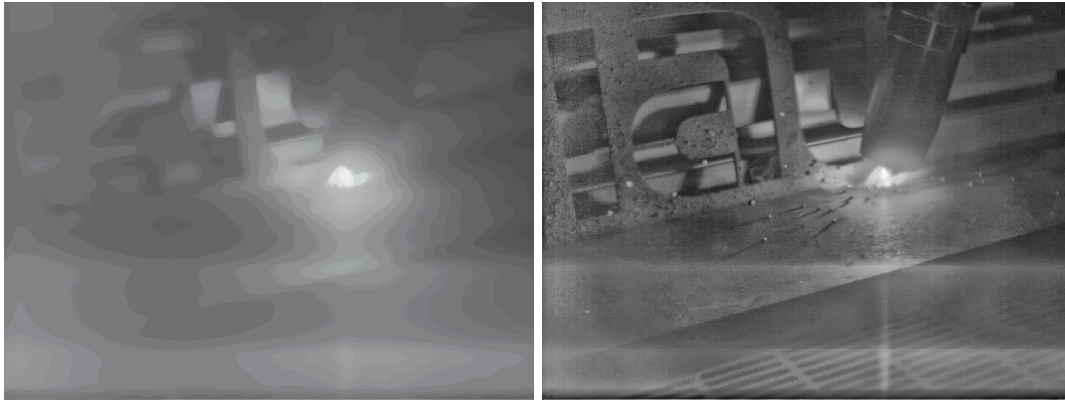


Figure 4.29.: *Segmentation of the merged image result* **Figure 4.30.:** *MAG, 85 A: Result of the VBSAHE processing*

MAG, 120 A For the process with 120 A welding current, the image composition from the underexposed image does use more regions. Not only the welding process supplies data in the underexposed image. Some bright direct lighted spots as seen in figure 4.31 are used as well as the welding arc region.

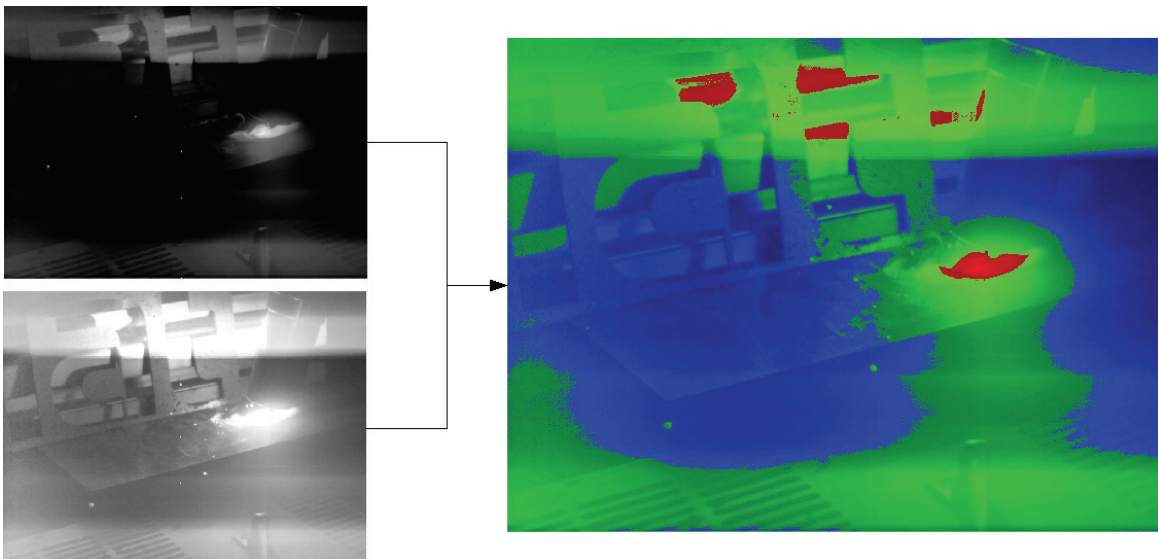


Figure 4.31.: *MAG process at 120 A: Merge composition of the resulting image from the underexposed (red), both (green) and overexposed (blue) image*

The composition results in an image using 337 different greyscale values and so giving more information at the welding spot, than single shot images (see figure 4.32).

By linear tone mapping the image in figure 4.33 to 255 greyscale values the result appears rather dark. It can be made re-visible by the VBSAHE algorithm (see figure 4.34).

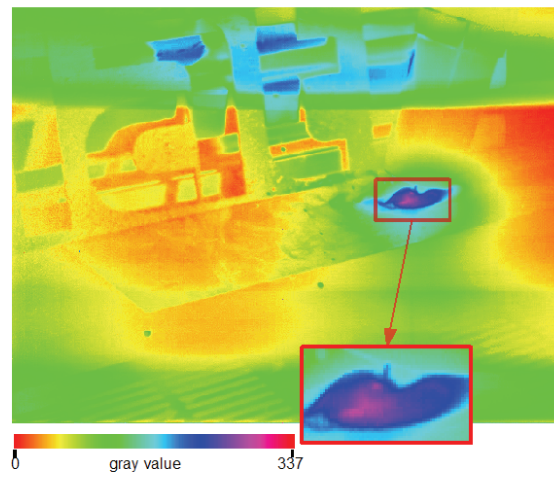


Figure 4.32.: *MAG, 120 A: False Colour of the merged image with 337 greyscale values*

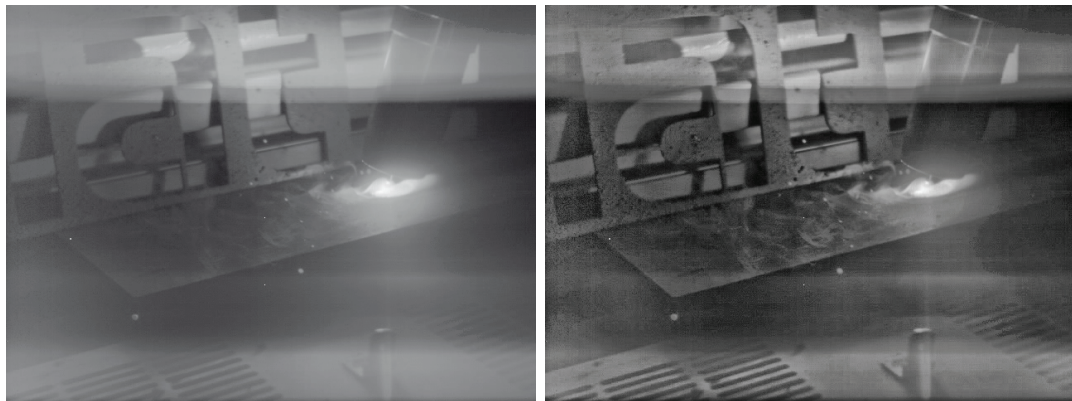


Figure 4.33.: *MAG, 120 A: Result of the merging process*

Figure 4.34.: *MAG, 120 A: Result of the VBSAHE algorithm*

MAG, 220 A Similar to the example corresponding to 85 A welding current is the result for the brighter welding current corresponding to 220 A. The composition in figure 4.35 is as well done by a small spot of the welding arc from the underexposed image (red), an huge area where the mean value of the both input images is taken (green) and parts of the dark regions taken from the overexposed image (blue).

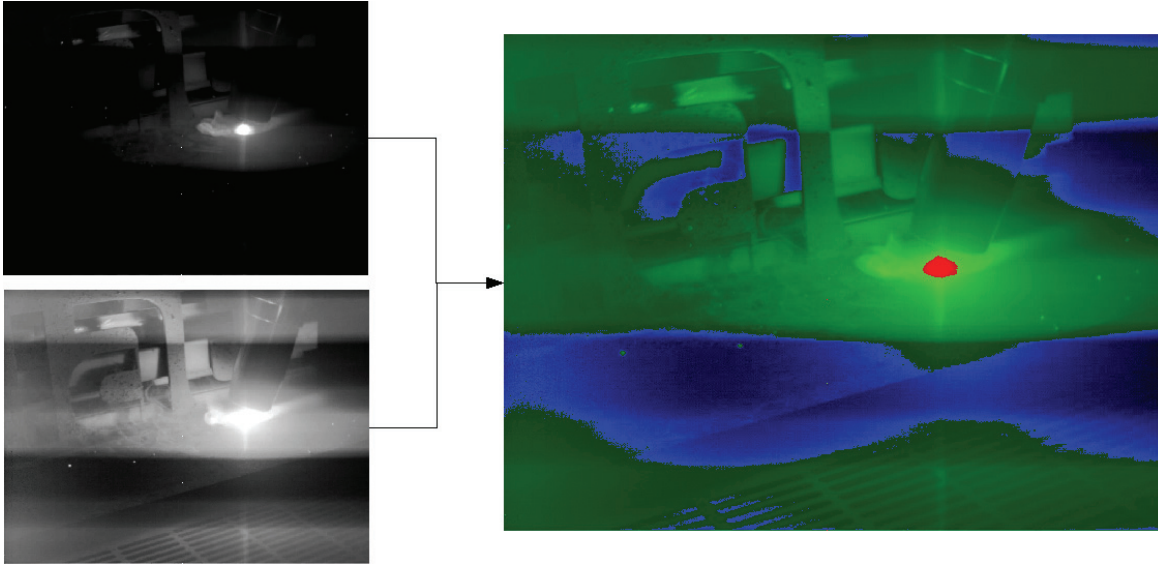


Figure 4.35.: *MAG process at 220 A: Merge composition of the resulting image from the underexposed (red), both (green) and overexposed (blue) image*

The process with its welding arc and melting pool covers at 220 A an amount of 37 grey values. This lower amount of different grey values fits to the technical specifications of the used C-MOS camera sensor. As described in section 2.2, its logarithmic response does map the same absolute difference at low lighting to a higher amount of grey value range than for the same absolute difference at bright lighting. This means that the process with its clearly bordered region is mapped to a smaller range of grey values which can be seen in the magnified region of figure 4.36.

The enhancement with the VBSAHE algorithm of the merged and tone mapped image (see figure 4.37) supplies again a better view onto the surrounding (see figure 4.38). In the process area no specific details are visible, as they do not exist in the source image. An interesting improvement occurs in the area of the smoke on the left side of the welding torch. By that the background in that area becomes more visible. The huge global brightness differences related to the white stripe area are lowered by the VBSAHE algorithm.

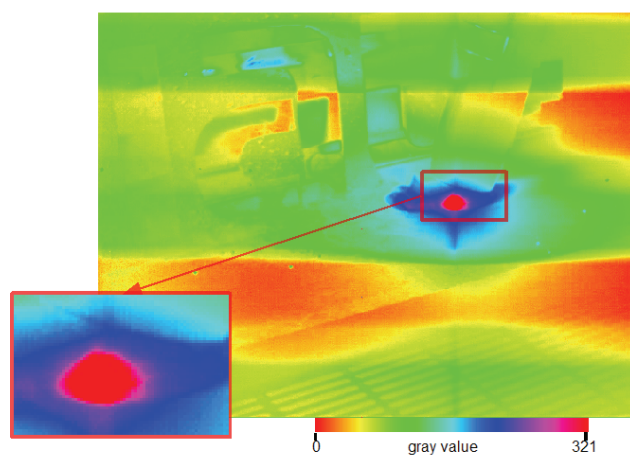


Figure 4.36.: *MAG, 220 A: False Colour of the merged image with 321 greyscale values*

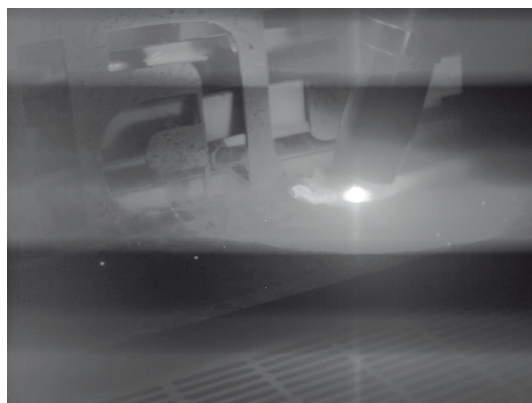


Figure 4.37.: *MAG, 220 A: Result of the merging process*



Figure 4.38.: *MAG, 220 A: Result of applying the VBSAHE algorithm*

4.2. Pulsed MIG process

The pulsed MIG process does not differ extensively from the setup of the MAG process. The main difference is the use of Argon as inert gas to protect the seam from oxidation. As base material a sheet of 4 mm thickness of corrosion-resistant aluminium magnesium alloy is used with an AlMg4.5MnZr wire of 1.2 mm diameter. The selected welding currents of 85 A, 180 A and 240 A give an impression of the process at different brightness condition. The 85 A welding current does not make sense concerning the quality of the welding seam as the power of the arc is not sufficient to crack the aluminium oxide layer. The defect that occurs is that melted material from the filler material (wire) lays down on the base material forming a rope. The selected 180 A and 240 A give two applications with a lower medium and higher medium welding current. The brightness produced by the arc is less of higher current than for the MAG process, which can be seen by comparing table 4.2 for the MAG and table 4.4. The original camera images are shown in figure 4.39. It can be seen that sparks and welding drips are more present than during the MAG welding considered in the previous section. In the following the evaluation is done here more concise and confines to the comparison of the original image with the results of CLAHE and VBSAHE.

Welding Current [A]	Brightness [lux]
80	$0.7 \cdot 10^3$
180	$2.4 \cdot 10^3$
240	$3.0 \cdot 10^3$

Table 4.4.: *Brightness of pulsed MIG process at 1 m distance from the welding torch*

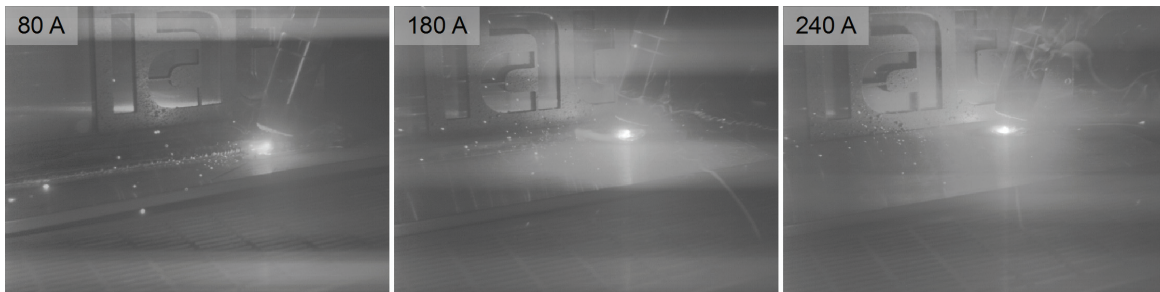


Figure 4.39.: *Original camera image for MIG welding process*

The result of the CLAHE for all chosen currents amplifies the white stripe caused by the rolling shutter of the camera in combination of the pulsed welding process. The process region appears bloomed with low information at the welding arc (see figure 4.40).

In contrast to the CLAHE results, the image resulting from VBSAHE in figure 4.41 appears less crisp related to the global contrast. The welding arc region is more precisely exposed without the amplification of the white stripe. The background containing the **iat** logo, results

4. Results

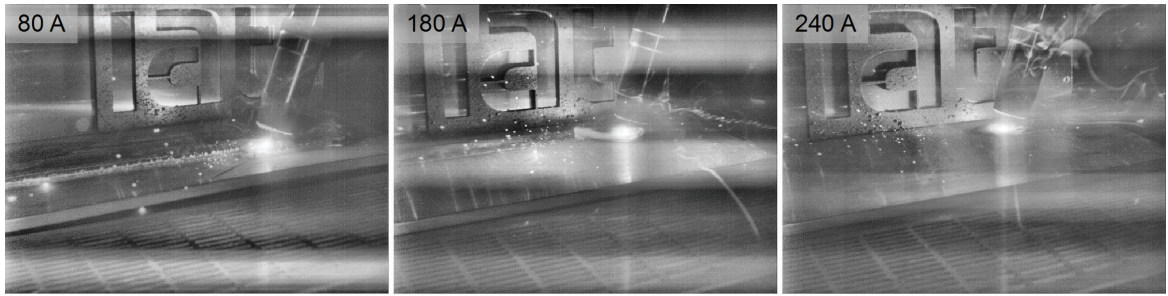


Figure 4.40.: MIG: Result of the CLAHE for 80 A, 180 A and 240 A welding current

for higher welding currents to a brighter scene. This effect is less visible in the CLAHE results in figure 4.40.

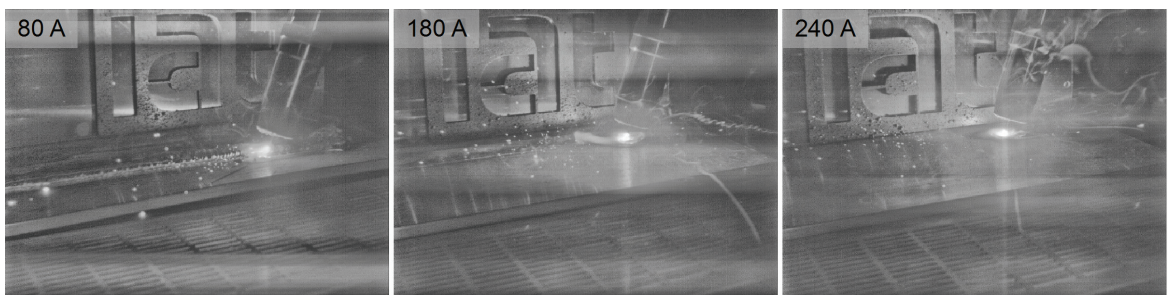


Figure 4.41.: MIG: Result of the VBSAHE with 80 A, 180 A, 240 A welding current

4.3. Pulsed TIG Process

To broaden and to proof the applicability of the welding observation system, the Tungsten-Inert-Gas process is used with mild steel. The used machine is a **TETRIX 300 COMFORT activArc** from the producer **ewm**. Here a pulsed DC process is used with negative polarity at the tungsten electrode and contactless high frequency ignition. The selected current is 230 A in order to sufficiently melt the 4 mm thick sheet. A resulting original image can be seen in figure 4.42 a.). The brightness of the welding arc in the distance of 1 m has only 801 lux and so much more less than the MAG equivalent which was $8.13 \cdot 10^3$ lux (see table 4.2). This circumstances does reduce the contrast dynamics in the scene. The figure 4.42 b.) shows the segmentation resulting from the Mean Shift approach. The segments are smoothly arranged around the welding arc, which again supports the functionality of the VBSAHE approach and takes care about the content while improving the image.

In figure 4.43 the result of the VBSAHE (a.) and the CLAHE (b.) algorithm are shown. The CLAHE algorithm does destroy the information in the welding arc area by clipping it to white, while the VBSAHE improves the local contrast around the arc.

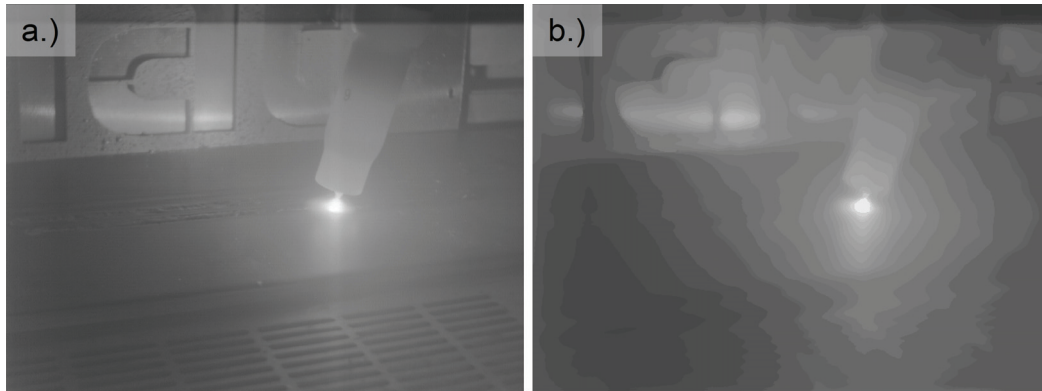


Figure 4.42.: *TIG DC pulsed 230 A: a.) Original b.) Segmentation by Mean Shift approach*

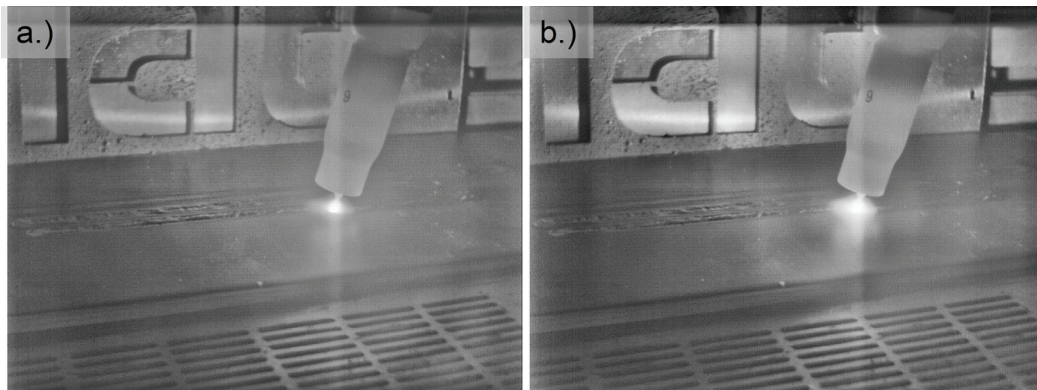


Figure 4.43.: *Result of contrast enhancement: a.) VBSAHE b.) CLAHE*

4. Results

These results are supported by the difference in the gradient of the results in figure 4.44. As in the previous sections the differences of the VBSAHE and the CLAHE are coded in green colour for a stronger VBSAHE gradient, while red shows a stronger gradient resulted by the CLAHE algorithm. The region around the welding arc is coloured green, which means that

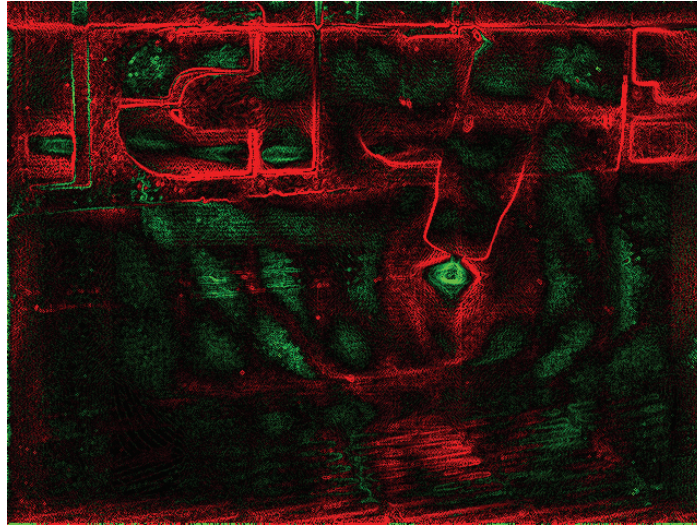


Figure 4.44.: *Difference of image gradient for VBSAHE and CLAHE results*

the local contrast is higher for the image enhanced by the VBSAHE algorithm. Other regions like clear edges at the **iat** logo in the background are more enhanced by the CLAHE, while smooth areas are more enhanced by the VBSAHE.

4.4. The Selective Automatic Darkening Filter

The prototype helmet (see chapter 3) is used with a mannequin head. It gives the opportunity to place an external camera at the eye position (see figure 4.45). After starting the system it has to be calibrated by using optical markers of the ARToolkit. These markers have to be placed around the working distance of the welder, who may then use the system at this specific distance. The calibration and the running system is done with the mannequin camera instead of a human user to document the results. For human user the calibration can be reduced to around 25 s after some time of practice by repetition. One drawback is here that the calibration needs to be done every time the user puts the helmet on as well as after raising it up. It must be done as the position of the camera and GLCD related to the eye is changed every time of moving the helmet.

The response time of the GLCD is about 150-175 ms as the pixels of the GLCD are set by serial access. The frame rate of the GLCD is lower than the detection threshold of the human eye for fluent movements. The abilities of the GLCD are restricted to squared shapes. Implementing other shapes than squares by building an entire Graphics Device Interface (GDI) would go along with a lower frame rate as for the square the most effective



Figure 4.45.: *Mannequin with camera in the right eye*

access to the pixels can be used. The low resolution of 132 by 147 pixels with the square size of 0.05 mm side length for one pixel causes insufficiencies related to the minimal size of the darkening in the field of view. The mock-up for the SADF principle uses a high bright LED mounted at the nozzle of a fake welding torch in order to simulate arc welding. In figure 4.46 three frames are shown of the running SADF system meanwhile simulated welding. The

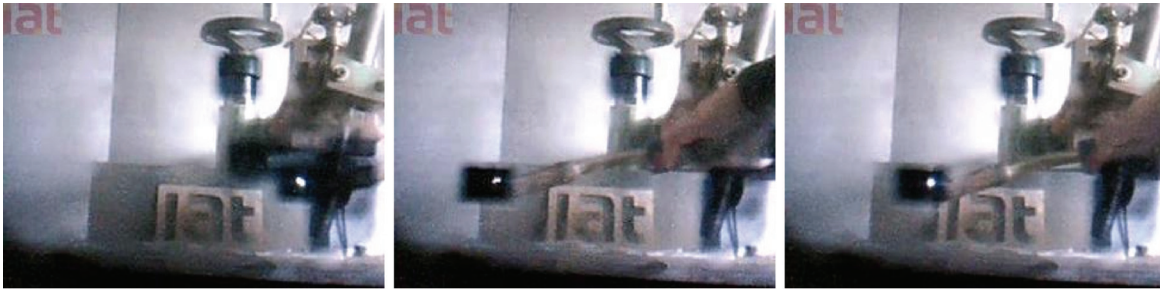


Figure 4.46.: *SADF testing by mannequin view*

position of the LED which is the brightest spot in the image, is extracted by thresholding the image and to darken the area of the bright pixels. The size of the square is selected bigger than the size of the bright pixel area in order to counteract the low frame rate of the GLCD. The low frame rate delays the correct covering of the light source by the darkened GLCD during movements. From the middle to the left frame in figure 4.46 a movement of the torch is made to the right. The delay can be seen in the right frame as the covering square is not centred on the light source.

During testing the problems of the system became visible. First the assumption of a constant working distance is not reliable. Depending on the welding course it may vary from 20 cm to 80 cm². Another issue is the accommodation of the eye. The human eye has to adapt to the distances in the field of view where it does not cover as much field of depth as the camera

²Working distances are minimum and maximum values based on interviews with welders from EWM

lenses may do, so that the black square covering the glaring light may not be seen sharp but blurred by the human observer.

In figure 4.46 the background and the black squares of the GLCD are good viewable. Although the background is better visible the black square is precisely noticeable. If a human uses the system, he does not recognize a black square. The darkening of the GLCD is seen as an fluent smooth darkening around the square center. Different results are made with an optical-see-through HMD, where the optics are well aligned to the users view, but the darkening abilities of such an HMD is very low and by that not useful for welding protection.

4.5. Conclusions

This thesis elaborates a system for the video observation of high dynamic contrast scenes with the application of welding. The development of a SADP system was achievable only by a feasibility study due to non-existent adequate hardware. The lack of a 2D GLCD only gives the opportunity to build a mock-up system, which keeps the idea of a SADP system alive (see section 3.3 and section 4.4).

The problems of having on the one side a camera for high dynamic contrast but only eight bits to record the greyscale is a drawback which bounds the quality of the raw image. One step to overcome with such limitations is to use the toggle merging with two images containing information of two different brightness ranges. It ends up in an image with more than 256 greyscale values, which has to be tone mapped to eight bits information for displaying on a monitor. This technique assured to use all the available 256 steps of greyscale as the input for the next algorithmic step of contrast enhancement (see section 3.1.4).

After widening the input data range of the image, the second most important question arose related to enhancing the image information. The question of what is the information of the image and how can it be enhanced ended up at the VBSAHE algorithm after examining different contrast enhancement approaches. This algorithm individually enhances the segmented information of the image. It takes the eight bit greyscale and enhances the local contrast, so that globally seen, the information becomes better visible as information by small greyscale differences can be enhanced without overrunning the limitations of 256 greyscale values of the output image (see section 3.2.4).

Related to the application of welding the problem of synchronizing the camera onto the welding process gave a milestone in video quality for the human observer. The flickering was not abolished but stabilized to a fixed position without depending on any machine interface. The optical trigger with automatic alignment of the sensor system to the brightness condition makes this system robust for a wide range of applications related to welding method, working distance and conditions (see section 3.1.2).

With the integration of the trigger, the flashing of the scene with high power LED became feasible. Although the effect of this technique is limited to widely used medium welding

currents, it produces a lighted areas which are lying in the shadow of the glaring welding arc (section 3.1.3).

In the future the aspects of a SADF system need to be observed regarding available GLCDs which may darken sufficiently the bright spots and follow movements with an adequate frame rate. An alternative suggestion is to re-think the idea of a video see-through welding helmet [9] were the user sees the scene by a video see-through HMD while the scene is captured by a camera system; a camera system as it is researched here.

Side effects of this research are the examination of the morphological top-hat operator (see section 3.2.5) and the application of the Wiener filter for denoising the image (see section 3.2.3). The lack of a defined helmet fixation on the user's head to preserve a valid calibration, needs further investigation for an alternative approach in order to avoid tedious calibrations.



Appendix

A.1. Mathematical Conventions

x, X	:	scalar
$x(\dots), X(\dots)$:	function
\vec{x}, \vec{X}	:	vectors in 2D (lowercase) and 3D (capital)
\mathbf{X}	:	matrix

A.2. Linear Algebra

A small introduction taken from [71] about important equations is given here

determinants The determinant of the product of two quadratic matrices \mathbf{A} and \mathbf{B} is the same as the product of their single determinants

$$\det(\mathbf{A} \cdot \mathbf{B}) = \det(\mathbf{A}) \cdot \det(\mathbf{B}) \quad (\text{A.1})$$

Transposed product The transposed matrix of matrix product is equal to the product of the two transposed matrices:

$$(\mathbf{A} \cdot \mathbf{B})^T = \mathbf{A}^T \cdot \mathbf{B}^T \quad (\text{A.2})$$

Inverse The inverse of a orthogonal matrix is equal to its transposed

$$\mathbf{A}^{-1} = \mathbf{A}^T \quad (\text{A.3})$$

Skew symmetric matrix A cross product can be mapped to a dot product by using a skew symmetric matrix. The skew symmetric matrix of a 3D vector is defined as :

$$[\vec{a}]_{\times} = \begin{bmatrix} 0 & -a_3 & a_2 \\ a_3 & 0 & -a_1 \\ -a_2 & a_1 & 0 \end{bmatrix} \quad (\text{A.4})$$

and the cross product can be written as

$$\vec{a} \times \vec{b} = [\vec{a}]_{\times} \vec{b} = \left(\vec{a}^T [\vec{b}]_{\times} \right)^T$$

Skew symmetric matrix and dot product The dot product for any skew symmetric matrix defined by $[\vec{t}]_{\times}$ with a non-singular matrix \mathbf{M} can be written as:

$$[\vec{t}]_{\times} \mathbf{M} = [\mathbf{M}^{-1}]^T [\mathbf{M}^{-1} \vec{t}]_{\times} \quad (\text{up to scale}) \quad (\text{A.5})$$

RQ-Decomposition The RQ-decomposition $[\mathbf{RQ}] = RQ()$ of a rectangular Matrix \mathbf{M} into a upper triangular matrix \mathbf{R} and an orthogonal matrix \mathbf{Q} can be derived from a more widely used QR-decomposition.

$$\mathbf{M} = \mathbf{R} \cdot \mathbf{Q} \quad (\text{A.6})$$

Deriving the RQ-decomposition from the QR-decomposition may be calculated by:

$$\tilde{\mathbf{M}} = \tilde{\mathbf{Q}} \cdot \tilde{\mathbf{R}} \quad (\text{A.7})$$

$$\mathbf{M}^{-1} = \left(\tilde{\mathbf{Q}} \cdot \tilde{\mathbf{R}} \right)^{-1} = \tilde{\mathbf{R}}^{-1} \cdot \tilde{\mathbf{Q}}^{-1} = \tilde{\mathbf{R}}^{-1} \cdot \tilde{\mathbf{Q}}^T \quad (\text{A.8})$$

The matrix $\tilde{\mathbf{R}}^{-1}$ gives the upper triangular matrix and $\tilde{\mathbf{Q}}^T$ the orthogonal matrix \mathbf{Q} .

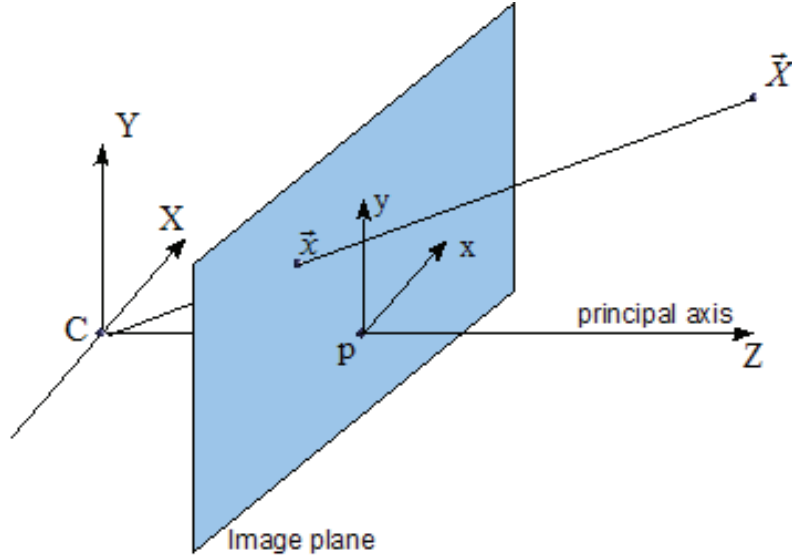


Figure A.1.: Pinhole camera geometry with C the camera centre and p the principal point

A.3. 2D Projection of the 3D World

A.3.1. Finite projective camera

A simple pinhole camera and its mapping of 3D point in homogenous coordinates $\begin{pmatrix} \vec{X} \end{pmatrix}$ to its 2D image plane $\begin{pmatrix} \vec{x} \end{pmatrix}$, can be written as:

$$\begin{pmatrix} X \\ Y \\ Z \\ 1 \end{pmatrix} \mapsto \begin{pmatrix} f X \\ f Y \\ Z \end{pmatrix} = \begin{bmatrix} f & 0 & 0 \\ 0 & f & 0 \\ 0 & 0 & 1 \end{bmatrix} \begin{pmatrix} X \\ Y \\ Z \\ 1 \end{pmatrix} \quad | f : \text{focal length} \quad (\text{A.9})$$

$$\vec{x}_{cam} = \mathbf{K} \vec{X} \quad (\text{A.10})$$

As it can be seen in figure A.1 the coordinate system of the image plane with origin p and the camera with C as the origin have the same orientation and though the same Z-axis. This simplifies the mapping from the 3D camera system to the 2D image plane. If the mapping is done from a 3D world coordinate system to an image plane based on the camera coordinate system, then the mapping in equation A.9 has to be expanded with a transformation term from the world to camera coordinates which consists of a rotation matrix \mathbf{R} and the coordinates \vec{C} of the origin in the world coordinate system:

$$\vec{x}_{cam} = \begin{bmatrix} \mathbf{R} & -\mathbf{R} \vec{C} \\ 0 & 1 \end{bmatrix} \begin{pmatrix} X \\ Y \\ Z \\ 1 \end{pmatrix} = \begin{bmatrix} \mathbf{R} & -\mathbf{R} \vec{C} \\ 0 & 1 \end{bmatrix} \vec{X} \quad (\text{A.11})$$

Which leads together with equation A.9 to

$$\vec{x} = \mathbf{K} \mathbf{R} \left[I \mid -\tilde{\mathbf{C}} \right] \vec{X} \quad (\text{A.12})$$

$$= \mathbf{P} \vec{X} \quad (\text{A.13})$$

with \vec{X} in world coordinate frame.

Up to yet the mapping to the image plane is still measured in distance units like meter or inches, but a digital camera uses pixels. For this the number of pixels per unit distance m in image coordinates is introduced and changes the use of the focal length f by mapping to a focal length in pixel coordinates $\alpha = f m$. The used C-MOS camera has squared pixels with identical dimension in x and y direction. This is why only one variable m is used.¹ The camera Matrix \mathbf{K} changes for a mapping to pixel coordinates to:

$$\mathbf{K} = \begin{bmatrix} \alpha & x_0 & 0 \\ & \alpha & y_0 & 0 \\ & & 1 & 0 \end{bmatrix} \quad (\text{A.14})$$

With x_0 and y_0 as the principal point derived from the pixel coordinates $p_0 = (p_x, p_y)$ with $x_0 = m p_x$ and $y_0 = m p_y$.

Back projection The ray back-projected from \vec{x} on the image plane by the camera system formed with \mathbf{P} is given by a one parameter family of solutions, which forms a 3D line

$$X(\lambda) = \mathbf{P}^{-1} \vec{x} + \lambda \mathbf{C} \quad (\text{A.15})$$

Camera Calibration

To calibrate a camera, the unknown \mathbf{P} can be calculated by using sufficient known 3D points \vec{X}_i and their projection \vec{x}_i onto the image plane as used in A.13. For an exact solution six precise pairs of 3D to 2D corresponding points are needed to solve the problem. But all measurements include measurement errors and so noise. An exact solution for the camera matrix \mathbf{P} is not achievable and can be iteratively solved by minimizing an optimum criterion. In this case a bigger number of measured correspondences $\vec{X}_i \rightarrow \vec{x}_i$ is used for a more precise solution. For such an approximated solution the Gold Standard algorithm is used [71]. It needs an initial estimate using a linear method to be calculated before minimizing the projection error using an iterative algorithm such as Levenberg-Marquardt [75], [76]. Before starting to find any solution the image points and the space points need to be normalized by a translation and scaling so that the centroid of the points is in the coordinate origin and their average distance from the origin is $\sqrt{2}$.

$$\vec{x}_i = \mathbf{T} \vec{x}_i \quad (\text{A.16})$$

$$\vec{X}_i = \mathbf{U} \vec{X}_i \quad (\text{A.17})$$

¹If a camera has non-squared pixel, as some CCD cameras have, two different value for the number of pixel per unit distance in x and y direction has to be used and effect two different (pixel based) focal length in x and y direction.

Linear solution The inhomogeneous camera projection equation A.13 can be changed to an homogenous problem by applying the cross product from the left with \vec{x} to both sides:

$$\vec{x}_i = \mathbf{P} \vec{X}_i \quad (\text{A.18})$$

$$\vec{x}_i \times \vec{x}_i = \vec{x}_i \times [\mathbf{P} \vec{X}_i] \quad (\text{A.19})$$

Now the cross product can be realigned by using instead a skew symmetric matrix. The way to use the skew symmetric matrix is sketched as follows with \vec{p}_i^T denoted as the i-th row of the matrix \mathbf{P} and $\vec{x}_i = (x_i, y_i, w_i)^T$

$$0 = \vec{x}_i \times \begin{pmatrix} \vec{p}_1^T \vec{X}_i \\ \vec{p}_2^T \vec{X}_i \\ \vec{p}_3^T \vec{X}_i \end{pmatrix} \quad (\text{A.20})$$

$$= \begin{bmatrix} 0^T & -w_i \vec{X}_i^T & y_i \vec{X}_i^T \\ w_i \vec{X}_i^T & 0^T & -x_i \vec{X}_i^T \\ -y_i \vec{X}_i^T & x_i \vec{X}_i^T & 0^T \end{bmatrix} \begin{pmatrix} \vec{p}^1 \\ \vec{p}^2 \\ \vec{p}^3 \end{pmatrix} \quad (\text{A.21})$$

$$0 := \mathbf{A} \cdot \vec{p} \quad (\text{A.22})$$

The overdetermined system is received by stacking for each of the n normalized corresponding pairs $\vec{X}_i \rightarrow \vec{x}_i$ equation A.22, to a $2n \times 12$ matrix \mathbf{A} . Only two equations of A.22 can be used for each correspondence $\vec{X}_i \rightarrow \vec{x}_i$ as the third is not linearly independent. In order to achieve an optimal solution for \vec{p} for the $2n \times 12$ matrix \mathbf{A} the Singular Value Decomposition (SVD) will be used. The unit singular vector corresponding to the smallest singular values is the optimal solution for \vec{p} . Especially if $\mathbf{A} = \mathbf{U}\mathbf{D}\mathbf{V}^T$ with \mathbf{D} diagonal matrix with positive diagonal entries, arranged in descending order, then an optimal solution for \vec{p} is the last column of \mathbf{V} .

So the matrix $\tilde{\mathbf{P}}$ is determined from the last column of \mathbf{V} as:

$$\tilde{\mathbf{P}} = \begin{bmatrix} v_{1,12} & v_{2,12} & v_{3,12} & v_{4,12} \\ v_{5,12} & v_{6,12} & v_{7,12} & v_{8,12} \\ v_{9,12} & v_{10,12} & v_{11,12} & v_{12,12} \end{bmatrix} \quad (\text{A.23})$$

Following the camera model as used in equation A.13, the minimization of $\sum_i d(\vec{x}_i, P\vec{X}_i)$ which is the projection error between the measured 2D points and the projection of their 3D correspondences, gives the optimization criteria. The Levenberg-Marquardt Algorithm may be used to retrieve a first approximation for the preceeding SVD.

Denormalization The camera matrix for the original coordinates is obtained from $\tilde{\mathbf{P}}$ by denormalization of $\tilde{\mathbf{P}}$ (see A.17) by

$$\mathbf{P} = \mathbf{T}^{-1} \tilde{\mathbf{P}} \mathbf{U} \quad (\text{A.24})$$

A.4. Schematics

The schematics for the automatic amplification alignment for the OPT101 is given in figure A.2. The OPT101 is connected to Connector 'Conn1', while its wiring follows the reference of the producer.

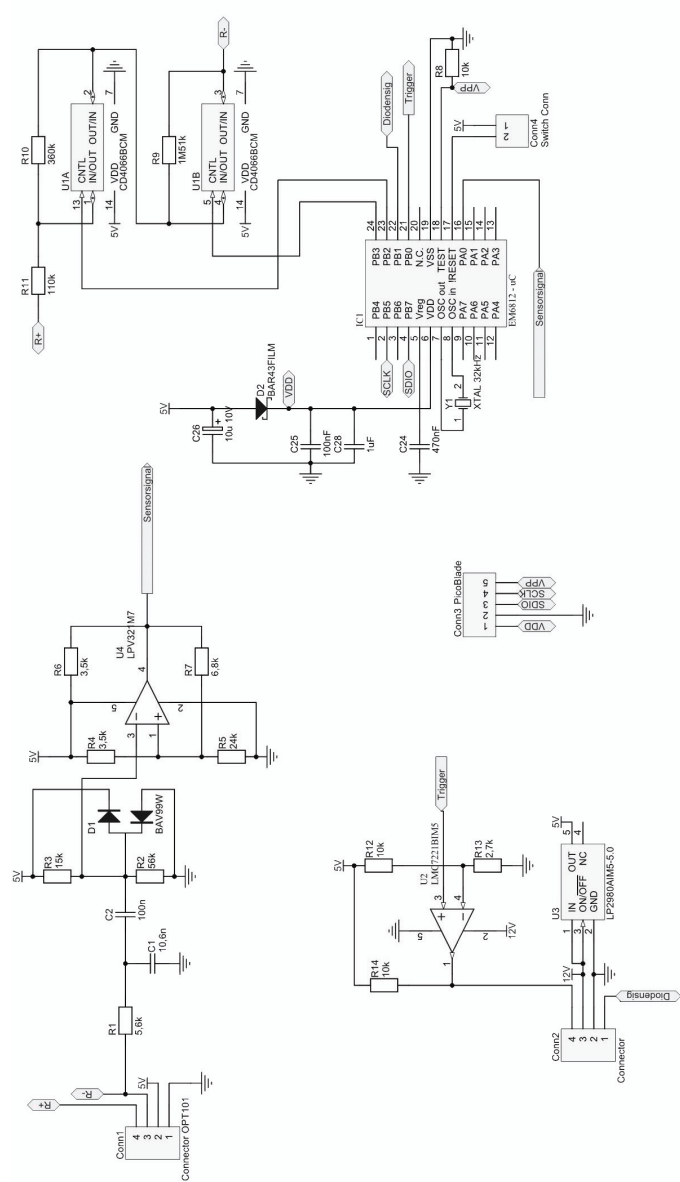


Figure A.2.: Schematics for the optical trigger extraction

A.5. Results of different image processing algorithms

The visibility of the result in section 4.1.2 is not optimal for precise inspection. Due to space limitation for a good readable text the single images are repeated here upscaled on the following pages.

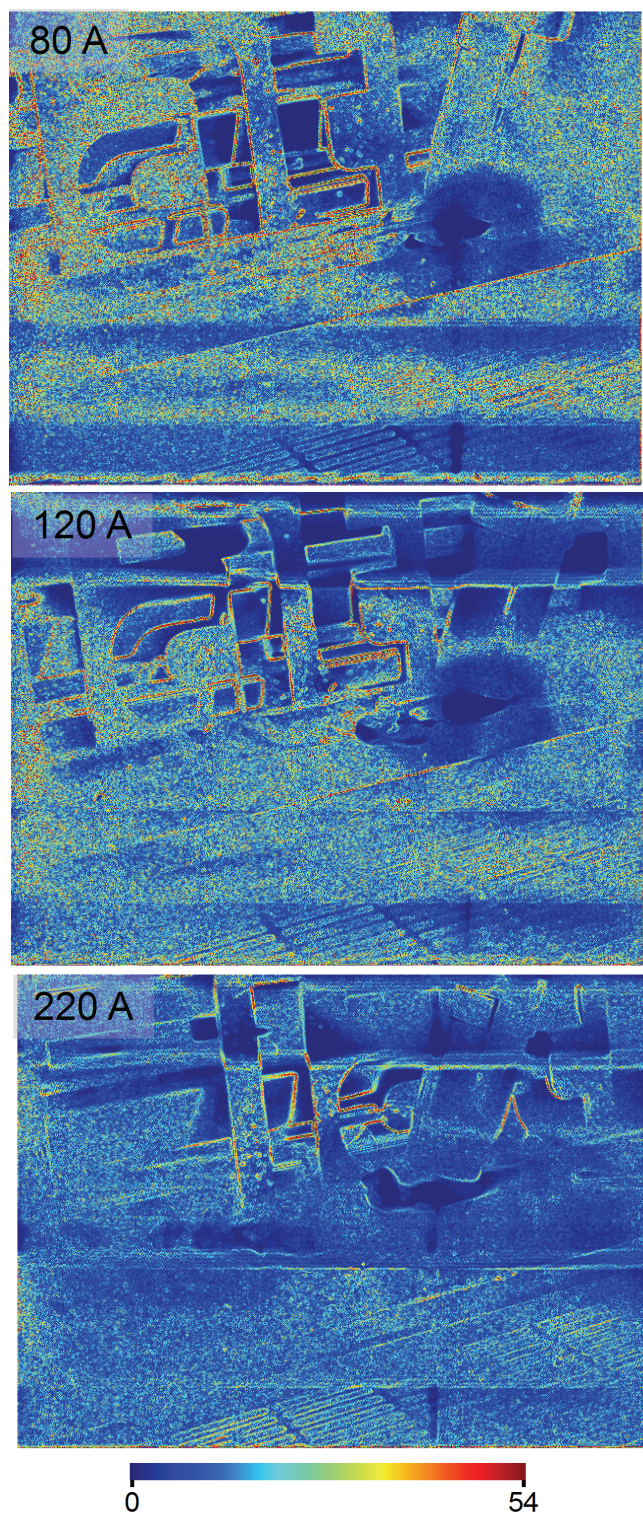


Figure A.3.: *MAG: Gradient difference of Histogram equalization and original image for 80 A, 120 A and 220A*

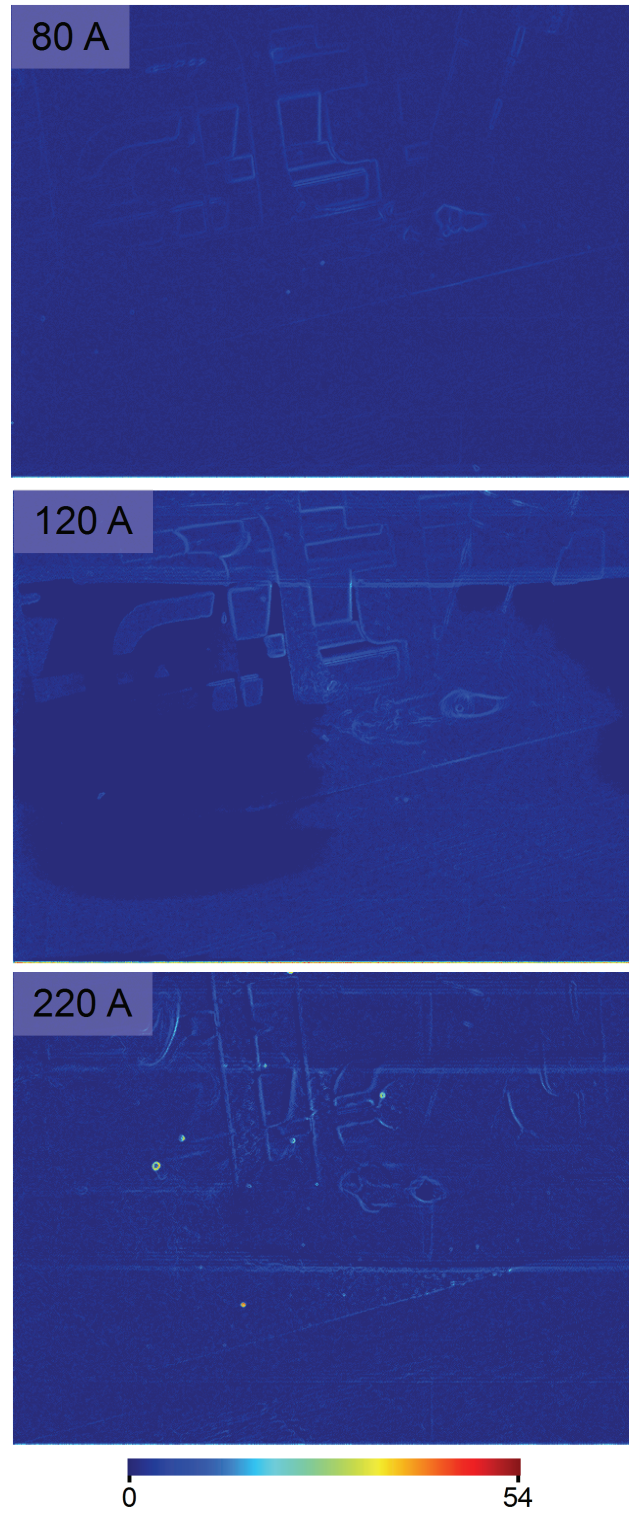


Figure A.4.: *MAG: Gradient difference of GLG and original image for 80 A, 120 A and 220A*

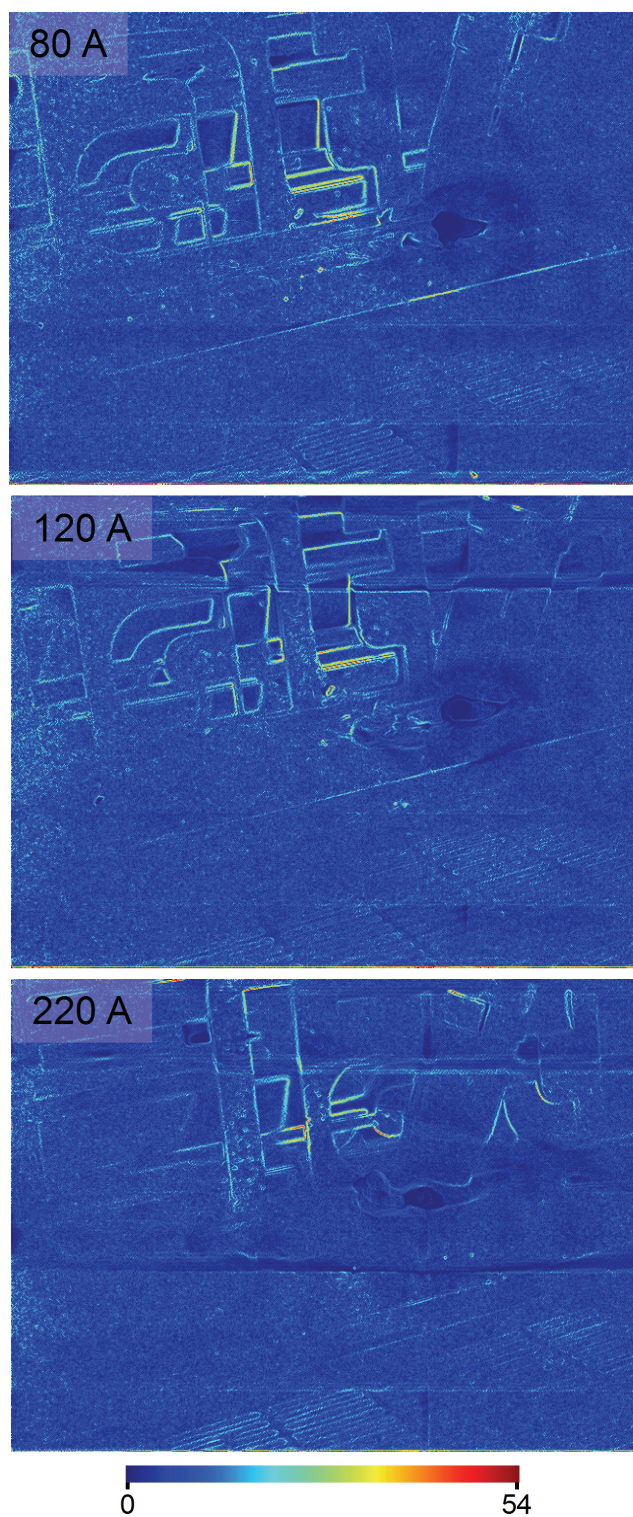


Figure A.5.: *MAG: Gradient difference of CLAHE and original image for 80 A, 120 A and 220A*

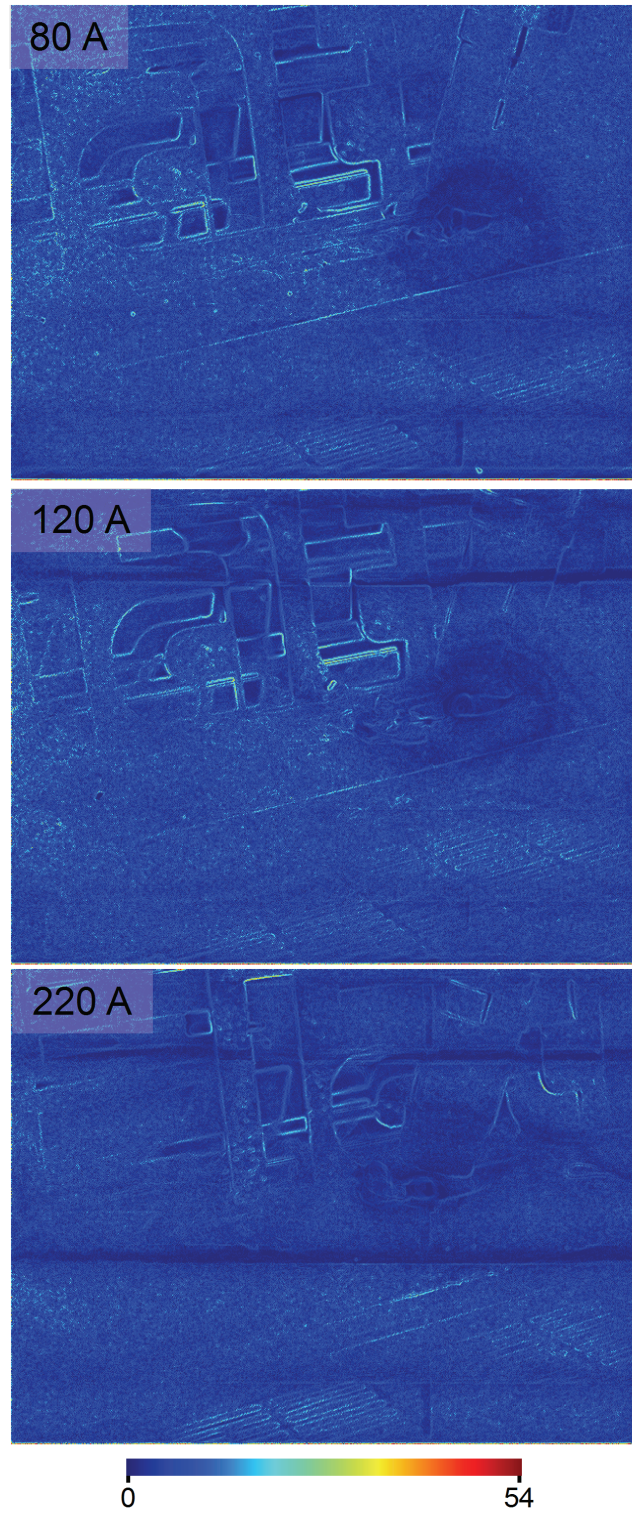


Figure A.6.: *MAG: Gradient difference of VBSAHE and original image for 80 A, 120 A and 220A*

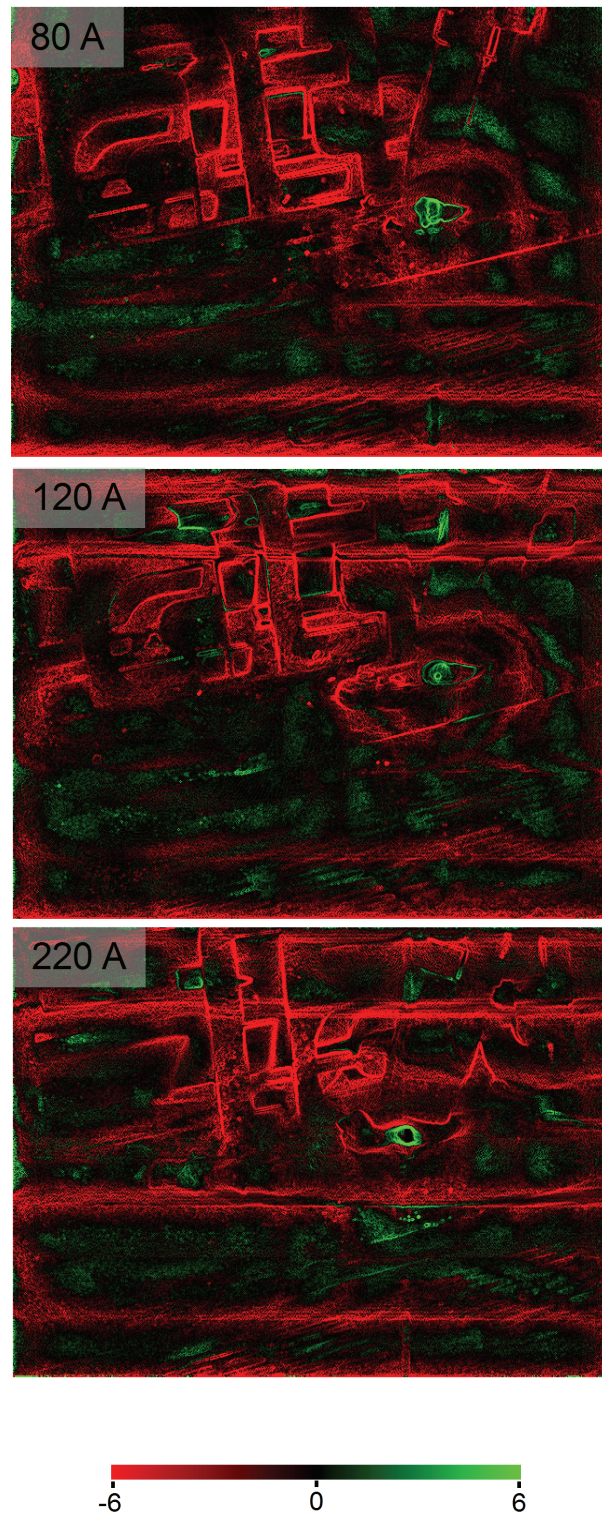


Figure A.7.: *MAG: Gradient difference of VBSAHE and CLAHE results for 80 A, 120 A and 220A*

Bibliography

- [1] P. Milgram, H. Takemura, A. Utsumi, and F. Kishino, “Augmented Reality: A class of displays on the reality-virtuality continuum,” in *SPIE Proceedings of Telem manipulator and Telepresence Technologies*, no. 2351, 1994, pp. 282–292.
- [2] R. L. O’Brien, *Welding processes*, 8th ed., ser. Welding handbook. Miami, Fla, USA: American Welding Society, 1995, vol. Vol. 2.
- [3] K.-J. Matthes and E. Richter, *Schweißtechnik - Schweißen von metallischen Konstruktionswerkstoffen*, 4th ed. München: Fachbuchverlag Leipzig, 2008.
- [4] K. Weman, *Welding processes handbook*, vii ed. Boca Raton, Fla., USA: CRC Press Inc, 2003.
- [5] D. Saini and S. Floy, “An investigation of gas metal arc welding sound signature for on-line quality control,” *Welding Journal*, vol. 4, pp. 172–179, 1998.
- [6] S. Steeb, *Zerstörungsfreie Werkstück- und Werkstoffprüfung - Die gebräuchlichsten Verfahren im Überblick*, 3rd ed., ser. Kontakt und Studium. Renningen: expert Verlag, 2005, vol. 243.
- [7] E. Sutter, A. Schirmacher, I. Decker, and G. Ott, *Elektrooptische Schweisserschutzfilter und Abschirmungen an Schweißerarbeitsplätzen - Sicherheitsanalyse und Messverfahren*, ser. Schriftenreihe der Bundesanstalt für Arbeitsschutz und Arbeitsmedizin. Bremerhaven: Wirtschaftsverlag NW, 1997, vol. 756.
- [8] W. Koschinski, A. Schirmacher, E. Sutter, G. Ott, and M. Janssen, *Automatische Schutzstufeneinstellung elektrooptischer Schweißerschutzfilter*, ser. Schriftenreihe der Bundesanstalt für Arbeitsschutz und Arbeitsmedizin,. Bremerhaven: Wirtschaftsverl. NW, Verl. für neue Wiss, 1999, vol. 859.
- [9] B. Hillers, D. Aiteanu, and A. Graeser, “Augmented-Reality Helmet for the manual welding process,” in *Virtual and Augmented Reality applications in manufacturing*, S. K. Ong and A. Y. C. Nee, Eds. London: Springer, 2004, pp. 361–381.
- [10] D. Aiteanu, B. Hillers, and A. Graeser, “A Step Forward in Manual Welding: Demonstration of Augmented Reality Helmet,” in *The Second IEEE and ACM International Symposium on Mixed and Augmented Reality (ISMAR)*, Tokyo, Japan, Oct., 7.-10. 2003.

- [11] —, “Improvement of the welding seam quality and minimizing the production costs in assembly process by using an Augmented-Reality helmet,” in *The second International Conference on Economical Engineering and Manufacturing Systems (ICEEMS)*, Brasov, Romania, Oct., 23.-25. 2003.
- [12] P. Tschirner, B. Hillers, and A. Graeser, “A concept for the application of augmented reality in manual gas metal arc welding,” in *International Symposium on Mixed and Augmented Reality (ISMAR)*, Darmstadt, Germany, 2002.
- [13] B. Hillers and A. Graeser, “Augmented Reality- The Third Way for New Technologies in Welding Education,” in *Technical Conference: Welding Trainer 2010 - The Future of Education*. Duisburg: GSI SLV Ruhr, September, 08.-09. 2010.
- [14] R. C. Gonzalez and R. E. Woods, *Digital image processing*, 3rd ed. Reading, Massachusetts: Addison-Wesley Publishing Company, 2007.
- [15] E. Reinhard, G. Ward, S. Pattanaik, and P. Debevec, *High Dynamic Range Imaging - Acquisition, Display and Image-based Lighting*, 1st ed. Elsevier, 2006.
- [16] R. F. Schmidt, G. Thews, and F. Lang, *Physiologie des Menschen*, 28th ed., ser. Springer-Lehrbuch. Berlin: Springer, 2000.
- [17] Wikipedia, *The Free Encyclopedia* - <http://www.wikipedia.org/>, 2007.
- [18] J. K. Ijspeert, T. J. P. Vandenberg, and H. Spekreijse, “A mathematical description of the foveal visual point spread function with parameters for age, pupil size and pigmentation,” *Vision Research*, vol. 33, no. 1, pp. 15–20, 15-20.1.1993 1993.
- [19] D. Sliney and M. Wolbarsht, *Safety with lasers and other optical sources - a comprehensive handbook*, 4th ed. New York [u.a.]: Plenum Press, 1985.
- [20] K. Hug, M. Rösli, and R. Rapp, “Magnetic field exposure and neurodegenerative diseases in recent epidemiological studies,” *Social and Preventive Medicine*, vol. V51, no. 4, pp. 210 – 220, 2006/07/19/ 2006.
- [21] V. G. Chigrinov, *Liquid crystal devices - physics and applications*, ser. Artech House optoelectronics library. Boston: Artech House, 1999.
- [22] T. Scharf, *Polarized light in liquid crystals and polymers*. Hoboken, N.J, USA: Wiley, 2007.
- [23] S.-B. Chen and J. Wu, *Intelligentized Methodology for Arc Welding Dynamical Process - Visual Information Acquiring, Knowledge Modeling and Intelligent Control of Arc Welding Dynamical Process*, 1st ed., ser. Lecture Notes in Electrical Engineering Vol.29. Heidelberg: Springer, 2009.

- [24] H. C. Wikle, S. Kottilingam, R. H. Zee, and B. A. Chin, "Infrared sensing techniques for penetration depth control of the submergege arc welding process," *Journal of Materials Processing Technology*, vol. 113, pp. 228–233, 2001.
- [25] T. U. Berlin, "Verfahren und Vorrichtung zum Regeln eines Energieertrags bei einem Fügeprozeß - Patent: DE102004015553A1," Patent, March, 30., 2004.
- [26] G. Saeed, Y. M. Zhang, and S. Cook, "A compact vision sensor for weld pool surface sensing," *International Journal of Modelling, Identification and Control*, vol. 1, no. 2, pp. 94–100, 2006.
- [27] Z. Yan, D. Xu, Y. Li, and M. Tan, "A Vision-Based Seam Tracking System for Submerged Arc Welding," in *Lecture Notes in Control and Information Sciences*, Springer, Ed., 2007, vol. 362, pp. 349–357.
- [28] P. Xu, G. Xu, X. Tang, and S. Yao, "A visual seam tracking system for robotic arc welding," *International journal of advanced manufacturing technology*, vol. 37, no. 1-2, pp. 70–75, 2008.
- [29] D. Xu, L. Wang, and M. Tan, "Image Processing and Visual Control Method for Arc Welding Robot," in *IEEE International Conference on Robotics and Biomimetics (RO-BIO)*, Shenyang, China, Aug. 2004, pp. 727–732.
- [30] Y. M. Zhang, R. Kovacevic, and L. Li, "Characterization and real-time measurement of geometrical appearance of the weld pool," *International Journal of Machine Tools and Manufacture*, vol. 36, no. 7, pp. 799 – 816, 1996.
- [31] H. Fennander, V. Kyrki, A. Fellman, A. Salminen, and H. Kälviäinen, "Visual measurement and tracking in laser hybrid welding," *Machine Vision and Applications*, vol. 20, no. 2, p. 103, 2009.
- [32] S. Nordbruch, "Procedure for the optimization of PGMAW using visual and electrical information," Ph.D. dissertation, Universität Bremen, Germany, 2005.
- [33] D. Schreiber, L. Cambrini, J. Biber, and B. Sardy, "Online visual quality inspection for weld seams," *The International Journal of Advanced Manufacturing Technology*, vol. 42, no. 5, p. 497, 2009.
- [34] B. Brzakovic and D. T. Khani, "Weld Pool Edge Detection for Automated Control of Welding," *IEEE Transactions on Robotics and Automation*, vol. 7, no. 3, pp. 397–403, 1991.
- [35] K. Y. Bae, T. H. Lee, and K. C. Ahn, "An optical sensing system for seam tracking and weld pool control in gas metal arc welding of steel pipe," *Journal of Materials Processing Technology*, vol. 120, no. 1-3, pp. 458 – 465, 2002.

- [36] J. S. Smith and C. Balfour, "Real-time top-face vision based control of weld pool size," *Industrial Robot: An International Journal*, vol. 32, no. 4, pp. 334–340, 2005.
- [37] F. Chongjian, S. B. Chen, and T. Lin, "Visual Sensing and Image Processing in Aluminum Alloy Welding," *Robotic Welding, Intelligence and Automation*, vol. 262, p. 275, 2007.
- [38] B. Hoefflinger and V. Schneider, "The High-Dynamic-Range Sensor," in *High-Dynamic-Range (HDR) Vision Microelectronics, Image Processing, Computer Graphics*, 1st ed., B. Hoefflinger, Ed. Springer, 2007, vol. 26, pp. 13–56.
- [39] U. Seger, H.-G. Graf, and M. E. Landgraf, "Vision assistance in scenes with extreme contrast," *IEEE Micro*, vol. 13, no. 1, pp. 50–56, Feb 1993.
- [40] H.-J. Schoenherr, "Lenses for HDR Imaging," in *High dynamic range (HDR) vision*, B. Höfflinger, Ed. Springer, 2007, vol. 26, pp. 99–105.
- [41] A. K. Jain, *Fundamentals of digital image processing*. Prentice-Hall, Inc. Upper Saddle River, NJ, USA, 1989.
- [42] J. C. Russ, *The image processing handbook*. Boca Raton, FL: CRC Press, 2002.
- [43] B. Jaehne, *Digital Image Processing*, 6th ed. Berlin, Heidelberg: Springer-Verlag, 2005.
- [44] Z. Y. Chen, B. Abidi R., P. D. L., and M. A. Abidi, "Gray-level grouping (GLG): an automatic method for optimized image contrast Enhancement-part I: the basic method," *IEEE Transactions on Image Processing*, vol. 15, no. 8, pp. 2290–2302, Aug. 2006.
- [45] J. DiCarlo and B. Wandell, "Rendering high dynamic range images," in *Proceedings of the SPIE: Image Sensors*, vol. 3965. SPIE, 2000, pp. 392–401.
- [46] J. Y. Kim, L. S. Kim, and S. H. Hwang, "An advanced contrast enhancement using partially overlapped sub-block histogram equalization," *IEEE Transactions on Circuits and Systems for Video Technology*, vol. 11, no. 4, pp. 475–484, 2001.
- [47] S. M. Pizer, E. P. Amburn, J. D. Austin, R. Cromartie, A. Geselowitz, T. Greer, B. T. H. Romeny, and J. B. Zimmerman, "Adaptive histogram equalization and its variations," *Computer Vision, Graphics and Image Processing*, vol. 39, no. 3, pp. 355–368, 1987.
- [48] K. Zuiderveld, "Contrast Limited Adaptive Histogram Equalization," in *Graphics Gems IV*. Boston: Academic Press, 1994, pp. 474–485.
- [49] A. M. Reza, "Realization of the Contrast Limited Adaptive Histogram Equalization (CLAHE) for Real-Time Image Enhancement," *The Journal of VLSI Signal Processing*, vol. 38, no. 1, pp. 35 – 44, 2004/08/01/ 2004.

-
- [50] N. Wiener, *Extrapolation, Interpolation and Smoothing of Stationary Times Series: With Engineering Applications*, 5th ed. Cambridge: MIT Press, 1964, vol. 9.
- [51] C. Tomasi and R. Manduchi, "Bilateral filtering for gray and color images," in *Proceedings of the Sixth International Conference on Computer Vision*, vol. 846. Citeseer, 1998.
- [52] F. Durand and J. Dorsey, "Fast bilateral filtering for the display of high-dynamic-range images," in *Proceedings of the 29th annual conference on Computer graphics and interactive techniques*. ACM New York, NY, USA, 2002, pp. 257–266.
- [53] D. Comaniciu and P. Meer, "Mean Shift: A Robust Approach Towards Feature Space Analysis - dobe," *IEEE Transaction on Pattern Analysis and Machine Intelligence*, vol. 24, no. 5, pp. 603–619, May 2002.
- [54] P. E. Debevec and J. Malik, "Recovering high dynamic range radiance maps from photographs," in *SIGGRAPH '97: Proceedings of the 24th annual conference on Computer graphics and interactive techniques*. New York, NY, USA: ACM Press/Addison-Wesley Publishing Co., 1997, pp. 369–378.
- [55] S. B. Kang, M. Uyttendaele, S. Winder, and R. Szeliski, "High dynamic range video," in *ACM SIGGRAPH 2003*. New York, NY, USA: ACM Press, 2003, pp. 319–325.
- [56] G. Ward, "Fast, Rrobust Image registration for compositing high dynamice range photographs from handheld exposures," *Journal of Graphics Tools*, vol. 8, no. 2, pp. 17–30, 2003.
- [57] K. Devlin, *A Review of Tone Reproduction Techniques*, ser. Technical report: CSTR-02-005. Department of Computer Science; University of Bristol, 2002.
- [58] F. Drago, K. Myszkowski, T. Annen, and N. Chiba, "Adaptive logarithmic mapping for displaying high contrast scenes," *Computer Graphics Forum*, vol. 22, no. 3, pp. 419 – 426, 2003.
- [59] E. Reinhard and K. Devlin, "Dynamic Range Reduction Inspired by Photoreceptor Physiology," *IEEE Transactions on Visualization and Computer Graphics*, vol. 11, no. 1, pp. 13–24, 2005.
- [60] B. Hoefflinger, *High-Dynamic-Range (HDR) Vision - Microelectronics, Image Processing, Computer Graphics*, 1st ed., ser. Springer Series in Advanced Microelectronics. Springer, 2007.
- [61] B. Hillers and A. Graeser, "Direct welding arc observation without harsh flicker," in *AWS welding show*, Chicago, Nov., 11.-14. 2007.
- [62] —, "Real time Arc Welding Video Observation System," in *62nd International Conference of the IIW*, Singapore, July, 12.-17. 2009, pp. 65–69.
-

- [63] S. Zeki, *A vision of the brain*, 6th ed. Oxford: Blackwell Scientific Publications, 1993.
- [64] J. S. Lee, "Digital image enhancement and noise filtering by use of local statistics," *IEEE Transactions on Pattern Analysis and Machine Intelligence*, no. 2, pp. 165–168, 1980.
- [65] J. S. Lim, *Two-dimensional signal and image processing*. Englewood Cliffs. NJ: Prentice Hall, 1990.
- [66] B. Hillers, V. Gui, and A. Gräser, "Contrast Enhancement in Video Sequences Using Variable Block Shape Adaptive Histogram Equalization," in *31st IAT Colloquium of Automation*. Leer: Institute of Automation, November, 05.-06. 2009.
- [67] A. Koschan and M. A. Abidi, *Digital color image processing*. Hoboken, NJ: Wiley-Interscience, 2008.
- [68] K. Fukunaga and L. D. Hostetler, "The Estimation of the Gradient of a Density Function, with Application in Pattern Recognition," *IEEE Transactions on Information Theory*, vol. 21, pp. 32–40, 1975.
- [69] H. Kato and M. Billinghurst, "Marker Tracking and HMD Calibration for a video-based Augmented Reality Conferencing System," in *Proceedings of the 2nd International Workshop on Augmented Reality (IWAR 99)*, San Francisco, USA, 1999.
- [70] D. Schmalstieg, H. Fuhrmann A. G., Z. Szalavari, M. Encarnacao L. M. Gervautz, and W. Purgathofer, "The Studierstube Augmented Reality Project," *Presence: Teleoperators and Virtual Environments*, vol. 11, no. 1, pp. 32–54, 2002.
- [71] R. Hartley and A. Zisserman, *Multiple View Geometry in Computer Vision*, 1st ed. Cambridge, UK: Cambridge University Press, 2000.
- [72] M. Tuceryan, Y. Genc, and N. Navab, "Single-Point active alignment method (SPAAM) for optical see-through HMD calibration for augmented reality," *Presence: Teleoperators and Virtual Environments*, vol. 11, no. 3, pp. 259–276, 2002.
- [73] W. H. Press, S. A. Teukolsky, and W. T. Vetterling, *Numerical recipes in C - the art of scientific computing*. Cambridge University Press, 1992.
- [74] M. D. Fairchild, *Color appearance models*, 2nd ed. Hoboken, NJ: Wiley, 2006.
- [75] K. Levenberg, "A Method for the Solution of Certain Problems in Least Squares," *Quart. Appl. Math*, vol. 2, pp. 164–168, 1944.
- [76] D. Marquardt, "An Algorithm for Least-Squares Estimation of Nonlinear Parameters," *Journal of the Society for Industrial and Applied Mathematics*, vol. 11, no. 2, pp. 431–441, 1963.

List of Figures

1.1. Technical Concept of GMAW. (source:[3])	22
1.2. Phases of the short circuit welding arc (source:[2])	23
1.3. Qualitative example of measured spray transfer	24
1.4. Technical principle of a TIG process (source:[3])	25
1.5. CCD camera image of MAG process with bloomed view on arc	27
1.6. Example of spectral irradiance for MAG welding of mild steel with a mixture of argon and carbon dioxide (18%) at 100 A	30
1.7. Mixed Reality continuum	32
1.8. Conceptional Setup of the TEREDES welding helmet	33
2.1. Human eye cross-sectional view, [Courtesy: NIH National Eye Institute] . . .	36
2.2. Scotopic and Photopic Vision [source:[17]]	37
2.3. Modulation Transfer Function	38
2.4. Schematic of absorption of UV-radiation in the ocular media of the human eye	39
2.5. Transmission requirements for shading level	41
2.6. Principles of LCD using TN technique	41
2.7. Depth up to which 90% of Photons are absorbed depending on wavelength . .	45
2.8. Inner Photo Effect for a Pixel on a CCD-sensor [courtesy: Olympus AG] . . .	45
2.9. Circuit for one HDRC Pixel	47
2.10. Image of the automatic test stand without FPN correction	48
2.11. Image of the automatic test stand with FPN correction	48
2.12. Spectral response of Gevilux lenses [40]	49
2.13. Spectral response of standard tube lense system	50
2.14. Subjects of the thesis beyond the State-of-the-Art (with green background) .	55
3.1. Top-down approach for a SADF setup	57
3.2. Signal diagram for a single pixel of the used Falldorf FuGa1000 camera	59
3.3. Impulse Arc: 23 V, 122 A, Gas with 82% Argon and 18% CO_2 , mild steel . .	60
3.4. Short-arc: 22 V, 150 A, Gas with 82% Argon and, 18% CO_2 , mild steel . . .	61
3.5. Phases during an arc segment (pulsed)	62
3.6. White stripe in camera image caused by brightness change	63
3.7. Sequence with hopping white stripe	63
3.8. Simple optical trigger on the welding process	63
3.9. a.) noisy signal from optical sensor, b.) bandpass filtered signal	64
3.10. Schmitt-Trigger signal of optical sensor signal	64
3.11. Sensor amplification control	65
3.12. Change of contrast dynamic by additional reflected light	66

3.13. CREE XR-E 7090 Q5 LED, Cooler and Optics	66
3.14. Lighting unit with two CREE Q5 LEDs	67
3.15. Mounting four CREE Q5 LEDs with active cooled housing on a welding helmet	67
3.16. Rise-time of the CREE Q5 setup	68
3.17. Setup for measuring the delay between the triggersignal and the first line read-out	68
3.18. Qualitative waveform of arc light intensity at pulsed MAG process with 120A, mild steel and a massive electrode with 1.2mm diameter	69
3.19. Histogram clipping by saturation of A/D converter	70
3.20. Histogram clipping for dark pixels	70
3.21. Image merging of two images I_1 and I_2 mapping two different ranges of values	71
3.22. Underexposed image	71
3.23. Overexposed image	72
3.24. Composition from high (red), mid (green) and low (blue) radiance information from images in figure 3.22 and figure 3.23	72
3.25. Resulting image by merging images in figure 3.22 and figure 3.23	73
3.26. Pseudocolour image with 351 grey levels corressponding to figure 3.25	74
3.27. Original camera image from welding scene with torch, arc and seam	74
3.28. Histogram of the Original image as given in figure 3.27	74
3.29. (top) Resulting grey level images of Histogram Equalization for 8, 16, 32 and 256 different resulting bins. (bottom) Corresponding histograms	75
3.30. Histogram example for the grouping and ungrouping process	77
3.31. Histogram after first grouping and ungrouping process	79
3.32. Mapping for a different amount of selected groups	80
3.33. Contrast measure for different amount of groups	80
3.34. Camera image processed using AHE approach	81
3.35. Bilinear merging of contextual regions A , B , C , D	82
3.36. Camera image with an 8x8 grid of tiles (red lines)	82
3.37. Camera image processed by the CLAHE algorithm	82
3.38. Noise supression in the image processing queue using a Wiener Filter	83
3.39. a.) CLAHE without pre-filter, b.) CLAHE with Wiener filter	84
3.40. Original camera image from welding scene with torch, arc and seam	85
3.41. Improvement by Wiener filtering and processing with CLAHE algorithm . . .	85
3.42. a.) Filter sequence Wiener \rightarrow CLAHE \rightarrow unsharp filter b.) Filter sequence Wiener \rightarrow CLAHE \rightarrow Wiener filter	85
3.43. Basic Variable Block Shape Adaptive Histogram Equalization setup	86
3.44. Epanechnikov kernel	89
3.45. Normal Gaussian kernel	89
3.46. Original camera image identical to figure 3.27	91
3.47. Mean shift applied to figure 3.46	91
3.48. Floodfill clustering of figure 3.47 with colour distance $c_d = 20$	91
3.49. Interpolating the pixel value by histogram mapping functions of the proximity	93
3.50. VBSAHE applied to the original image in figure 3.27	94
3.51. Mean value by row and column as the distance from left or from the top of the image	95
3.52. Minimizing the white stripe using top-hat operator with different structuring elements	96

3.53. Prototype setup for the SADF system	96
3.54. Black matrix on the GLCD to minimize the scattering light	98
3.55. Camera and LCD Plane for SADF	99
3.56. Coordinate Systems for SADF setup	99
4.1. Test-stand for semi-automated welding	104
4.2. MAG, 85 A, LED Off	106
4.3. MAG, 85 A, LED On	106
4.4. MAG, 120 A, LED Off	106
4.5. MAG, 120 A, LED On	106
4.6. MAG, 220 A, LED Off	107
4.7. MAG, 120 A, LED On	107
4.8. MAG, 85A, underexposed	107
4.9. MAG, 85 A, overexposed	107
4.10. MAG, 120 A, underexposed	108
4.11. MAG, 120 A, overexposed	108
4.12. MAG, 220 A, underexposed	108
4.13. MAG, 220 A, overexposed	108
4.14. MAG, 85 A, LED On, Segmentation by Mean Shift approach	109
4.15. MAG 85 A: Enhanced with a.) Histogram Equalization, b.) Grey-Level- Grouping, c.) CLAHE, d.) VBSAHE	110
4.16. MAG 120 A: Enhanced with a.) Histogram Equalization, b.) Grey-Level- Grouping, c.) CLAHE, d.) VBSAHE	111
4.17. MAG 220 A: Enhanced with a.) Histogram Equalization, b.) Grey-Level- Grouping, c.) CLAHE, d.) VBSAHE	111
4.18. MAG: Gradient difference of histogram equalized images and original image for 85 A, 120 A and 220 A	112
4.19. MAG: Gradient difference of GLG processed image and original image corres- ponding to 85 A, 120 A and 220 A	113
4.20. MAG: Gradient difference of CLAHE processed image and original image corresponding to 85 A, 120 A and 220 A	113
4.21. MAG: Gradient difference of VBSAHE processed image and original image corresponding to 85 A, 120 A and 220A	114
4.22. MAG: Gradient difference of VBSAHE and CLAHE results corresponding to 85 A, 120 A and 220A	114
4.23. MAG, 85 A, VBSAHE Applied with LED Off (Left), LED On (Right)	115
4.24. MAG, 120 A, VBSAHE Applied with LEDs Off (left) and LEDs On (right) .	116
4.25. MAG, 220 A, VBSAHE Applied with LEDs Off (left) and LEDs On (right) .	116
4.26. MAG process at 85 A: Merge composition of the resulting image from the underexposed (red), both (green) and overexposed (blue) image	117
4.27. MAG, 85 A: False Colour of the merged images with 389 greyscale values . .	118
4.28. MAG, 85 A: Result of the merging process	118
4.29. Segmentation of the merged image result	119
4.30. MAG, 85 A: Result of the VBSAHE processing	119
4.31. MAG process at 120 A: Merge composition of the resulting image from the underexposed (red), both (green) and overexposed (blue) image	119
4.32. MAG, 120 A: False Colour of the merged image with 337 greyscale values . .	120

4.33. MAG, 120 A: Result of the merging process	120
4.34. MAG, 120 A: Result of the VBSAHE algorithm	120
4.35. MAG process at 220 A: Merge composition of the resulting image from the underexposed (red), both (green) and overexposed (blue) image	121
4.36. MAG, 220 A: False Colour of the merged image with 321 greyscale values . .	122
4.37. MAG, 220 A: Result of the merging process	122
4.38. MAG, 220 A: Result of applying the VBSAHE algorithm	122
4.39. Original camera image for MIG welding process	123
4.40. MIG: Result of the CLAHE for 80 A, 180 A and 240 A welding current . . .	124
4.41. MIG: Result of the VBSAHE with 80 A, 180 A, 240 A welding current	124
4.42. TIG DC pulsed 230 A: a.) Original b.) Segmentation by Mean Shift approach	125
4.43. Result of contrast enhancement: a.) VBSAHE b.) CLAHE	125
4.44. Difference of image gradient for VBSAHE and CLAHE results	126
4.45. Mannequin with camera in the right eye	127
4.46. SADP testing by mannequin view	127
A.1. Pinhole camera geometry with C the camera centre and p the principal point	133
A.2. Schematics for the optical trigger extraction	136
A.3. MAG: Gradient difference of Histogram equalization and original image for 80 A, 120 A and 220A	138
A.4. MAG: Gradient difference of GLG and original image for 80 A, 120 A and 220A	139
A.5. MAG: Gradient difference of CLAHE and original image for 80 A, 120 A and 220A	140
A.6. MAG: Gradient difference of VBSAHE and original image for 80 A, 120 A and 220A	141
A.7. MAG: Gradient difference of VBSAHE and CLAHE results for 80 A, 120 A and 220A	142

List of Tables

2.1. Overview about European Norms [EN] for personal eye protection	40
2.2. Contrast sensitivity of the last significant bit in percentage for logarithmic mapping [38]	47
3.1. Factors forming the arc emitted light	62
3.2. Groups and borders of the example given in figure 3.30	77
3.3. GLCD Specification	97
4.1. Series of measurements to evaluate different image enhancement algorithms .	105
4.2. Brightness of pulsed MAG process at 1 m distance from the welding torch . .	106
4.3. Mean values for the gradient differences	112
4.4. Brightness of pulsed MIG process at 1 m distance from the welding torch . .	123